中国科学技术大学

博士学位论文

锶原子的冷却和囚禁

用于里德堡态的量子模拟

作者姓名： Ingo Nosske

学科专业： 原子与分子物理

导师姓名： Matthias Weidemüller 教授

完成时间： 二〇一八年五月三十日

University of Science and Technology of China

A dissertation for doctor's degree

Cooling and trapping of strontium atoms for quantum simulation using Rydberg states

Author: Ingo Nosske

Speciality: Atomic and Molecular Physics

Supervisor: Prof. Matthias Weidemüller

Finished time: May 30, 2018

中国科学技术大学学位论文原创性声明

本人声明所呈交的学位论文，是本人在导师指导下进行研究工作所取得的成果。除已特别加以标注和致谢的地方外，论文中不包含任何他人已经发表或撰写过的研究成果。与我一同工作的同志对本研究所做的贡献均已在论文中作了明确的说明。

作者签名：_____　　签字日期：_____

中国科学技术大学学位论文授权使用声明

作为申请学位的条件之一，学位论文著作权拥有者授权中国科学技术大学拥有学位论文的部分使用权，即：学校有权按有关规定向国家有关部门或机构送交论文的复印件和电子版，允许论文被查阅和借阅，可以将学位论文编入《中国学位论文全文数据库》等有关数据库进行检索，可以采用影印、缩印或扫描等复制手段保存、汇编学位论文。本人提交的电子文档的内容和纸质论文的内容相一致。

保密的学位论文在解密后也遵守此规定。

□ 公开　□ 保密（____ 年）

作者签名：_____　　导师签名：_____

签字日期：_____　　签字日期：_____

摘　要

本论文介绍了一种实验装置，用来制备超冷锶原子和基于窄线宽互组谱线进行里德堡态激发。超冷锶原子，作为双电子原子系统，为里德堡物理研究提供了有趣的，尚未被探索过的机会。锶原子存在线宽很窄的互组谱线，其第二个价电子可以用来囚禁和成像，这些是常用碱金属原子所不具备的。

我们从零开始设计和搭建实验装置。整个装置包括超高真空系统，磁场和用于锶原子冷却、再泵浦、里德堡激发的激光系统。我们重点介绍一种新型横向装载的二维磁光阱，用于产生冷锶原子束。在 500 °C 适中的原子炉温度下，对于同位素 ^{88}Sr，冷锶原子束装载到邻近三维磁光阱的速率高达 10^9 s^{-1}。所有四种稳定同位素都可以被囚禁，包括波色子和费米子。与塞曼减速器相比，冷原子束可以避免黑体辐射和真空污染的带来的影响。

我们展示了一束 481 纳米的再抽运光用于抽运 $5s5p\,^3P_2 \rightarrow 5p^2\,^3P_2$ 跃迁，可以提高磁光阱中原子数目一个数量级。我们也介绍了后续的激光冷却过程，包括磁阱和基于窄线宽互组谱线的锶原子磁光阱。该锶原子磁光阱可以实现温度低至 μK。

我们也实现了在窄线宽锶原子磁光阱中进行里德堡三重态的激发。通过原子损失光谱，我们获得了线宽低至 MHz 的里德堡共振谱线。论文中介绍的技术和结果为进一步实现基于超冷双电子原子里德堡态的量子模拟打下了很好的基础。

关键词：超冷锶原子，二维磁光阱，窄互组谱线，双电子里德堡原子

ABSTRACT

This thesis describes an experimental apparatus which produces ultracold strontium atoms and allows for their excitation to triplet Rydberg states via a narrow intercombination line. Ultracold strontium atoms, as two-electron systems, offer intriguing research opportunities in the field of Rydberg physics, brought about by the presence of metastable states and by the second valence electron which allows one to employ trapping and imaging techniques not possible in the commonly used alkali atoms.

Starting with an empty lab, a new experimental apparatus has been designed and realized. It comprises an ultra-high vacuum system, magnetic field sources and laser systems which are required for cooling, repumping and Rydberg excitation of strontium atoms. A novel feature is the implementation of a transversely loaded two-dimensional magneto-optical trap, which serves as a source of a cold strontium atomic beam. Loading rates of the atomic beam into a nearby three-dimensional magneto-optical trap (MOT) exceeding 10^9 s^{-1} for the ^{88}Sr isotope at a moderate strontium oven temperature of $500\,^{\circ}\mathrm{C}$ are reported. All the four stable isotopes of strontium can be trapped, both bosons and fermions. This cold atom source minimizes black-body radiation and vacuum contamination at the position of the final experiments, as if compared to the Zeeman slower design.

A repumping laser addressing the $5\mathrm{s}5\mathrm{p}\,^3\mathrm{P}_2 \rightarrow 5\mathrm{p}^2\,^3\mathrm{P}_2$ transition at 481 nm is shown to increase the atom number in the MOT by one order of magnitude. Subsequent steps in our laser cooling procedure are described, in particular a magnetic trap acting on atoms in the $5\mathrm{s}5\mathrm{p}\,^3\mathrm{P}_2$ state and a strontium MOT operating on a narrow intercombination line, with achieved temperatures in the low μK regime. At the end of this thesis excitations of ultracold strontium atoms in the narrow-line MOT to triplet Rydberg states are realized. By atom loss spectroscopy, a Rydberg resonance with a ~ 1 MHz linewidth is achieved. The established techniques and results described in this thesis pave the way for the realization of quantum simulation applications in our constructed apparatus, making use of ultracold two-electron atoms in Rydberg states.

Key Words: ultracold strontium atoms; two-dimensional magneto-optical trap; narrow intercombination lines; two-electron Rydberg atoms

Contents

Chapter 1 Introduction 1

Chapter 2 Experimental setup 4

2.1 Strontium 4

2.1.1 Chemical and nuclear properties 5

2.1.2 Electronic level scheme 6

2.1.3 The two laser cooling transitions 8

2.1.4 Metastable states and repumping 10

2.1.5 Laser cooling strategy 11

2.2 Vacuum system 12

2.2.1 Overview 12

2.2.2 2D-MOT chamber 14

2.2.3 Science chamber 15

2.3 Magnetic fields 17

2.3.1 2D-MOT 17

2.3.2 3D-MOT 19

2.4 Laser system 21

Chapter 3 Two-dimensional magneto-optical trap 25

3.1 Cold atom sources 25

3.2 Setup and diagnostics 27

3.2.1 2D-MOT setup 27

3.2.2 Diagnostics 30

3.3 Characterization of the cold atomic beam 32

3.4 Prospects for future designs 35

Chapter 4 Three-dimensional magneto-optical traps 37

4.1 Setup and diagnostics 37

4.1.1 3D-MOT setup 37

4.1.2 Diagnostics 38

4.2 Loading of the broad-line MOT 40

4.2.1 Loading and loss mechanism 40

4.2.2 Dependences on 2D-MOT parameters 43

4.2.3 Effect of Zeeman slowing 47

4.3 Repumping from the $^3P_2$ state · · · · · 48
4.4 Magnetic trapping of $^3P_2$ atoms · · · · · 49
4.5 Narrow-line cooling and trapping · · · · · 52

Chapter 5 Ultracold strontium Rydberg atoms · · · · · 55
5.1 Properties · · · · · 55
5.1.1 General properties · · · · · 55
5.1.2 Rydberg interactions · · · · · 58
5.1.3 Strontium Rydberg atoms · · · · · 63
5.2 Experimental results · · · · · 66
5.2.1 Principle of Rydberg loss spectroscopy · · · · · 66
5.2.2 Rydberg excitation in the broad-line MOT · · · · · 67
5.2.3 Rydberg excitation in the narrow-line MOT · · · · · 69

Chapter 6 Conclusion and outlook · · · · · 72

Appendix A Supplementary material for Chapter 2 · · · · · 75
A.1 Properties of the two laser cooling transitions · · · · · 75
A.2 Heating of the Zeeman slower viewport · · · · · 77
A.3 Vacuum system installation · · · · · 80

Appendix B Supplementary material for Chapter 3 · · · · · 83
B.1 Atomic flux determination by the TOF method · · · · · 83
B.1.1 Density and flux · · · · · 83
B.1.2 Measuring the flux · · · · · 84
B.2 Model for the 2D-MOT loading rate · · · · · 87

Bibliography · · · · · 89

Acknowledgements · · · · · 107

Publications · · · · · 109

List of Figures

2.1 Chemical properties of strontium · · · · · 6

2.2 Level scheme with all addressed transitions in our experiment · · · · · 7

2.3 Level scheme with alternative repumping transitions from the metastable states · · · · · 11

2.4 Vacuum system · · · · · 13

2.5 Customized steel science chamber · · · · · 16

2.6 Magnetic field generation for the 2D-MOT · · · · · 18

2.7 Magnetic field generation for the 3D-MOTs · · · · · 20

2.8 Schematic of the laser system · · · · · 22

3.1 Schematic of the 2D-MOT · · · · · 28

3.2 Optical setup for the 2D-MOT cooling and the Zeeman slower beams · · · · · 29

3.3 Angular dependence of the atomic beam fluorescence · · · · · 31

3.4 Characterization of the cold atomic beam · · · · · 33

4.1 Setup of the blue and red 3D-MOTs · · · · · 38

4.2 Fluorescence pictures of the blue 2D- and 3D-MOTs · · · · · 40

4.3 Loading curves and isotope spectrum of the blue MOT · · · · · 41

4.4 Blue MOT loss rate versus the cooling beam intensity · · · · · 42

4.5 Blue MOT temperature · · · · · 44

4.6 Blue MOT loading rate as a function of 2D-MOT parameters · · · · · 45

4.7 Blue MOT loading rate enhancement due to an additional Zeeman slower beam · · · · · 48

4.8 Atom number enhancement in the blue MOT due to the repumping beam · · 49

4.9 Magnetic trap lifetime · · · · · 50

4.10 Magnetic trap loading · · · · · 52

4.11 Operation of the red MOT · · · · · 53

5.1 Dipolar interactions between two Rydberg atoms · · · · · 59

5.2 Illustration of Rydberg blockade in a two-atom system · · · · · 62

5.3 Level scheme of the singly-charged strontium ion Sr^+ · · · · · 65

5.4 Level scheme for Rydberg excitation · · · · · 67

5.5 Rydberg excitation in the blue MOT · · · · · 68

5.6 Rydberg excitation in the red MOT · · · · · 70

5.7 $5s45s\,^3S_1$ loss spectra in the red MOT for different excitation times · · · · · 71

A.1 Heating of the Zeeman slower viewport · · · · · 78

A.2 Pressure during the 2D-MOT chamber bakeout · · · · · 81

A.3 Pressure rise tests in the science chamber · · · · · 82

B.1 TOF setup geometry for the 2D-MOT atomic flux determination · · · · · 85

List of Tables

2.1 Quantum statistics, nuclear spins and natural abundances for all stable isotopes of strontium · · · · · 6

2.2 Properties of the two laser cooling transitions for ^{88}Sr · · · · · 9

2.3 Distances, radii and numerical apertures of the science chamber viewports. 17

3.1 Typical values of the photodiode setup for the flux determination of the 2D-MOT cold atomic beam · · · · · 32

4.1 Overview of achieved blue MOT loading rates at an oven temperature of $465\ ^{\circ}\mathrm{C}$ for all stable isotopes of strontium · · · · · 47

5.1 Overview about n^*-scalings of Rydberg atom properties · · · · · 57

A.1 Extended table of the properties of the two laser cooling transitions for ^{88}Sr · · · · · 76

Notation

c_0	Speed of light	$299\,792\,458\ \mathrm{m/s}$
μ_0	Magnetic constant	$4\pi \times 10^{-7}\ \mathrm{N/A^2}$
ϵ_0	Electric constant	$8.854 \times 10^{-12}\ \mathrm{F/m}$
h	Planck constant	$6.626 \times 10^{-34}\ \mathrm{J\ s}$
$\hbar$	Reduced Planck constant	$1.055 \times 10^{-34}\ \mathrm{J\ s}$
e	Elementary charge	$1.602 \times 10^{-19}\ \mathrm{C}$
μ_B	Bohr magneton	$9.274 \times 10^{-24}\ \mathrm{J/T}$
a_0	Bohr radius	$5.292 \times 10^{-11}\ \mathrm{m}$
u	Atomic mass constant	$1.661 \times 10^{-27}\ \mathrm{kg}$
k_B	Boltzmann constant	$1.381 \times 10^{-23}\ \mathrm{J/K}$

Chapter 1 Introduction

It has been a long-standing goal in physics to gain a high degree of control over a quantum system to mimic – or to *simulate* – another quantum system of interest which lacks a high degree of controllability [1]. The realization of such a quantum simulator can be useful in order to gain a better understanding of hard-to-change quantum systems whose complex behavior is classically hard to compute. Systems whose investigation by quantum simulation were proposed are typically systems from condensed-matter physics, ranging from Hubbard models to high-T_c superconductivity and quantum phase transitions, but also applications of quantum simulators in other fields of physics were proposed, such as in cosmology, in high-energy physics or in chemistry [2].

One experimental platform which, due to the high degree of control over its properties, allows for the realization of a quantum simulator are ultracold atoms [3, 4]. The production of ultracold atomic gases at sub-μK temperatures and atomic densities of up to $10^{14}\,\mathrm{cm}^{-3}$ is nowadays routinely achieved in laboratories worldwide by laser cooling techniques [5–10]. A wide variety of elements, ranging from alkali atoms [11] to alkaline-earth atoms [12], lanthanides [13] and noble gases [14] can now be cooled down by laser cooling techniques. Both bosonic [15–17] and fermionic [18] cold atomic gases can be brought to quantum degeneracy, and the sign and strength of interatomic interactions can be tuned for example by Feshbach resonances [19]. The cold atoms can be held in optical lattices which are formed by the standing waves of laser beams with controllable geometry, and imaging of the cloud with single-atom resolution has been achieved [20].

Ultracold atoms in Rydberg states are one particularly promising candidate for the realization of quantum simulators [21, 22]. Rydberg states, which are electronic states with high principal quantum numbers $n \gtrsim 10$, have properties which are strongly dependent on and such tunable by n, such as their huge geometric sizes and polarizabilities in static electric fields [23]. Most notably, interactions between Rydberg atoms are several orders of magnitude larger than interactions between ground-state atoms, and their sign, strength, angular dependence and distance dependence behavior can be controlled by the choice of the Rydberg state or by applying an additional electric field [24, 25]. The large Rydberg interactions lead to a phenomenon called Rydberg blockade in which the Rydberg state of a second nearby atom is shifted out of resonance when being subject to a narrow-band Rydberg excitation laser [26–29]. Rydberg atoms in optical lattices with single-atom detection resolution [30] have been used to realize

an Ising-type Hamiltonian [31]. It is also possible to use single or a few Rydberg atoms in controlled geometries [32] to study Rydberg interactions [33–35] or to build more complicated geometries for quantum simulation applications [36, 37]. Atomic ground states can be admixed with a weak Rydberg character, which leads to a controllable and strongly interacting but long-lived atomic system. This technique which is called Rydberg dressing [38–41] was realized in a few proof-of-principle experiments [42–44], but further research possibilities seem to be ample. Other research fields of interest regarding cold Rydberg atoms are in the field of the engineering and usage of optical nonlinearities due to the strong Rydberg interactions [45–47], the study of dipole-mediated energy transport [48], the creation of single-particle sources [49, 50] or quantum computing [51, 52].

Most of the research in the field of ultracold Rydberg atoms so far has been conducted with alkali atoms, while the number of groups working on ultracold alkaline-earth atoms in Rydberg states is limited [53–55]. Alkaline-earth atoms in Rydberg states, as two-electron systems, offer intriguing possibilities in quantum simulation, but are not well explored yet. The second valence electron allows for trapping [56] and imaging techniques of Rydberg atoms [57, 58] which are not present in the alkali atoms. Two-electron atoms have long-lived metastable states and associated narrow intercombination lines. If one of these lines is used as the lower transition in a typically employed two-photon excitation scheme to Rydberg states, it can be used to decrease the associated decoherence rate, as compared to alkali atoms. Two-electron Rydberg atoms also feature doubly-excited perturber states [59]. There are also quantum simulation proposals only regarding alkaline-earth atoms [60–63].

Strontium is a particularly interesting candidate for two-electron atoms, as efficient laser cooling techniques were established for this species [64, 65]. Strontium could for the first time be cooled in a magneto-optical trap (MOT) operating on its broad closed transition in Japan in 1990 [66], only three years after the realization of the first MOT of any species ever produced [67]. The first strontium MOT operating on its narrow intercombination closed transition was then realized in 1999 in Japan [68] and at NIST in the US [69]. Due to the low Doppler temperature of the narrowband MOT without any evaporative cooling high phase-space densities of 0.1 in an optical dipole trap could be achieved [70], as well as temperatures of 250 nK [71, 72].

The first strontium Bose-Einstein condensates (BECs) were created in 2009 by the groups of F. Schreck in Innsbruck (now in Amsterdam) [73] and of T. Killian in Houston [74]. The central trick was to use the ^{84}Sr isotope for the last evaporative cooling step, which is the strontium isotope with the lowest natural abundance but with the most favorable s-wave scattering length for evaporative cooling. Such, strontium was the third species with two valence electrons which was cooled down to quantum degeneracy, after ytterbium in 2003 in Kyoto [75]

and calcium in 2009 at PTB in Braunschweig [76]. In 2010 all other stable isotopes of strontium were brought to quantum degeneracy, namely the boson ^{86}Sr [77], the boson ^{88}Sr [78] and the fermion ^{87}Sr [79, 80]. However, the largest strontium BECs so far were attained with the original ^{84}Sr isotope, see an article which summarizes the laser cooling techniques developed in the group of F. Schreck in 2009-2012 [81]. With this isotope, it was also possible to create the first BEC without evaporative cooling [82].

Currently, the main interest in ultracold strontium atoms from the scientific community stems from its application in optical lattice clocks [83–86], which were recently reviewed in Ref. [87]. The related sensitive measurements can have important potential applications in geodesy [88], the search for dark matter [89] or gravitational wave detection [90]. Other research interests in ultracold strontium atoms include the quest for polar open-shell molecules [91], Sr-Sr molecules [92, 93], precision measurements of gravity [94], fundamental atom-light interactions [95, 96] and the quest for a continuous atom laser [12].

This thesis describes the strontium Rydberg experiment which was set up from scratch since 2014 at the USTC Shanghai Institute for Advanced Studies, which belongs to the University of Science and Technology of China. In Chapter 2 the experimental setup is described, which encompasses the ultra-high vacuum system, the magnetic field sources and the laser systems required for cooling, repumping and Rydberg excitation of strontium atoms. In Chapter 3 a two-dimensional magneto-optical trap (2D-MOT) is described, which serves as a source of a cold strontium atomic beam. In Chapter 4 further cooling steps in our experiment are described. This includes the MOT operating on the broad closed transition of strontium and the effect of a repumping beam operating on the $5s5p\,^3P_2 \rightarrow 5p^2\,^3P_2$ transition at 481 nm. This chapter includes a short description of a MOT operating on the narrow closed transition. Then in Chapter 5 a short introduction into Rydberg physics is given, and our first experimental results regarding Rydberg excitations of ultracold strontium atoms are described. Finally, a summary of the results of this thesis as well as an outlook on future research is given in Chapter 6.

Chapter 2 Experimental setup

The wavelength meter-based frequency stabilization scheme shown in Sec. 2.4 is described in greater detail in the following publication:
Luc Couturier, Ingo Nosske, Fachao Hu, Canzhu Tan, Chang Qiao, Y. H. Jiang, Peng Chen, and Matthias Weidemüller. Laser frequency stabilization using a commercial wavelength meter. *Rev. Sci. Instrum.* 89, 043103 (2018).

In this chapter the employed experimental setup in our laboratory is described, which is used for cooling, trapping and for Rydberg excitation of strontium atoms. First in Sec. 2.1 the properties of strontium atoms are described which are most relevant for our experiment. After this, the design considerations and the setup of the ultra-high vacuum system in which the experiments take place are described in detail in Sec. 2.2. The setups for the generation of magnetic fields, which are required in our experiment, are described in Sec. 2.3. This chapter is then concluded by a description of the laser system which is required for cooling, trapping and for Rydberg excitation of strontium atoms in Sec. 2.4.

2.1 Strontium

In the following the physical aspects of strontium atoms which are most relevant in our experiment are described. For a more extensive description of various properties of strontium see for example the thesis of S. Stellmer [97], or a review article about degenerate quantum gases of strontium by the same first author [64].

In Sec. 2.1.1 the chemical and nuclear properties of strontium are shortly described. The most relevant electronic levels and transitions for our experiment are introduced in Sec. 2.1.2. This is followed by a description of the dramatically different properties of the two transitions which are used for laser cooling in Sec. 2.1.3, which follows from their very different natural linewidths. After that metastable states of strontium, as well as repumping strategies from them when performing laser cooling, are discussed in Sec. 2.1.4. This is followed by a short layout of our laser cooling strategy in Sec. 2.1.5

2.1.1. Chemical and nuclear properties

Strontium is a soft silvery metal which rapidly oxidizes, and such changes its chemical properties, if it is exposed to air. To maintain pure metallic strontium, which is shown in Fig. 2.1 (a), its exposure to air such has to be minimized, which is possible by storing it in a protective atmosphere as for example argon. When putting it into an oven or a heat pipe, then this has to be done fast if air is present, or even better inside a glove box which is filled with a protective atmosphere.

Strontium has a low saturated vapor pressure, if compared to the alkali atoms, with its melting point being at 777 °C and its boiling point at 1382 °C [98]. According to Refs. [97, 99], who use the values from Ref. [100], the saturated vapor pressure for solid strontium is given by: ①

$$\log_{10}(P[\mathrm{mbar}]) = 10.62 - 9450/T[K] - 1.31\log_{10}(T[K])\ . \tag{2.1}$$

The saturated vapor pressure and the corresponding atomic density $n_a = P/k_B T$ are plotted in Fig. 2.1 (b) and (c). To achieve the same vapor pressure like the commonly used element in laser cooling applications rubidium at room temperature, which is about 3×10^{-7} mbar [105], strontium has to be heated to a temperature of about 430 °C, according to Eq. (2.1).

Strontium atoms have 38 protons and such one more than rubidium atoms. An overview over the four stable isotopes of strontium, their quantum statistics, nuclear spins and natural abundances is given in Table 2.1. ^{88}Sr is the most abundant isotope and thus well-suited for experiments which work with natural-abundance strontium and for which no peculiar property of a certain isotope is needed. Its s-wave scattering length is -1 a_0 [97] and thus close to zero, which makes it well-suited for certain metrological applications such as precision measurements of the gravitational acceleration g [94]. Just as all the other bosonic isotopes, ^{88}Sr has no nuclear spin and such no hyperfine structure. The fermionic isotope ^{87}Sr has a nuclear spin $I = 9/2$ which is the highest of all stable alkaline-earth isotopes. It is commonly used in optical lattice clocks based on strontium atoms [83, 86], due to its vanishing s-wave scattering at low temperatures which prevents collisional shifts and as it possesses a more useful clock transition than its bosonic counterparts due to hyperfine mixing [87]. The bosonic isotope ^{84}Sr

① There are also other values given in the literature, for example in Table 2 in Ref. [101], who give the formula $\log_{10}(P[\mathrm{atm}]) = 9.226 - 8572/T[\mathrm{K}] - 1.1926\log_{10}(T[\mathrm{K}])$ for the saturated vapor pressure of solid strontium. This equation gives an about three orders of magnitude higher pressure than Eq. (2.1). It is consistent with the formula used by [102]. On the other hand, Eq. (2.1) seems to agree better with the given temperature-dependent atomic density of Dinneen *et al.* 1999 [103] and with the measured vapor pressure of Courtillot *et al.* 2003 [104], so it is used throughout this thesis. However, it shall be kept in mind that the vapor pressure value is subject to a considerable uncertainty.

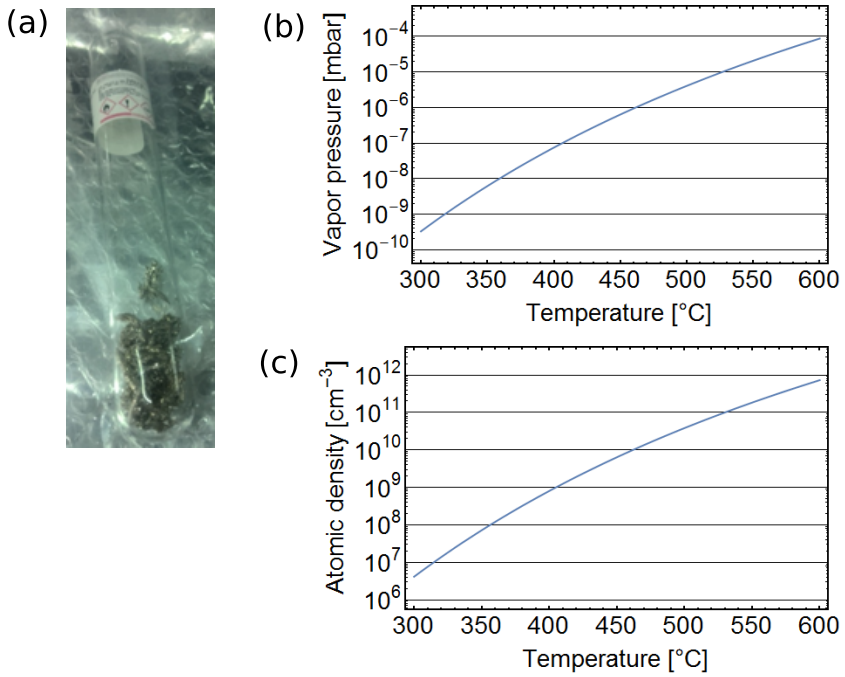

Fig. 2.1 Chemical properties of strontium. (a) Solid strontium chunks in a protective argon atmosphere. (b) The saturated vapor pressure and (c) the atomic density of strontium versus temperature.

isotope has the lowest natural abundance, but with an s-wave scattering length of $124\ a_0$ it is most suited for evaporative cooling to quantum degeneracy, as this scattering length lies in a good intermediate regime between the two extremes of no sufficient interatomic thermalization and a too high three-body collision rate which expels atoms from the shallow trap [97].

Isotope	Statistics	Nuclear spin	Abundance [98]
^{88}Sr	bosonic	0	82.58 %
^{87}Sr	fermionic	9/2	7.00 %
^{86}Sr	bosonic	0	9.86 %
^{84}Sr	bosonic	0	0.56 %

Table 2.1 Quantum statistics, nuclear spins and natural abundances for all stable isotopes of strontium.

2.1.2. Electronic level scheme

An overview over the most important electronic levels and the addressed transitions of the strontium atom in our experiment is shown in Fig. 2.2. In the level scheme hyperfine structure levels are not shown, as they do not exist for bosonic isotopes of strontium which have zero nuclear

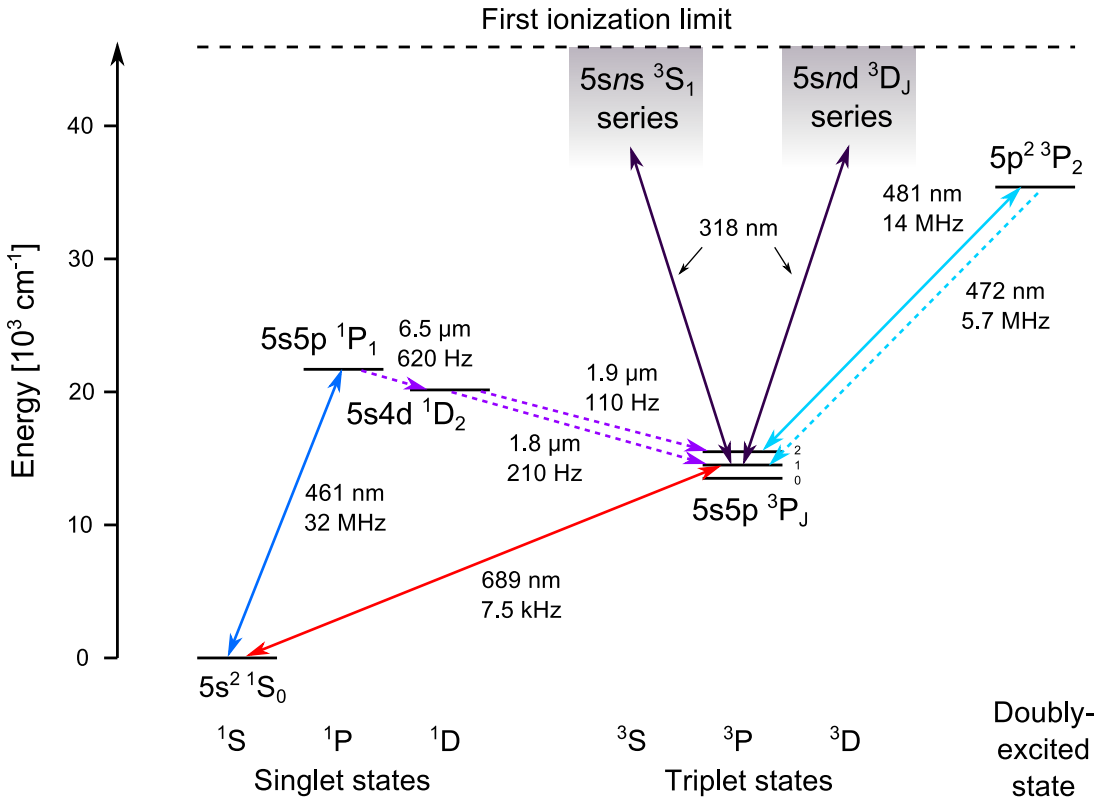

Fig. 2.2 Level scheme with all addressed transitions in our experiment. Spectroscopic parameters in this figure are taken from Ref. [98], while decay rates involving the $5s4d\,{}^1D_2$ state can be found in Ref. [106]. Solid double-sided arrows are drawn for transitions which are addressed by laser beams in our experiment, while dotted single-sided arrows denote decay paths of transitions which are not addressed by laser beams. The vertical positions of the energy level manifolds are drawn to scale, while the finestructure splittings are exaggerated.

spins ($I = 0$). For a good description of the hyperfine structure of the fermionic isotope ^{87}Sr ($I = 9/2$) refer to Ref. [97]. Apart from the absence of hyperfine structure for bosonic isotopes, the singlet states ($S = 0$) also do not have a fine structure, which makes the electronic level scheme particularly simple. For most measurements presented in this thesis the bosonic isotope ^{88}Sr was used.

Strontium has two closed or nearly closed transitions from its ground state: The broad $5s^2\,{}^1S_0 \rightarrow 5s5p\,{}^1P_1$ transition at 461 nm with a natural linewidth of $\Gamma_{461}/2\pi = 32$ MHz, and the narrow $5s^2\,{}^1S_0 \rightarrow 5s5p\,{}^3P_1$ transition at 689 nm with a natural linewidth of $\Gamma_{689}/2\pi = 7.5$ kHz. These two transitions are such useful for laser cooling applications, which generally require closed transitions [5]. The 461 nm and the 689 nm transitions are called the blue and the red transitions in the following and throughout this thesis, as it is common in the literature about strontium atoms.

The blue transition is not completely closed, as the upper $5s5p\,{}^1P_1$ state decays to the

$5s4d\,^1D_2$ state with a measured decay rate of $\Gamma_{^1P_1\rightarrow{}^1D_2} = 3.85(1.47)\times 10^3\ s^{-1}$ [107], which corresponds to a branching ratio of approximately 1:50,000 if compared to the large decay rate to the ground state. The $5s4d\,^1D_2$ state then decays further to the metastable triplet states $5s5p\,^3P_2$ and $5s5p\,^3P_1$, with the calculated branching ratio to the $5s5p\,^3P_2$ state being $B_{^1D_2\rightarrow{}^3P_2} \simeq 1{:}3$ [108]. While the $^3P_1$ state decays on a relatively short time of 21 μs, the $^3P_2$ state has a lifetime on the order of 100 s in a room temperature environment (for more details on the metastable state lifetimes see Sec. 2.1.4). In summary, every approximately 150,000$^{\text{th}}$ time an atom being driven on the blue transition falls into the long-lived $^3P_2$ state.

From that state an atom can be transferred back to the ground state by exciting it to the doubly-excited $5p^2\,^3P_2$ state via a repumping beam at 481 nm [64, 109]. The two main decay channels from this state are the decays to the $5s5p\,^3P_2$ state with $\Gamma_{481}/2\pi = 14$ MHz and to the $5s5p\,^3P_1$ state with $\Gamma_{472}/2\pi = 5.7$ MHz [98]. After decaying to the $5s5p\,^3P_1$ state an atom will then decay further to the ground state on the time scale of 21 μs. From these decay rates it follows that each atom has to scatter $(\Gamma_{481}+\Gamma_{472})/\Gamma_{472} \simeq 3.5$ repumping beam photons on average to return back to the ground state. Additional comparably strong decay channels from the $5p^2\,^3P_2$ state do not exist, as there are no other dipole-allowed single-photon transitions leading to lower states. [②] The dipole-forbidden decay to the $5s5p\,^1P_1$ state is much weaker [98] and would even be beneficial for this repumping scheme.

The last type of transition which is addressed in our experiment is the transition from the $5s5p\,^3P_1$ state to a Rydberg state. To reach ionization threshold, the absorption of an ultraviolet (UV) photon with wavelength 318 nm is needed. From the $5s5p\,^3P_1$ state, three Rydberg series can be accessed via single-photon dipole-allowed transitions: The $5sns\,^3S_1$ series, the $5snd\,^3D_1$ series and the $5snd\,^3D_2$ series.

If strontium atoms should be excited to singlet Rydberg series, then this is possible by the absorption of a 413 nm photon from the $5s5p\,^1P_1$ state [53, 58]. However, only triplet Rydberg states are accessed in our experiment, as we want to benefit from the narrower natural linewidth of the lower $5s^2\,^1S_0 \rightarrow 5s5p\,^3P_1$ transition which can be beneficial in a two-photon $5s^2\,^1S_0 \rightarrow 5s5p\,^3P_1 \rightarrow \text{Ry}$ excitation scheme.

2.1.3. The two laser cooling transitions

The dipole-forbidden closed intercombination $^1S_0 \rightarrow {}^3P_1$ transition has a natural linewidth of $\Gamma_{689}/2\pi = 7.5$ kHz which is $\approx$ 4300x lower than the linewidth of the dipole-allowed closed $^1S_0 \rightarrow {}^1P_1$ transition with a natural linewidth of $\Gamma_{461}/2\pi = 32$ MHz. Due to this reason these two transitions which are used for laser cooling have very different properties. The most

[②] Also the $4d5p\,^3D_J$ ($J = 1, 2, 3$) manifold lies slightly higher in energy than the $5p^2\,^3P_2$ state [110].

	$5s^2\ {}^1S_0 \rightarrow 5s5p\ {}^1P_1$	$5s^2\ {}^1S_0 \rightarrow 5s5p\ {}^3P_1$
Vacuum wavelength $\lambda = 1/\tilde{\nu}$	460.862 nm	689.449 nm
Natural linewidth $\Gamma/2\pi$	$32.0^{+0.5}_{-0.5}$ MHz	$7.5^{+0.1}_{-0.2}$ kHz
Natural lifetime $\tau = 1/\Gamma$	5.0 ns	21 μs
Maximum acceleration $a_{\max} = \frac{\Gamma}{2}\frac{\hbar k}{m}$	$9.9 \times 10^5\ \mathrm{m/s^2}$	$150\ \mathrm{m/s^2}$
Saturation intensity $I_{\mathrm{sat}} = \frac{\pi c}{\sigma_0}\frac{\hbar\Gamma}{\lambda}$	$43\ \mathrm{mW/cm^2}$	$3.0\ \mu\mathrm{W/cm^2}$
Doppler temperature $T_D = \frac{\hbar\Gamma}{2k_B}$	770 μK	0.18 μK
Recoil temperature $T_R = \frac{\hbar^2 k^2}{k_B m}$	1.0 μK	0.46 μK

Table 2.2 Properties of the two laser cooling transitions for ^{88}Sr. The vacuum wavelengths and natural linewidths are computed from the wave numbers and transition probabilities from Ref. [98], while all other values in this table are derived from them.

important properties of the blue and red closed transitions are summarized in Table 2.2. For a more extensive overview refer to the table in the Appendix A.1.

In particular the narrow dipole-forbidden transition has a few interesting properties which are discussed more in detail in the following:

(i) The maximum acceleration of a light field on that transition is comparably low, with $a_{\max} = \frac{\Gamma}{2}\frac{\hbar k}{m} = 150\ \mathrm{m/s^2}$, while m is the mass of a strontium atom and $k = \lambda/2\pi$ is the wavenumber of the transition with the transition wavelength λ. The maximum acceleration is such only about 15-times larger than the acceleration due to gravity and falls below the gravitational acceleration from an absolute detuning of about 20 kHz on, with respect to the atomic transition and if no power or other broadening mechanisms are present.

(ii) Already small effects can introduce level shifts on the order of the natural linewidth, for example velocities with $v_\Gamma = \Gamma/k = 5.2\ \mathrm{mm/s}$ due to the Doppler shift or magnetic fields with $B_\Gamma = \Gamma/(\frac{\mu_B}{h} g_J) = 3.6\ \mathrm{mG}$ due to the Zeeman shift, with $g_J = 1.5$ being the Landé factor of the $^3P_1$ state.

(iii) If an atom scatters a photon on that transition then it gains a recoil velocity of $v_R = \hbar k/m = 6.6\ \mathrm{mm/s}$. This corresponds to a Doppler shift of $kv_R/2\pi = 10\ \mathrm{kHz}$ which is larger than the natural linewidth. Thus, a single scattering event can kick an atom out of resonance.

(iv) The saturation intensity $I_{\mathrm{sat}} = \frac{\pi c}{\sigma_0}\frac{\hbar\Gamma}{\lambda} = 3.0\ \mu\mathrm{W/cm^2}$, with the on-resonant absorption cross section $\sigma_0 = 3\lambda^2/2\pi$, is comparably low.

(v) The Doppler temperature $T_D = \frac{\hbar\Gamma}{2k_B} = 0.18\ \mu\mathrm{K}$ is very low and even below the recoil temperature $T_R = \frac{\hbar^2 k^2}{k_B m} = 0.46\ \mu\mathrm{K}$. This results in very low achievable temperatures if performing laser cooling on this transition [71, 72]. Conversely to this, the $^1\mathrm{S}_0 \rightarrow {}^1\mathrm{P}_1$ transition has a five times larger linewidth than the D_2 line of rubidium [105], which results in a five times larger Doppler temperature than rubidium of $770\ \mu\mathrm{K}$.

2.1.4. Metastable states and repumping

The $5\mathrm{s}5\mathrm{p}\,{}^3\mathrm{P}_J$ ($J = 2, 1, 0$) metastable states of the strontium atom are very long-lived, as only the ground state $5\mathrm{s}^2\,{}^1\mathrm{S}_0$ has a lower energy than these states, and as single-photon transitions to the ground state are dipole-forbidden. However, the metastable states still gain finite lifetimes due to higher-order processes [97, 111, 112].

The $5\mathrm{s}5\mathrm{p}\,{}^3\mathrm{P}_2$ state has a calculated lifetime of 1050 seconds (corresponding to 17 minutes), with the largest decay contribution being the magnetic-dipole (M1) decay to the relatively short-lived $5\mathrm{s}5\mathrm{p}\,{}^3\mathrm{P}_1$ state [113]. The actual experimental lifetime of its low-field seeking m_J states in a magnetic trap [114] was, however, measured to be dependent on the temperature of the environment. In room-temperature environments, according to Ref. [115], the effective lifetime of the $5\mathrm{s}5\mathrm{p}\,{}^3\mathrm{P}_2$ state is limited to the order of 100 s due to black-body coupling to subsequently decaying slightly higher-lying $5\mathrm{s}4\mathrm{d}\,{}^3\mathrm{D}_J$ states. Its extrapolated lifetime in the limit of zero temperature of 520 s, on the other hand, appears to roughly agree with the theoretical value [113, 115].

A small fraction of the fast decaying $5\mathrm{s}5\mathrm{p}\,{}^1\mathrm{P}_1$ singlet state is mixed into the $5\mathrm{s}5\mathrm{p}\,{}^3\mathrm{P}_1$ triplet state due to spin-orbit interaction [111, 112]. Such, there is an electric-dipole (E1) decay to the ground state with linewidth $\Gamma_{689}/2\pi = 7.5$ kHz [98], which is large if compared to the decay rates from the other two longer-lived metastable states.

The $5\mathrm{s}5\mathrm{p}\,{}^3\mathrm{P}_0$ state of bosonic isotopes has a calculated lifetime of thousands of years, with the dominant decay channel being the electric-dipole magnetic-dipole (E1M1) two-photon decay to the ground state. In the case of the fermionic isotope ^{87}Sr, with nuclear spin $I = 9/2$, the ${}^3\mathrm{P}_0$ state is coupled with the ${}^1\mathrm{P}_1$ and ${}^3\mathrm{P}_1$ states with their E1 decays to the ground state, and such gains a shorter lifetime on the order of 100 s, which corresponds to a natural linewidth of $\Gamma_{698} \sim 1$ mHz [111, 112]. The E1 transition of the fermionic isotope is used for strontium optical lattice clocks [83–86], due to which the $5\mathrm{s}5\mathrm{p}\,{}^3\mathrm{P}_0$ state is also called the clock state.

For practical considerations of our laser cooling experiment, which usually takes place on a seconds timescale, the ${}^3\mathrm{P}_2$ and ${}^3\mathrm{P}_0$ states such have an infinite lifetime, while the ${}^3\mathrm{P}_1$ state, with a lifetime of 21 μs, decays relatively fast. It was already mentioned before that every approximately 150,000$^{\mathrm{th}}$ atom in the blue cooling cycle ecays to the ${}^3\mathrm{P}_2$ state. To overcome

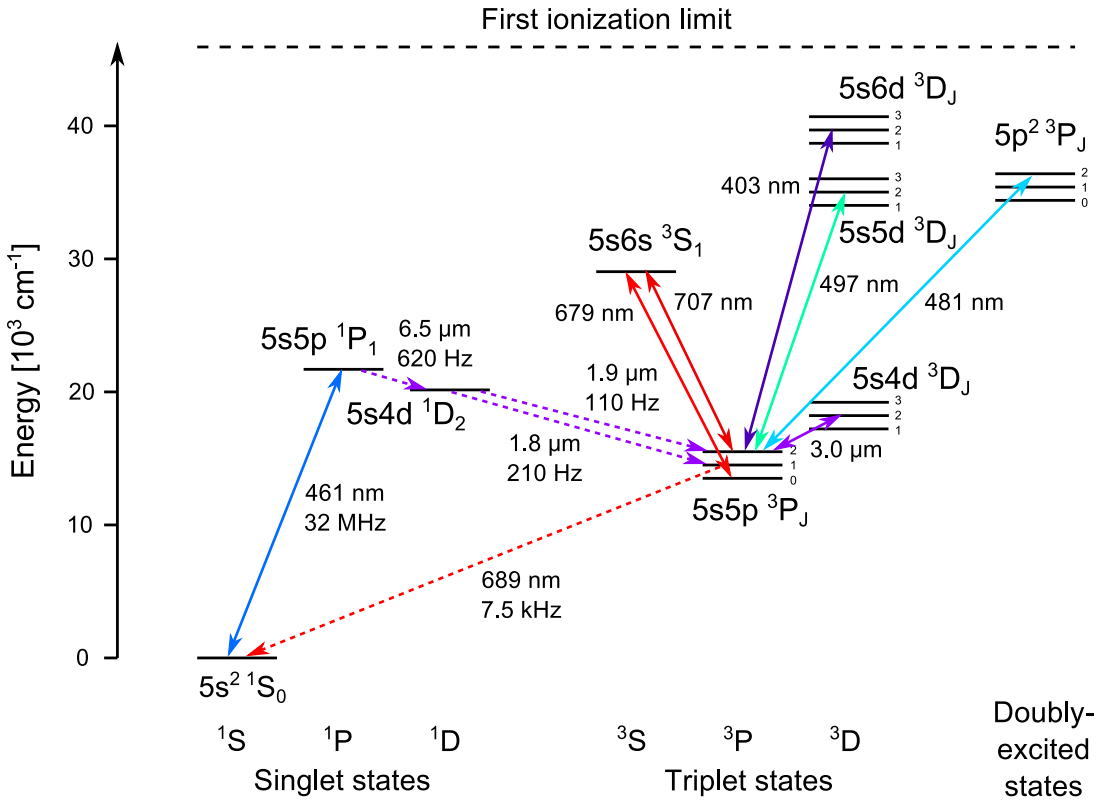

Fig. 2.3 Level scheme with alternative repumping transitions from the metastable states. The vertical positions of the energy level manifolds are drawn to scale, while the finestructure splittings are exaggerated.

the problem of $^3\mathrm{P}_2$ atom accumulation during cooling on the blue transition, a few repumping schemes were developed, see the level scheme in Fig. 2.3 for an overview.

The earliest repumping scheme addresses the $5\mathrm{s}5\mathrm{p}\,^3\mathrm{P}_2 \rightarrow 5\mathrm{s}6\mathrm{s}\,^3\mathrm{S}_1$ transition at 707 nm and the $5\mathrm{s}5\mathrm{p}\,^3\mathrm{P}_0 \rightarrow 5\mathrm{s}6\mathrm{s}\,^3\mathrm{S}_1$ transition at 679 nm [103]. Also addressing the second transition is needed for efficient repumping, as the branching ratio of the $5\mathrm{s}6\mathrm{s}\,^3\mathrm{S}_1 \rightarrow 5\mathrm{s}5\mathrm{p}\,^3\mathrm{P}_0$ transition is relatively large [98].

Apart from this two-photon scheme also a few single-photon repumping schemes exist: Repumping via the $5\mathrm{s}5\mathrm{d}\,^3\mathrm{D}_2$ state at 497 nm [99, 109, 116], via the $5\mathrm{s}4\mathrm{d}\,^3\mathrm{D}_2$ state at 3012 nm [117], via the $5\mathrm{s}6\mathrm{d}\,^3\mathrm{D}_2$ state at 403 nm [109] and, as realized in our experiment, via the $5\mathrm{p}^2\,^3\mathrm{P}_2$ state at 481 nm were realized. The repumping transition at 481 nm was also used in the laboratories of T. Killian in Houston before.

2.1.5. Laser cooling strategy

In our laboratory, we heat strontium chunks to a high temperature of $450 \ldots 500\ ^\circ\mathrm{C}$, to create a sufficiently dense strontium gas. The relatively slow atoms of that strontium gas are decelerated in a transversely loaded two-dimensional magneto-optical trap (2D-MOT) [118, 119].

It operates on the broad blue transition which due to its larger natural linewidth allows to slow down more atomic velocity classes than if the 2D-MOT would be operated on the red transition. Additionally to the 2D-MOT cooling beams, a counter-propagating Zeeman slower beam can enhance the captured flux in the 2D-MOT [119, 120].

The two-dimensionally trapped atoms in the 2D-MOT are then accelerated by a blue pushing beam along the third direction which creates a slow atomic beam. It is used to load a 3D-MOT which also operates on the blue transition. This one is called the broad-line MOT or *blue MOT* [66, 103, 106, 121–125]. As the Doppler temperature on the blue transition is with 770 μK relatively high, we then create a 3D-MOT at the same position on the red transition, which is called the narrow-line MOT or *red MOT*. It can further cool down the atoms by about three orders of magnitude, due to the much narrower linewidth of that transition [68, 69, 71, 72, 126–129].

2.2 Vacuum system

The experiments on ultracold strontium atoms take place in an ultra-high vacuum (UHV) system. An ultra-high vacuum is required in order to ensure that the cold atoms do not collide with background atoms during the time scale of one experimental cycle, which for strontium setups typically lasts for up to a few tens of seconds [81]. The goal was to create a vacuum in the 10^{-11} mbar range at the position of the final experiments. The challenge is to create an ultra-high vacuum and at the same time having a high atomic flux and good optical access in the experiment region. Vacuum systems of other strontium setups are for example described in Refs. [97, 130–132].

An overview over the entire vacuum system is given in Sec. 2.2.1. This is followed by a more detailed description of the 2D-MOT chamber in Sec. 2.2.2 and by the science chamber in Sec. 2.2.3.

2.2.1. Overview

An overview over the elements of the vacuum system in our experiment is shown in Fig. 2.4 (a). It is a two-chamber system, consisting of the 2D-MOT chamber which contains the cold atom source [118, 119], and the science chamber in which experiments on the cold atoms are performed. The two chambers are separated from each other by a differential pumping tube, with diameter $D = 2.0\,\mathrm{mm}$, length $L = 22.8\,\mathrm{mm}$ and a conductance for air at room temperature of $C_{\mathrm{tube}}[\mathrm{l/s}] = 12.1 \times D^3[\mathrm{cm}]/L[\mathrm{cm}] = 0.042\,\mathrm{l/s}$ [133]. It leads to a differential pumping factor of $S_{\mathrm{gas}}/C_{\mathrm{tube}}$ for the gas-specific pumping speed S_{gas} in the chamber with lower pres-

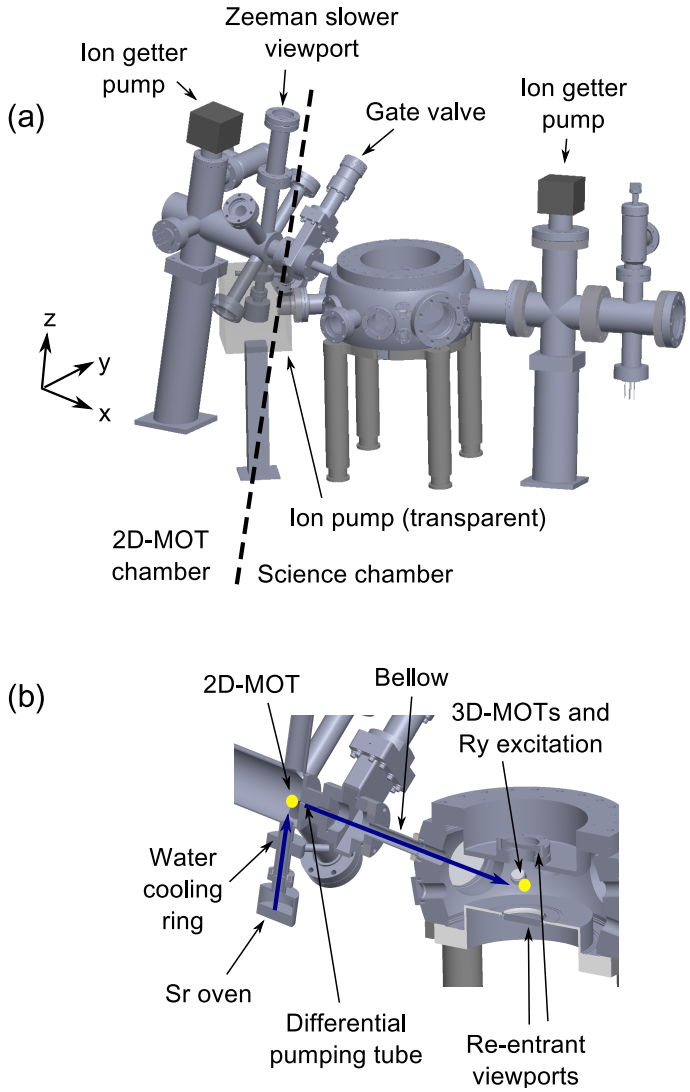

Fig. 2.4 Vacuum system. (a) Overview over the entire vacuum system, which consists of the 2D-MOT chamber and the science chamber. (b) A cut along the plane of the trajectory of a strontium atom which is emitted from the oven, stopped and deflected in the 2D-MOT, and then trapped in the (3D-)MOTs.

sure. Its entry aperture is located 14 mm downstream from the 2D-MOT position, see Fig. 2.4 (b) (dimensions as in Ref. [120]). The differential pumping tube is designed to allow the science chamber to have a lower pressure than the 2D-MOT chamber, which due to its contained strontium chunks and its heated oven and Zeeman slower viewport parts was expected to have a higher pressure.

All vacuum pieces are joined together by standard ConFlat (CF) flanges, in which hard steel knife edges cut into soft-material (typically copper) gaskets and thus ensure tight joints. The total system is ~ 120 cm long, ~ 50 cm wide and up to ~ 70 cm high. The center of the science chamber is located 35 cm above the optical table. The 2D-MOT chamber and a vacuum piece connecting to the science chamber are supported by hollow steel cylinders which are

welded to their bottoms. Additionally, the heavy ($\sim 20\,\mathrm{kg}$) science chamber is supported by four steel pedestals with diameter $47\,\mathrm{mm}$, and the magnets of an ion pump connected to the science chamber are supported by a simple hollow aluminum cylinder.

Nearly all viewports are equipped with customized 3 mm thick steel adapters between the screw heads and the viewport steel surfaces during assembly. They allow for the mounting of cage systems from Thorlabs holding small optics assemblies, i.e. a 60 mm (30 mm) [16 mm] cage system on a CF63 (CF40) [CF16] viewport.

2.2.2. 2D-MOT chamber

The main piece (LEOSolutions) of the 2D-MOT chamber is a steel piece which provides eight flanges with direct lines of sight to the 2D-MOT trappiong region: four of them are used for CF40 cooling beam viewports, additional two flanges are used for the strontium oven (CF16) and the Zeeman slower viewport (CF40), and the remaining two CF40 flanges are used for the pushing beam viewport and the connection to the science chamber. Additionally, this main piece provides flanges for the connection of an ion getter pump (SAES Getters, NEXTorr D 200-5), an ion gauge (Agilent, UHV-24p) and a CF40 all-metal angle valve (MDC Vacuum Products, 314003). The pump includes an ion pump, with a pumping speed of $\sim 6\,\mathrm{l/s}$ for all gas types, as well as a non-evaporative getter (NEG) pump, which exerts different pumping speeds for different reactive gas types, with a maximum of $200\,\mathrm{l/s}$ for H_2 and O_2. While the NEG element only removes reactive gases like H_2, H_2O and N_2 from the system by chemical sorption into the getter material (St 172), the ion pump also removes non-reactive gases such as Ar or CH_4 from the system by ionization and subsequent ion acceleration into a getter material [134].

The strontium oven is connected to the main piece by a nickel gasket, as nickel is preferred over copper at high temperatures. The oven is a simple cylinder with a height of $\sim 20\,\mathrm{mm}$ and an inner diameter of $\sim 47\,\mathrm{mm}$. The oven aperture is 125 mm below the 2D-MOT position, to which it is connected by a tube with an inner diameter of 16 mm. The oven is heated by a Nichrome (80% Ni, 20% Cr) resistive heating wire, with a diameter of $0.5\,\mathrm{mm}$, a $0.25\,\mathrm{mm}$ thick electrical insulation made of glassfiber and a maximum specified temperature of $800\,^\circ\mathrm{C}$ (Hangzhou Ualloy Materials). The heating wire is powered by a DC power supply. The readout thermocouple is welded inside the oven steel bulk below the strontium reservoir, and the oven is typically heated to $465\,^\circ\mathrm{C}$. A steel ring for water cooling welded around the tube leading to the oven helps to keep the steel temperature around the 2D-MOT trapping region below $30\,^\circ\mathrm{C}$. It would rise to $\sim 70\,^\circ\mathrm{C}$ at our typical oven operating temperature otherwise.

To avoid strontium deposition on the Zeeman slower viewport which is located $42\,\mathrm{cm}$ from the oven aperture, it is permanently heated to $330\,^\circ\mathrm{C}$. Details on its heating and its thermal

insulation box can be found in the Appendix A.2. All other viewports in the 2D-MOT chamber consist of Kodial glass and are not heated, as they do not have a direct line of sight to the oven. All viewports in the 2D-MOT chamber are covered with $\sim 430 - 700\,\mathrm{nm}$ anti-reflection coatings at both sides, except the Zeeman slower viewport which is only coated at its outer side, in order to avoid possible chemical reactions with incident strontium atoms.

After the differential pumping tube a CF40 gate valve (MDC Vacuum Products, E-GV-1500M) is placed to be able to separate the 2D-MOT and the science chambers from each other, for example when refilling strontium into the oven. It is followed by a CF16 bellow which connects to the science chamber and which allows for a fine-adjustment of the 2D-MOT chamber position, with respect to the science chamber, during assembly.

2.2.3. Science chamber

The science chamber is the central piece of the vacuum system. It should allow for good optical access, for convenient positioning of magnetic field systems and ideally for an electric field control and ion detection. The possibility of electric field and ion detection is particularly advantageous for experiments involving Rydberg atoms, due to the huge d.c. polarizability of Rydberg atoms scaling with n^7, with n being the principal quantum number of the Rydberg state [135], and the possibility of Rydberg atom ionization by electric fields with subsequent ion detection [136]. Electrodes for electric field control are preferred to be mounted inside the vacuum system, such that charging of glass near the electrodes does not become an issue [137], and also ion detectors require internal vacuum mounting. As this is more easily done inside a steel chamber, we decided to use a steel chamber instead of a glasscell. Apart from this a steel chamber is not as fragile as a glasscell, and possible accidents can be avoided. While an electrode and ion detection structure is not installed yet in our system, our science chamber offers the possibility for this. Designs for similar in-vacuo setups are described in Refs. [33, 132, 138, 139].

A model of the science chamber is shown from different angles in Fig. 2.5. It is a customized steel chamber (Kimball Physics) which offers 20 flanges. The two large flanges along the vertical axis have CF200 sizes and are connected to two re-entrant viewports of slightly different designs. The main reasons for using re-entrant viewport designs were the lower power consumption of MOT coils places inside their recessed buckets (see Sec. 2.3.2) and a higher numerical aperture for a possible future imaging system along the vertical axis. The diameter of the glass surface of the lower re-entrant viewport, which offers the highest numerical aperture to the atoms, is 50 mm. The upper re-entrant viewport is a CF200-CF40 steel adapter, with a standard CF40 viewport being connected to it. In the horizontal plane totally four CF63 flanges and six CF40 flanges are located, three of which are attached to tubes welded to the steel cham-

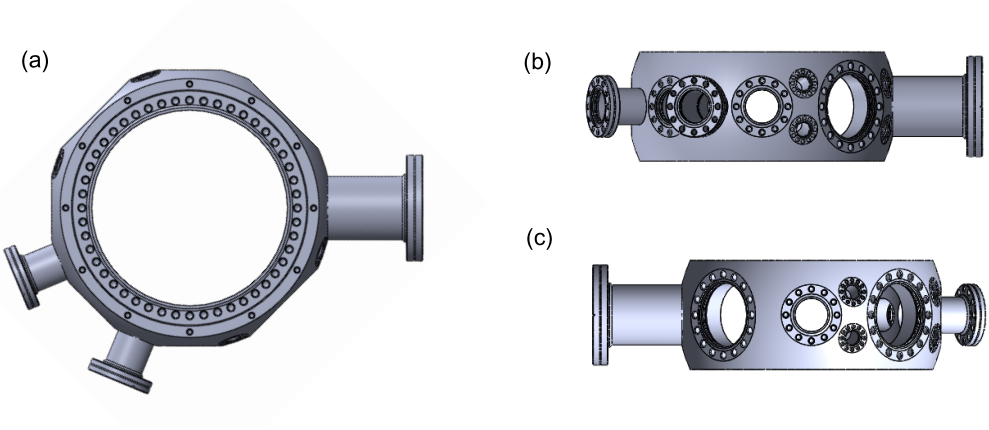

Fig. 2.5 Customized steel science chamber. (a) Top view. (b) Front view. (c) Rear view.

ber. Additionally, the chamber has eight CF16 flanges at angles of $\pm 10°$ towards the horizontal plane. An overview over the distances d_{vp}, radii r_{vp} and numerical apertures $\mathrm{NA} = \sin\theta$, with $\theta = \tan^{-1}(r_{\mathrm{vp}}/d_{\mathrm{vp}})$, of the science chamber viewports is shown in Table 2.3.

To one of the CF16 flanges, being out of the horizontal plane, the bellow leading to the 2D-MOT chamber is connected, in order to save optical access in the horizontal plane. The distance between the 2D-MOT and the 3D-MOT positions is 335 mm.

Most of the flanges of the horizontal plane are equipped with fused silica viewports with a customized multi-band anti-reflection coating for the wavelengths 318 nm, 461 nm, 532 nm, 689 nm and 1064 nm (Vacom). However, the actual coating performance is far from the original specifications, which makes its reflection properties similar to uncoated viewports. The CF16 flange opposite to the pushing beam is equipped with a sapphire viewport (MDC Vacuum Products).

Just like the 2D-MOT chamber, the science chamber is pumped by an ion getter pump (SAES Getters, NEXTorr D 500-5) and connected to an ion gauge (Agilent, UHV-24p) and a CF40 all-metal angle valve (MDC Vacuum Products, 314003). Additionally, a $20\,\mathrm{l/s}$ ion pump (Agilent, VacIon Plus 20 Starcell) is connected to it. The achieved pressure in the science chamber is with $1.7 \times 10^{-9}\,\mathrm{mbar}$, according to the ion gauge (around half that value according to the nearby NEXTorr ion pump current), higher than the target pressure, which is certainly due to a virtual leak in our science chamber region. It is paradoxically higher than the pressure in our 2D-MOT chamber, which after about one year of operation according to its ion pump current is $\sim 2 \times 10^{-10}\,\mathrm{mbar}$, if the oven is heated to $465\,°\mathrm{C}$. While the pressure in the science chamber slightly increased over time, the pressure in the 2D-MOT chamber decreased over time. The latter is possibly due to getter qualitites of strontium. For more details on the vacuum system installation and performance see the Appendix A.3.

At the achieved pressure in the science chamber the cold atom lifetime due to collisions

Viewport	Quantity	Distance [mm]	Radius [mm]	Numerical aperture
Re-entrant down	1	41	25	0.52
Re-entrant up	1	56	20	0.34
CF63	3	160	34	0.21
CF63 ext.	1	576	34	0.06
CF40	4	160	20	0.12
CF40 ext.	2	213	20	0.09
CF16	8	160	8	0.05

Table 2.3 Distances, radii and numerical apertures of the science chamber viewports.

with background atoms is measured to be ~ 8 s, see Sec. 4.4 for details. This agrees well with the order of magnitude of a few seconds at that pressure reported by other groups [114, 140, 141]. This collision-induced atom lifetime reduces the achievable atom number in our magnetic trap acting on the $^3\mathrm{P}_2$ state and also imposes an upper limit to the time of future evaporative cooling stages in an optical dipole trap. However, it is still low enough for a large variety of experiments.

2.3 Magnetic fields

The magnetic fields required for atom cooling and trapping for the 2D-MOT are introduced in Sec. 2.3.1, and for the 3D-MOT in Sec. 2.3.2.

2.3.1. 2D-MOT

For the strontium 2D-MOT, a two-dimensional quadrupolar magnetic field with a gradient of a few 10s of G/cm in its trapping region is required, while along the third axis the magnetic field should be zero. One possibility to generate such a magnetic field is the usage of four magnetic coils in the so-called Ioffe configuration [11]. However, inspired by similar designs [118, 120], we decided to realize the magnetic field by the usage of permanent magnets, which are compact, relatively easy to assemble and do not need a power supply.

The permanent magnet geometry and the used coordinate system are shown in Fig. 2.6 (a). We use N35 neodymium ($\mathrm{Nd_2Fe_{14}B}$) magnets. Each single magnet piece has dimensions of 25 mm $\times$ 10 mm $\times$ 3 mm and a magnetization of $6.6(1) \times 10^5$ $\mathrm{A/m}$ along its shortest axis. Four stacks of permanent magnets are located symmetrically around the chamber, with center distances of 75 mm and 88 mm in x and z directions, respectively. Each stack consists of nine magnets glued together along the y axis and has the dimensions $d_x = 25\,\mathrm{mm}$, $d_y = 27\,\mathrm{mm}$

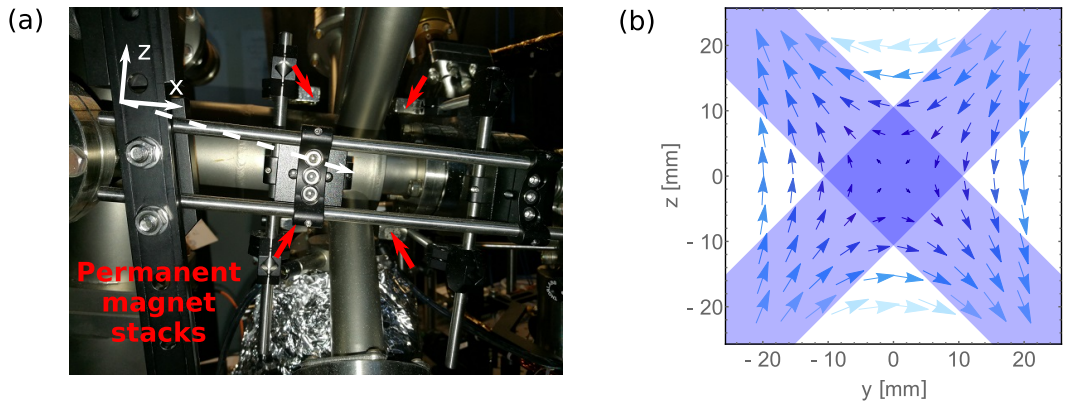

Fig. 2.6 Magnetic field generation for the 2D-MOT. (a) Photo of the four permanent magnet stacks in our setup. A coordinate system is introduced, with the origin being in the center of the 2D-MOT, and the third y axis (not shown) pointing into the plane. (b) Calculated magnetic field lines in the yz plane. The blue shaded areas denote the regions of the 2D-MOT cooling beams within their $1/e^2$ radii of 7.5 mm.

and $d_z = 10\,\mathrm{mm}$. The magnetization direction of the two upper stacks (positive y direction) is opposite to the one of the two lower stacks (negative y direction).

The resulting calculated magnetic field [142] in the yz plane is shown in Fig. 2.6 (b). While the magnetic field lines are perpendicular to the y axis at $z = 0$ and to the z axis at $y = 0$, they are parallel along the cooling beam directions which have $45°$ angles to the y and z axes in the yz plane. With the above stated geometry values, the permanent magnets generate a longitudinal magnetic field gradient along the cooling beam center directions of $\partial B_r/\partial r = 34\,\mathrm{G/cm}$, with $r = \sqrt{y^2 + z^2}$, in the 2D-MOT trapping region.

The maximum transverse B_y field versus z along the center line of the z axis (at $x, y = 0$) is 156 G at $z = -45\,\mathrm{mm}$. Its value varies across the tube between the oven and the 2D-MOT trapping region, which has a diameter of 16 mm, by up to around $\pm 25\,\%$. Assuming perfect alignment, the permanent magnets generate field gradients of $\partial B_r/\partial r \simeq 60\,\mu\mathrm{G}/(100\,\mu\mathrm{m})$ at the position of the 3D-MOT which is located 335 mm downstream in x direction.

As the cold atoms in the 2D-MOT accumulate on the zero line of the two-dimensional quadrupolar magnetic field and as they subsequently shall be accelerated through a differential pumping tube with a diameter of only 2 mm, the magnet positions have to be adjustable on this mm length scale. Because of this reason we glued the magnet stacks on a structure which is connected to one horizontal and one vertical translation stage, which delivers enough degrees of freedom to fine-tune the four stacks as a whole. After the four stacks are first positioned relative to each other carefully by hand, the position of the stack structure can be optimized by moving the translation stages and by observing the blue 2D-MOT fluorescence by eye through the pushing beam viewport, with the pushing beam being off. In this way the 2D-MOT can be

moved until it overlaps with the differential pumping tube on the x axis. Additionally to the degrees of freedom given by the two translation stages, the two magnet stacks on each x side can be slided by hand, if respective screws are loosened, in order to change the magnetic field gradient to up to 50 G/cm in our setup.

2.3.2. 3D-MOT

For the blue and the red 3D-MOTs a three-dimensional quadrupolar magnetic field in the trapping region is needed, which can be generated by anti-Helmholtz coils. One of the design criterions for our coils was that an axial magnetic field gradient $\partial B_z/\partial z$ of about 60 G/cm can be achieved, which is a typical gradient used during magnetic trap loading of strontium atoms in the $^3\mathrm{P}_2$ state [73, 74]. In this section the z axis denotes the gravity axis, unlike in the sections before in which z points along the slightly tilted (by $10°$) axis between the oven and the 2D-MOT trapping region.

The analytic expression for the on-axis magnetic field at position z along the symmetry axis of two current loops with counter-propagating currents, which is the anti-Helmholtz configuration, can be calculated from the Biot-Savart law. It is

$$B_z^{\mathrm{AH}} = \frac{\mu_0 N I R^2}{2(R^2+(z-h)^2)^{3/2}} - \frac{\mu_0 N I R^2}{2(R^2+(z+h)^2)^{3/2}} \,, \tag{2.2}$$

with the number of turns per current loop N, the electrical current I and the radii R and heights $\pm h$ of the current loops. From this the first Taylor expansion around the origin $B_z^{(1)}$ can be calculated. Its first derivative,

$$\partial B_z^{(1)}/\partial z = 3\mu_0 N I \frac{R^2 h}{(R^2+h^2)^{5/2}} \,, \tag{2.3}$$

is a good estimate for the magnitude of the magnetic field gradient in the center. From this formula it can be seen that in order to achieve a high gradient, it is desirable to place the coils as near as possible to the trapped atoms. At the same time the consumed power per coil $P = I^2 R_{\mathrm{el}}$ can be reduced, with the resistance per coil $R_{\mathrm{el}} = \rho_{\mathrm{Cu}}\, l/C$, the electrical resistivity of copper at room temperature $\rho_{\mathrm{Cu}} = 1.68 \times 10^{-8}\ \Omega\,\mathrm{m}$ [143] and the length l and cross section C of the wire. This minimizes the demands upon the power supply and the water cooling system of the coils. This consideration was one of the major reasons why we decided to use re-entrant viewports in our science chamber.

The re-entrant viewport geometry allows a minimum coil height of 39 mm above and a minimum radius of 37 mm besides the atoms. These values already take a 2 mm tolerance into account. Another design criterion for the coils was that there should be enough space on the steel parts of our re-entrant flanges to place high-voltage feedthroughs in the future, which could

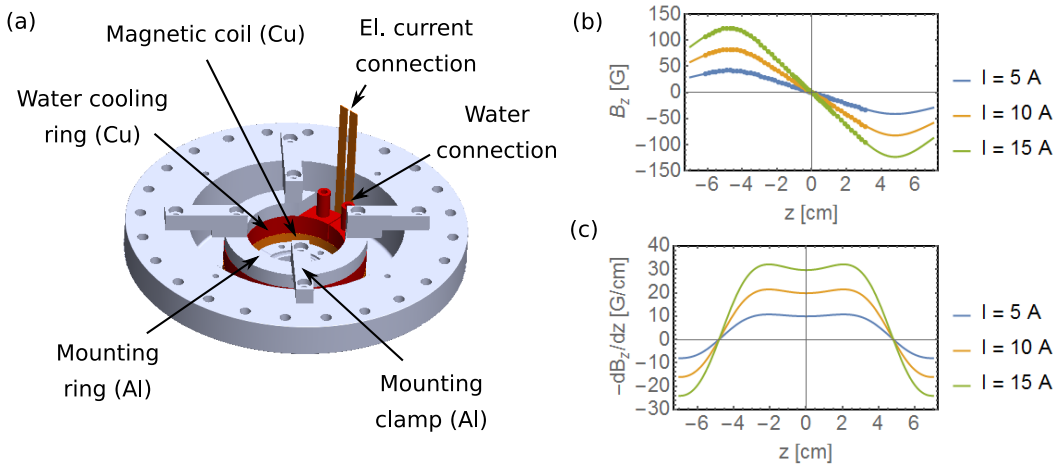

Fig. 2.7 Magnetic field generation for the 3D-MOTs. (a) An annotated drawing of the MOT coil structure in the recessed bucket of a re-entrant viewport. (b) Calculated (lines) and measured (circles) magnetic fields and (c) calculated magnetic field gradients of the anti-Helmholtz coil pair for different currents.

connect to in-vacuo electrodes and ion detectors. The outer radius of our coils was such set to 53 mm, while the inner radius of the recessed bucket is 80 mm.

The coil design is shown in Fig. 2.7 (a). We use flat 7.5×0.5 mm copper wires (MWS Wire), with 32 layers in the radial and 2 layers in the vertical direction. Each coil is cooled by a hollow copper water cooling ring which is glued (Henkel Loctite, Stycast 1266) on top of it. A similar design can be found in Ref. [144]. We chose this design over hollow copper wires with water cooling channels inside, as it needs a lower electrical current and power to achieve a given magnetic field gradient at the same geometry, due to the higher filling ratio of current-carrying wires. However, the heat contact for our coils is not very good, such that the lower re-entrant viewport gets a temperature of $\sim 30\,^{\circ}\mathrm{C}$ at an electrical current of 20 A, which corresponds to a power dissipation per coil of 32 W. This problem is certainly due to the unsufficient thermal conductivity of our used glue, and can certainly be overcome in future designs by the use of a glue with a higher thermal conductivity.

The calculated [145] and measured magnetic fields and the calculated magnetic field gradients for three different currents are shown in Fig. 2.7 (b) and (c). The axial gradient of the coil pair is 2.0 G/cm per 1 A. For our chosen geometry, the difference of gradients within a radius of 1 cm is $\simeq 2\%$. The coil circuit is powered by two in-series power supplies (Toellner, TOE 7621). It can be switched by an insulated-gate bipolar transistor. A gradient of up to 60 G/cm has been achieved with this setup.

Additionally to the anti-Helmholtz coil pair which is used for the generation of the MOT gradient fields, around the science chamber three pairs of rectangular coils in Helmholtz config-

uration are installed which allow for the compensation of the Earth's and other stray magnetic fields. They form a cage with dimensions of about $300\ \mathrm{mm} \times 500\ \mathrm{mm} \times 300\ \mathrm{mm}$, centered at the 3D MOT position. These dimensions are chosen such that they do not diminish optical access around our science chamber. Each coil has 30 windings. Formulas for the magnetic fields of rectangular coils are for example described in the thesis of A. Arnold [146]. The Helmholtz coil pairs can produce magnetic fields of a few G.

2.4 Laser system

The entire laser system described in this section, with the exception of the frequency doubler for ultraviolet light generation, is located on a separate optical table, the *laser table*, while the vacuum system in which the experiments take place is located on the *vacuum table*. The laser light is guided from the laser table to the vacuum table by polarization maintaining fibers.

The lasers used in our experiment are used to drive the electronic transitions of strontium which were introduced in the level scheme in Fig. 2.2. An overview over the four employed laser units including their frequency stabilization schemes is shown in Fig. 2.8. They are described more in detail in the following paragraphs.

(1) The blue laser system To address and cool down a large number of atoms on the blue $5\mathrm{s}^2\ {}^1\mathrm{S}_0 \rightarrow 5\mathrm{s}5\mathrm{p}\ {}^1\mathrm{P}_1$ cooling transition at 461 nm, a laser source is needed which delivers a high output power of a few 100s of mW and which is reliable. Typically employed techniques to generate high-power laser light at this wavelength are injection-locked diode lasers, whose slave laser output power can reach 100 mW in single-mode [147] or 500 mW in multi-mode operation [148], or frequency-doubled tapered amplifiers in the infrared at 922 nm [125]. In our experiment, we employ a Ti:sapphire laser at 922 nm which is frequency-doubled (MSquared, SolsTiS and ECD-X). [③] The Ti:sapphire laser is pumped by a 10 W laser at 532 nm. If no problems occur, this laser system represents a way to generate high single-mode power at 461 nm, with an output of above 500 mW.

For frequency stabilization, the Ti:sapphire laser light at 922 nm is coupled to a high-accuracy wavelength meter (High Finesse, WSU/10) via a single- or a multi-mode fiber, dependent on the experiment [150]. The output signal of the wavelength meter serves as input to a servo loop controlling the frequency of the laser. When being frequency-stabilized via the single-mode fiber, the remaining frequency fluctuations of the blue laser light are 1.1 MHz

[③] A nearby wavelength in another atomic system, for which a high power is needed, is the $4\mathrm{P}_{3/2} \rightarrow n\mathrm{S}_{1/2}/n\mathrm{D}_J$ (with $n \gg 10$) transition in potassium [149].

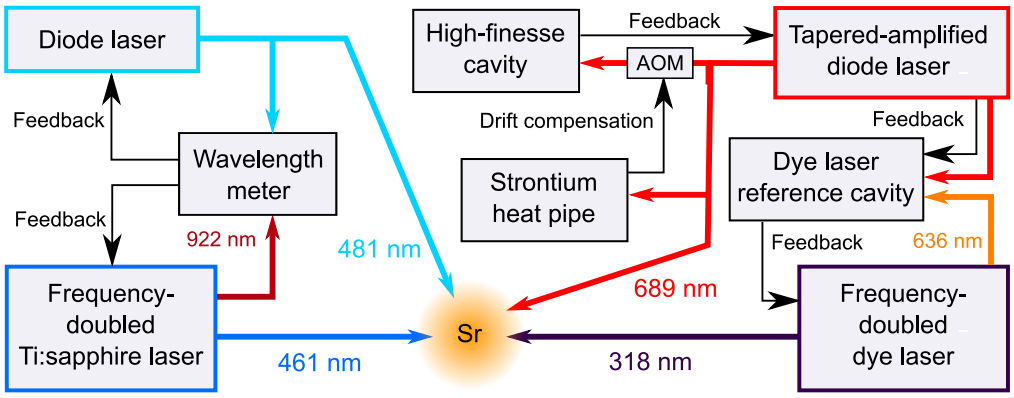

Fig. 2.8 Schematic of the laser system. Laser beams at the four wavelengths 461 nm, 481 nm, 689 nm and 318 nm are generated by four different laser units. The laser units at 461 nm and 481 nm are frequency-stabilized by a wavelength meter [150]. The laser unit at 689 nm is frequency-stabilized by a high-finesse cavity, in combination with a strontium heat pipe and a frequency-shifting acousto-optical modulator (AOM). The laser unit at 318 nm is frequency-stabilized on a reference cavity whose length is stabilized on the 689 nm laser frequency. For more details see text.

(RMS) over a time interval of 11 h, which is measured by the beat-note with a diode laser at 461 nm which is frequency-stabilized on the atomic signal in a hollow-cathode lamp [147] (not shown in Fig. 2.8). The remaining frequency fluctuations are thus much smaller than the natural linewidth of the atomic cooling transition which is 32 MHz. If the Ti:sapphire laser is stabilized by a multi-mode fiber, together with the repumping laser at 481 nm, then its RMS frequency deviation is about 2 MHz. This worse frequency stability is due to the uncertainty of the wavelength measurement of the wavelength meter which has its origin in phase shifts in the multi-mode fiber. A multi-mode fiber is however needed in this configuration, as there is no single-mode fiber available which transmits both 922 nm and 481 nm. This wavelength meter-based frequency stabilization scheme is described in greater detail by Couturier *et al.* 2018 [150].

The blue laser output is coupled to an optical path system consisting of acousto-optical modulators (AOMs), polarizing beam splitters, wave plates and fiber couplers to deliver all the needed laser frequencies and powers which are needed for atom cooling and trapping to the experiment, such as the 2D-MOT cooling beam, the Zeeman slower beam, the pushing beam, etc.

(2) The cyan laser system The 481 nm light addressing the $5s5p\,^3P_2 \rightarrow 5p^2\,^3P_2$ repumping transition is generated by a diode laser (Toptica, DL 100). Not much laser power is

needed on this transition, as a few mW are more than sufficient. [4] The laser typically delivers about 10 mW of output power after an integrated fiber dock. The laser is then split, with one beam being used for frequency-stabilization on the wavelength meter via a multi-mode fiber, and another one being fiber-coupled to be guided to the experiment. The latter beam can be turned on and off by a mechanical beam shutter [152].

(3) The red laser system To generate light addressing the narrow red $5s^2\,{}^1S_0 \rightarrow 5s5p\,{}^3P_1$ cooling transition, we employ a tapered-amplified diode laser at 689 nm (Toptica, TA pro). It typically delivers a power output of 80 mW. A high power on this level is desireable in order to be able to efficiently capture atoms from the blue MOT during the broadband phase of the red MOT [68], and to not be power-limited for two-photon excitation schemes to triplet Rydberg states. However, the tapered amplifier degrades regularly and typically has to be replaced every few months. Using the Pound-Drever-Hall technique [153, 154], it is frequency-stabilized on an ultrastable cavity with a finesse of about 200,000 (Stable Laser Systems) [155]. By measuring the cavity transmission with the frequency-stabilized laser, the laser linewidth is estimated to be on the kHz level.

The long-term drift of the ultrastable cavity is close to being linear and around 10 kHz per day, as determined by day-to-day measurements of the atomic signal in a strontium heat pipe [97, 128]. This drift can be compensated by a frequency-shifting double-pass AOM, which is placed in front of the slowly drifting high-finesse cavity, on a daily basis. All AOM drivers of the red laser system are based on direct digital synthesizers (DDSs), which have a higher frequency stability than voltage-controlled oscillators (VCOs) and which are stabilized to a rubidium atomic clock for long-term stability. The red laser beam is then split and frequency-shifted by AOMs, to produce all the beams needed for the experiment.

(4) The ultraviolet (UV) laser system Similar laser systems of other strontium Rydberg groups which address the $5s5p\,{}^3P_1 \rightarrow 5sns\,{}^3S_1/5snd\,{}^3D_J$ (with $n \gg 10$) transition at 318 nm to triplet Rydberg states are described by Refs. [156, 157]. Nearby UV wavelengths in other atomic systems are the $6\,S_{1/2} \rightarrow n\,P_J$ (with $n \gg 10$) transition in cesium at 319 nm [158, 159], the $2\,S_{1/2} \rightarrow 3\,P_{3/2}$ transition in lithium at 323 nm [160], and the magic wavelength of the metastable $1s2s\,{}^3S_1$ and $1s2s\,{}^1S_0$ states in helium at 320 nm [161]. All of these laser sources rely on frequency doubling. The fundamental is typically chosen to be the light resulting from sum frequency generation of two high-power infrared lasers [156, 157, 159, 161]. Alternative

[4] A nearby wavelength in another atomic system, for which typically a much higher power is required, is the $5P_{3/2} \rightarrow nS_{1/2}/nD_J$ (with $n \gg 10$) transition in rubidium. Here often frequency-doubled tapered amplifiers in the infrared are used [151].

sources of the fundamental are a dye laser [158] or a tapered-amplified optical diode laser [160]. We chose to use a frequency-doubled dye laser system, as it delivers a high power and as its wavelength is tunable over a wide range, such that the transitions from all three metastable states $5s5p\,{}^3P_{2,1,0}$ of strontium to near the first ionization threshold can be accessed.

The dye laser (Sirah, Matisse 2 DX) at 636 nm is pumped by a 20 W laser at 532 nm (Spectra-Physics, Millennia eV 20). If a stable frequency of the UV light is needed, then the dye laser is frequency-stabilized to a reference cavity which acts on an electro-optical modulator (EOM) and a fast piezo inside the dye cavity. As the reference cavity drifts by typically a few MHz/min without any further stabilization, its length is stabilized to the frequency of a laser beam originating from the ultrastable laser at 689 nm which is also coupled into the reference cavity, see Fig. 2.8. The feedback loop controlling the length of the reference cavity has a low bandwidth of $\sim 10\,\mathrm{Hz}$.

With this setup, the frequency change of the dye laser Δf_{dye} can be controlled by the frequency change of a double-pass AOM (not shown in Fig. 2.8) Δf_{AOM} of the 689 nm beam on which the length of the dye reference cavity is stabilized. The frequency relation is given by $\Delta f_{\mathrm{dye}} = 2\,(\lambda_{689}/\lambda_{\mathrm{dye}})\,\Delta f_{\mathrm{AOM}}$. The relation for the UV frequency change then contains another factor of two, $\Delta f_{\mathrm{UV}} = 4\,(\lambda_{689}/\lambda_{\mathrm{dye}})\,\Delta f_{\mathrm{AOM}}$.

The dye laser light at 636 nm, with a power of around 3 W, is delivered from the laser to the vacuum table by a 5 m long fiber (NKT Photonics, aeroGUIDE-Power), which is connected to SMA fiber collimators (Schäfter+Kirchhoff, 60FC-SMA-T-23-A18-02). The fiber coupling efficiency is around 50%. Even though the fiber coupling results in a significant loss of UV power, we decided to do so because of practical reasons, as the $\sim 2.5\,\mathrm{m}$ long system consisting of pump laser, dye cavity, reference cavity and frequency doubler would not conveniently fit on our vacuum table. The dye laser light is then frequency-doubled on the vacuum table (Sirah, WaveTrain 2). The UV power on the vacuum table is around 200 mW. After passing the light through an AOM (Gooch & Housego) and polarization cleaning we typically have around 80 mW available for further experiments. The linewidth of the UV laser is around 200 kHz.

Chapter 3 Two-dimensional magneto-optical trap

Part of this chapter is based on the following publication:
Ingo Nosske, Luc Couturier, Fachao Hu, Canzhu Tan, Chang Qiao, Jan Blume, Y. H. Jiang, Peng Chen, and Matthias Weidemüller. Two-dimensional magneto-optical trap as a source for cold strontium atoms. *Phys. Rev. A* 96, 053415 (2017).

In this chapter the characterization of a strontium 2D-MOT is described, which represents a compact alternative cold atom source minimizing vacuum contamination and black-body radiation at the experiment region, compared to a Zeeman slower. Deflected ^{88}Sr cold atomic fluxes of 4×10^9 s^{-1} are achieved. The longitudinal velocity of the cold atomic beam emerging from the 2D-MOT is found to be tunable over several tens of m/s by the pushing beam intensity, between about 20 m/s and 50 m/s, and it has a typical divergence of around 60 mrad.

In the following, first general techniques for the realization of cold atom sources are introduced in Sec. 3.1. Then our experimental setup and the employed fluorescence diagnostics are described in Sec. 3.2. A description of the characterization of the cold atomic beam follows in Sec. 3.3. This chapter is then concluded by a discussion on future designs for strontium 2D-MOTs to gain higher atomic fluxes in Sec. 3.4.

3.1 Cold atom sources

One straightforward way to generate cold atoms is to simply create a MOT which captures atoms from a background gas, called a vapor-cell MOT (VCMOT) [67, 162]. VCMOTs were realized for strontium atoms, however, due to its low vapor pressure, in order to generate a sufficiently dense background gas of strontium atoms, the MOT chamber has to be heated to temperatures on the order of 300 °C [103, 106]. This high temperature is a technical nuisance due to the higher probabiliy of an arising leak of the vacuum system and due to more generated heat around the science chamber, which for example can lead to the distortion of laser beam paths. Additionally, VCMOTs have the disadvantage that a relatively dense background gas is present at all times and creates large atomic loss rates due to collisions.

Therefore MOTs in state-of-the-art cold atom experiments are typically loaded by slow atomic beams – that means cold atomic beams –, which are generated in a second vacuum chamber separated from the MOT chamber by a differential pumping tube. The two most com-

mon ways to produce a cold atomic beam are the implementation of a Zeeman slower, in which hot atoms emanating from an oven or a dispenser are slowed down by a counter-propagating beam in a spatially varying magnetic field [7, 104], or of a 2D-MOT, in which atoms are laser-cooled along two dimensions and then accelerated by a pushing beam along the third dimension towards the MOT [11, 163]. Another early realized source of a cold atomic beam is the low-velocity intense source (LVIS), in which atoms are pushed out of a VCMOT by the cooling power imbalance created by a hole in one of the six cooling beams [164].

For cold strontium experiments, typically a Zeeman slower is employed. Its magnetic field can be either generated by magnetic coils [12, 68, 104] or by permanent magnets [165–168]. The Zeeman slower design is often combined with a collimation of the oven beam through heated microtubes [169, 170] and a transverse optical molasses cooling stage. All cooling lasers from the optical molasses to the first MOT typically address the broad closed $^1\mathrm{S}_0 \rightarrow {}^1\mathrm{P}_1$ transition at 461 nm. [①] Typical ^{88}Sr MOT loading rates of Zeeman slowers are on the order of $10^9\,\mathrm{s}^{-1}$ [68], while one reference reports loading rates of up to $4 \times 10^{10}\,\mathrm{s}^{-1}$ [104].

The standard Zeeman slower design exhibits a direct line of sight from the heated oven to the MOT, which results in a constant background atomic flux and in an increased exposure to black-body radiation at the MOT position. It is well-known that black-body radiation is a major source of uncertainty in strontium optical lattice clocks [83, 172], due to which in clock setups hot surfaces are preferred to be isolated from the experiment position. To avoid these problems, an in-vacuo atomic beam shutter between the oven and the MOT can be used. Another approach was realized in Refs. [12, 173] and consists of a 2D-MOT after a standard Zeeman slower which brightens and deflects the cold atomic beam.

Apart from the avoidance of vacuum contamination and black-body radiation at the experiment region, the 2D-MOT design, if applicable, is usually preferred over the Zeeman slower design, due to its more compact size and the unnecessity of a dedicated design of the magnetic field configuration or an undertaking of the effort in engineering the coil structure. A large variety of vapor-cell 2D-MOT designs have been reported in the literature, for example for the elements rubidium [11, 174, 175], cesium [163, 176, 177], potassium [178] and mercury [179, 180]. This is possible due to the relatively high vapor pressures of these elements around room temperature.

However, for elements with lower vapor pressures, such as the alkaline-earth atoms, the

[①] This is contrary to e.g. the alkaline-earth-like atom ytterbium. For this element the initial cooling of thermal atoms address the broad $^1\mathrm{S}_0 \rightarrow {}^1\mathrm{P}_1$ transition, while the MOT typically directly addresses the narrow intercombination $^1\mathrm{S}_0 \rightarrow {}^3\mathrm{P}_1$ transition [171]. That is possible as this intercombination transition in ytterbium is around 25-times broader than in strontium, which results in higher achievable decelerations in a light field and in higher MOT capture velocities.

vapor-cell 2D-MOT design can hardly be realized. An alternative is offered by the transversely loaded 2D-MOT design [118, 120, 171]. Unlike the vapor-cell 2D-MOT, which is isotropically loaded from a uniform background vapor, the transversely loaded 2D-MOT captures an atomic beam effusing from a high-temperature oven or a dispenser. Transversely loaded 2D-MOTs were successfully demonstrated for the two alkali atoms lithium [118] and sodium [120, 181], which both have low vapor pressures. They have a compact design, with a small distance between the oven and the trapping region on the order of 10 cm, and are equipped with permanent magnets for producing the required two-dimensional quadrupolar magnetic field. A similar design was realized for the alkaline-earth-like atom ytterbium [171].

Following up on the seminal work of Tiecke *et al.* 2009 [118], we realized a compact, transversely loaded 2D-MOT source for cold strontium atoms. By implementing the design of Lamporesi *et al.* 2013 [120], the cold atomic flux can be increased if an auxiliary Zeeman slower beam is added, counter-propagating to the hot oven beam. Our realized source of cold strontium atoms is similar to the one described in Ref. [182], which is employed to load a trapped-ion array, and to a system which includes a Zeeman slower and two 2D-MOTs for strontium which is offered by the company AOSense, Inc. (see the Supplementary Materials of Ref. [183]). [②] Another early setup of a strontium 2D-MOT is described in Ref. [186], however only low MOT loading rates were achieved in that setup.

3.2 Setup and diagnostics

The setup of our strontium 2D-MOT is described in Sec. 3.2.1, and the diagnostics methods are introduced in Sec. 3.2.2.

3.2.1. 2D-MOT setup

The schematic of the strontium 2D-MOT is shown in Fig. 3.1 (left and center). The aperture of the oven, in which 5 g of strontium with natural isotope abundance (99.99 % purity; Sigma & Aldrich) are deposited, is located 125 mm below the center of a custom-made multiway cross vacuum chamber, which is the 2D-MOT trapping region. The oven is typically operated at a temperature of 465 °C and does not have a heated microtube array for atomic beam collimation in its aperture [104, 169, 170]. To avoid strontium coating of the opposite viewport for the auxiliary Zeeman slower, the window is permanently heated to 330 °C. A differential pumping tube separates the 2D-MOT chamber from a subsequent UHV chamber. Its entry has no direct

[②] Visualizations of the source from AOSense can be seen in theses from the group of Jun Ye, i.e. in Figure 6.1 of Ref. [184] and in Figure 3.1 of Ref. [185].

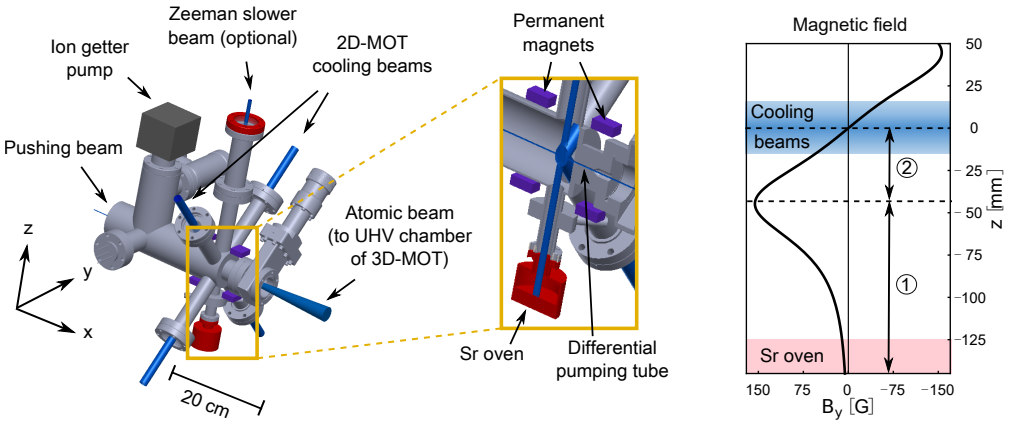

Fig. 3.1 Schematic of the 2D-MOT. Left: Experimental setup. Hot strontium atoms effusing from the oven in the bottom of the setup are cooled and trapped in the center of the multiway cross vacuum chamber by a perpendicular pair of retro-reflected cooling beams. Atoms in the 2D-MOT are pushed to a UHV chamber (not shown) where they can be further loaded into a 3D-MOT. A Zeeman slower beam (optional) is used to decelerate hot strontium atoms through the top viewport of the setup. Heated parts of the setup are highlighted in red. The vacuum of the setup is maintained by an ion getter pump. Center: Zoom-in of the highlighted rectangle in the left part. Four stacks of permanent magnets are used to generate the 2D quadrupolar magnetic field. A differential pumping tube is located between the 2D-MOT vacuum chamber and the UHV chamber for vacuum isolation. Right: Magnetic field along the z direction. The red shaded area depicts the strontium oven, while the blue shaded area represents the 2D-MOT cooling beams. For Zeeman deceleration, either region ① or ② can be used.

line of sight to the oven, and no clogging of the tube is noticed by observation through the pushing beam viewport. The pressure in the 2D-MOT chamber is $\sim 2 \times 10^{-10}$ mbar. For more details on the vacuum system see Sec. 2.2.

Hot strontium atoms evaporated from the oven are cooled and trapped in the 2D-MOT by a perpendicular pair of retro-reflected circularly polarized cooling beams, with $1/e^2$ radii of 7.5 mm, in the $\sigma^+ - \sigma^-$ configuration. Four stacks of permanent magnets create a two-dimensional quadrupolar magnetic field with a gradient of 34 G/cm along the cooling beam axes, as well as a transverse B_y field component along the z axis which coincides with the propagation direction of the hot atomic beam (for more details on the permanent magnet setup see Sec. 2.3.1). There are two regions of the magnetic field topology which allow for Zeeman slowing, as labeled ① and ② in Fig. 3.1 (right). This magnetic field design enables one to increase the 2D-MOT loading rate by implementing an auxiliary Zeeman slower beam, with a $1/e^2$ radius of 6 mm, through the viewport opposite to the strontium oven [120]. The captured atoms are then accelerated along the x direction by a pushing beam with $1/e^2$ radius 0.7 mm.

Two possible realizations of the four 2D-MOT cooling beams are shown in Fig. 3.2. They

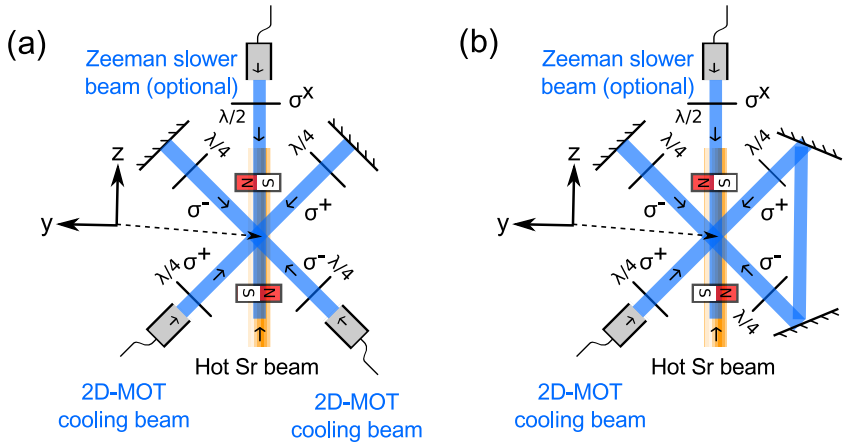

Fig. 3.2 Optical setup for the 2D-MOT cooling and the Zeeman slower beams. (a) Two retro-reflected beams or (b) a single recycled beam can be used for the realization of the four 2D-MOT cooling beams. While the cooling beam paths contain quarter-wave plates ($\lambda/4$) for the realization of the $\sigma^+ - \sigma^-$ configuration, in front of the Zeeman slower beam a half-wave plate ($\lambda/2$) is installed, which maximizes the effective beam power in a transverse Zeeman slower.

can either be formed by two retro-reflecting laser beams, see Fig. 3.2 (a), or by a single laser beam which is guided through the vacuum chamber for four times, see Fig. 3.2 (b). The latter realization – a single recycled 2D-MOT cooling beam – can be used for achieving about the same flux of the cold atomic beam from the 2D-MOT, if compared to the two retro-reflected 2D-MOT cooling beams. The optimum flux is achieved for a slight misalignment of the cooling beams with respect to the center lines of the vacuum chamber, which is certainly due to an emerging power imbalance of the cooling beams in that configuration which has to be compensated for in order not to misalign the position of the cold atoms in the 2D-MOT. This setup requires a more complicated alignment procedure but is advisable when the available blue laser power is scarce.

A half-wave plate is installed in front of the Zeeman slower beam, see Fig. 3.2, as a Zeeman slower beam with a linear polarization which is orthogonal to the magnetic field direction maximizes the fraction of beam power which can be used for slowing down atoms in a transverse Zeeman slower [166]. The maximum usable power for slowing in a transverse Zeeman slower, however, is only $50\,\%$ [187]. In our case, as the magnetic field points along the y direction, the optimum linear polarization of the Zeeman slower beam points along the x direction. It is confirmed in the experiment that the flux increase due to the Zeeman slower beam can be tuned nearly to zero by rotating this half-wave plate. All Zeeman slower optics after the fiber coupler, which also include a polarizing beam splitter, a photodiode for power monitoring and an additional mirror for aligning purposes (not shown in Fig. 3.2), are directly attached to

the thermal insulation structure of the heated Zeeman slower viewport (for its design see the Appendix A.2).

The pushing beam collimator and a 50:50 beam splitter are held by mirror mounts which are directly attached to the vacuum system and allow for beam alignment. The beam splitter allows for visual inspection of the blue fluorescence of the 2D-MOT and the hot oven beam, which is clearly visible by eye, when the pushing beam is off.

3.2.2. Diagnostics

The fluorescence light of the cold atomic beam, which originates from the 2D-MOT, is collected by a 1-inch lens with a focal length of $25\ \mathrm{mm}$, which is located at a distance of $90\ \mathrm{mm}$ from the atoms at a CF40 viewport. [3] The fluorescence light then passes a narrowband filter for 461 nm (Semrock, FF01-461/5-25) and hits a photodiode (Thorlabs, SM05PD1A) with a responsitivity of $\mathcal{R} = 0.14(1)\,\mathrm{A/W}$ at 461 nm and an active area of $3.6\ \mathrm{mm} \times 3.6\ \mathrm{mm}$. The photodiode current is fed into a current preamplifier (Stanford Research Systems, SR570) whose output is read out on an oscilloscope.

The atom number N_{at} can be related to the oscilloscope voltage U_{PD} by $N_{\mathrm{at}} = C_{\mathrm{PD}} \times U_{\mathrm{PD}}$, with the conversion factor

$$C_{\mathrm{PD}} = (\Gamma_{\mathrm{sc}} \times \hbar\omega \times L\,\Omega_{\mathrm{PD}}\,F_{\mathrm{dip}} \times \mathcal{R}\,G)^{-1}\,, \tag{3.1}$$

which has the unit $[V^{-1}]$. Hereby are the scattering rate Γ_{sc}, the angular frequency of the atomic transition ω, the optics loss factor L, the solid angle $\Omega_{\mathrm{PD}} = r^2/4d^2$ with the lens radius r and distance d, the enhancement factor due to the dipole radiation pattern F_{dip} and the gain G. The scattering rate in a two-level system is given by [188]

$$\Gamma_{\mathrm{sc}} = \frac{\Gamma}{2}\frac{I/I_{\mathrm{sat}}}{1 + I/I_{\mathrm{sat}} + 4\Delta^2/\Gamma^2}\,, \tag{3.2}$$

with the natural linewidth $\Gamma/2\pi = 32\,\mathrm{MHz}$ and the saturation intensity $I_{\mathrm{sat}} = 43\,\mathrm{mW/cm^2}$ of the blue transition (see Table 2.2), the excitation beam intensity I and the excitation beam detuning to the atomic transition Δ. The combined average intensity of two beams is taken, $I = 2 \times P/(\pi\,w^2)$, with the beam power P and the $1/e^2$ beam radius w.

We found that the fluorescence signal of the atomic beam depends on the angle between the detection direction and the linear polarization direction of the excitation beam, see Fig. 3.3. Indeed the expected angular emission pattern for π-scattered light in a pure two-level system, as it is the case for our transition, is non-isotropic, as it follows the classical radiation pattern for

[3] The atomic beam measurements were done in a test setup, with the 2D-MOT chamber being connected to a CF40 six-way cross instead of the UHV chamber which hosts the 3D-MOT.

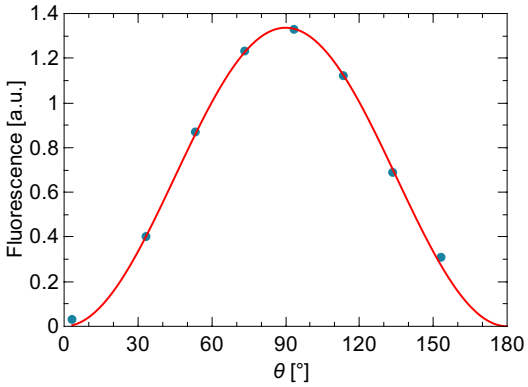

Fig. 3.3 Angular dependence of the atomic beam fluorescence. Plotted are the measured fluorescence over the angle θ between the detection direction and the linear polarization direction of the excitation beam (blue circles). The red line is a theoretical fit according to Eq. (3.3) which describes the angular dependence of π-scattered light in a pure two-level system.

an oscillating dipole. The normalized expression of its theoretical angular dependence is given by [105, 189, 190]

$$f(\theta, \phi) = \frac{3}{8\pi} \sin^2 \theta \,, \tag{3.3}$$

with θ being the angle between the photon emission direction and the linear polarization direction of the excitation beam. While there is a strong dependence on the polar angle $\theta \in [0, \pi]$, there is no dependence on the azimuthal angle $\phi \in [0, 2\,\pi]$ in the plane which is normal to the linear polarization direction of the excitation beam. Eq. (3.3) was fitted to the experimental data and a good agreement was found, see Fig. 3.3.

We then calculate the enhancement factor due to the dipole radiation pattern F_{dip} as being the ratio of (i) the angular dependence function of the fluorescence $f(\theta, \phi)$, which is integrated up to the capture half-angle of the imaging system $\alpha_c = \tan^{-1}(r/d)$ around $\theta = \pi/2$ where the fluorescence signal is maximized, and (ii) the solid angle neglecting any angular dependence of the spontaneous emission $r^2/4d^2$:

$$F_{\mathrm{dip}} = \int_{\pi/2-\alpha_c}^{\pi/2+\alpha_c} \mathrm{d}\theta \, \sin\theta \int_{-\alpha_c}^{\alpha_c} \mathrm{d}\phi \, \frac{f(\theta, \phi)}{r^2/4d^2} \,. \tag{3.4}$$

This factor is 1.87 in our case. In the case of the 3D-MOT, due to averaging over many polarizations and angles, this factor is set to unity which corresponds to isotropic fluorescence emission. Typical values for the photodiode setup are summarized in Table 3.1.

Additionally to the photodiode setup the fluorescence of the atomic beam is also measured by a complementary metal-oxide semiconductor (CMOS) camera.

Quantity	**Value**
Excitation beam power P	2x 6 mW
Excitation beam $1/e^2$ radius w	2.4 mm
Excitation beam detuning $\Delta/2\pi$	zero
Scattering rate Γ_{sc}	$6.1 \times 10^7\ \mathrm{s}^{-1}$
Optics loss factor L	0.88
Solid angle Ω_{PD}	5.0×10^{-3}
Dip. rad. enhancement factor F_{dip}	1.87
Gain G	$5 \times 10^9\ \mathrm{V/A}$
Conversion factor C_{PD}	$6.6 \times 10^3\ \mathrm{atoms/V}$
10% to 90% rise time	3.6 ms

Table 3.1 Typical values of the photodiode setup for the flux determination of the 2D-MOT cold atomic beam.

3.3 Characterization of the cold atomic beam

We then measure the properties of the cold atomic beam emanating from the 2D-MOT. The properties of the cold atomic beam are of interest as they will determine the loading efficiency of the downstream 3D-MOT.

First the atomic beam emanating from the 2D-MOT, being accelerated by the pushing beam, is measured by the time-of-flight (TOF) method [11]. A retro-reflected laser beam on resonance with the broad closed transition of strontium is applied to excite the cold atomic beam emerging from the 2D-MOT. The linearly polarized excitation beam with $1/e^2$ diameter $d_{\mathrm{exc}} = 4.8\,\mathrm{mm}$ propagates along the z direction at a distance of $\ell = 300\,\mathrm{mm}$ downstream from the center of the 2D-MOT. The atomic fluorescence during the excitation is collected with a photodiode and additionally monitored by a CMOS camera.

The temporal evolution of the fluorescence signal is measured after suddenly turning off the pushing laser beam by an AOM, from which we can deduce the longitudinal velocity distribution of the atomic beam and the atomic flux. The atomic flux per longitudinal velocity is given by

$$\Phi(v_x) = \frac{C_{\mathrm{PD}}}{d_{\mathrm{exc}}} \frac{\ell}{v_x} \frac{1}{g(\theta_{\mathrm{FWHM}})} \left(-\frac{\mathrm{d}U_{\mathrm{PD}}(t)}{\mathrm{d}t} \right), \tag{3.5}$$

with the conversion factor of voltage to atom number C_{PD} from Eq. (3.1), the longitudinal velocity v_x, a divergence θ_{FWHM}-dependent factor $g(\theta_{\mathrm{FWHM}})$ which describes the overlap of the excitation laser beam intensity with the atomic beam density, and the voltage signal measured from the fluorescence $U_{\mathrm{PD}}(t)$. A detailed derivation of Eq. (3.5) can be found in the Appendix B.1.

Measurement results for different parameters of the cold ^{88}Sr atomic beam versus the push-

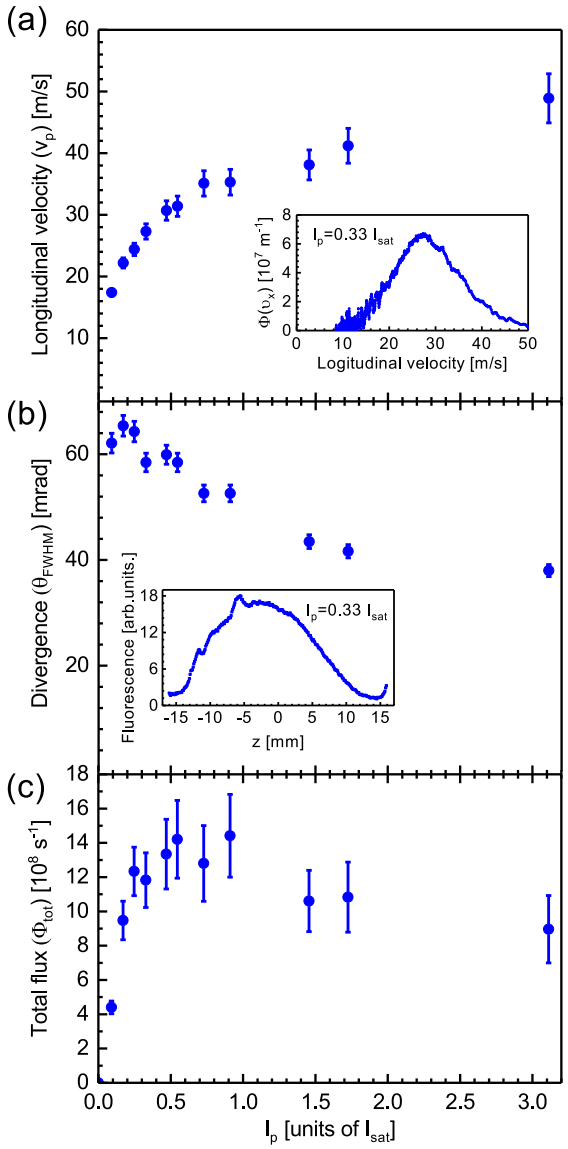

Fig. 3.4 Characterization of the cold atomic beam. (a) The most probable longitudinal velocity, (b) the divergence, and (c) the total flux of the atomic beam versus the pushing beam light intensity. The insets in (a) and (b) show the longitudinal velocity distribution and the transverse distribution of the atomic beam at $I_\mathrm{p} = 0.33\, I_\mathrm{sat}$

ing beam peak intensity I_p are shown in Fig. 3.4. For this measurement the power per 2D-MOT cooling beam is set to 30 mW, its detuning is -50 MHz and the pushing beam detuning is set to zero. Apart from these values, the magnetic field gradient is set to $50\ \mathrm{G/cm}$, the oven temperature is $465\ ^\circ\mathrm{C}$, and Zeeman slower loading was applied which enhanced the flux by a factor of 3 (see Sec. 4.2.3). The measured most probable longitudinal velocity v_p is shown in Fig. 3.4 (a), which is the velocity at which the atomic flux per longitudinal velocity $\Phi(v_x)$ has its maximum. One example for $\Phi(v_x)$ is shown in the inset. The most probable longitudinal velocity varies from 17 m/s to 49 m/s with increasing I_p, and appears to increase at a smaller rate beyond I_sat.

The full-width-at-half-maximum (FWHM) divergence θ_FWHM of the atomic beam is mea-

sured by fluorescence imaging using the CMOS camera for different pushing beam intensities, which gives us the transverse density distribution of the atomic beam. The result is shown in Fig. 3.4 (b), and an example of the transverse density distribution for $I_p = 0.33\, I_{\mathrm{sat}}$ is shown in the inset. It can be seen that θ_{FWHM} is around $60\,\mathrm{mrad}$ for small I_p and then decreases to $40\,\mathrm{mrad}$ for large I_p. Generally a small beam divergence is desired in order to hit the trapping region of the 3D-MOT. This trend can be understood by two effects: For small I_p, the divergence of the atomic beam is limited to around $60\,\mathrm{mrad}$ by clipping at the differential pumping tube of the vacuum system (with diameter $2.0\,\mathrm{mm}$ and length $22.8\,\mathrm{mm}$, starting $14\,\mathrm{mm}$ downstream from the 2D-MOT center). The transverse density distribution of the atomic beam looks more box-shaped for small I_p and more Gaussian-shaped for large I_p, which supports this theory as the wings of the initially Gaussian-shaped beam are cut off by the differential pumping tube. For large I_p, the divergence of the atomic beam is governed by the ratio of the transverse and longitudinal velocities. Indeed it is found that in this regime the divergence is proportional to the inverse most probable longitudinal velocity, $\propto v_p^{-1}$. It such follows the trend of the travelling time of the atoms, while the radial velocities are assumed to not change significantly for different I_p.

From the divergence at large I_p we can get an estimate on the transverse temperature in the 2D-MOT. The cooling beam detuning Δ-dependent minimum achievable temperature due to fluctuations in the cooling force is given by [188]

$$T_\Delta = \frac{\hbar\,\Gamma}{4\,k_B}\,\frac{1+(2\Delta/\Gamma)^2}{-2\Delta/\Gamma}\,. \tag{3.6}$$

This temperature is simply the Doppler temperature $T_D = \hbar\,\Gamma/2k_B = 770\ \mu\mathrm{K}$ at $\Delta = -\Gamma/2$. T_Δ is 1.4 mK for our cooling beam detuning and corresponds to a one-dimensional radial RMS velocity of $v_{r,\Delta} = (k_B T_\Delta/m)^{1/2} = 35\,\mathrm{cm/s}$. Additionally, there is a radial heating of the cold atoms by the pushing beam acceleration, due to the random nature of the spontaneous emission. It contributes an additional Gaussian broadening with the RMS velocity $v_{r,p} = \frac{1}{\sqrt{3}} v_R \sqrt{N}$ [189, 191]. Hereby were used the recoil velocity of the blue transition $v_R = \hbar k/m = 9.8\,\mathrm{mm/s}$ and the number of absorbed pushing beam photons $N \simeq v_p/v_R$. At our largest measured most probable longitudinal velocity v_p this results in $v_{r,p} = 40\,\mathrm{cm/s}$. A convolution of the two Gaussian distributions, which are approximated to be independent from each other, results in the combined radial velocity of $v_{r,\mathrm{tot}} = (v_{r,\Delta}^2 + v_{r,p}^2)^{1/2} = 53\,\mathrm{cm/s}$. With this we can approximate the divergence of the cold atomic beam as

$$\theta_{\mathrm{FWHM}} \simeq C_{\mathrm{GF}}\,\frac{v_{r,\mathrm{tot}}}{v_p}\,, \tag{3.7}$$

which is $26\,\mathrm{mrad}$ in this case. The prefactor $C_{\mathrm{GF}} = 2\sqrt{2\ln 2} \approx 2.355$ accounts for the conversion from the standard deviation to the full-width-at-half-maximum of a Gaussian distribution.

The measured value is around 50% above the theoretical one [see the highest intensity data point in Fig. 3.4 (b)]. This is likely due to a higher transverse temperature in the 2D-MOT. The measured divergences at high I_p fit well with a 2D-MOT temperature of $5\,\mathrm{mK}$, which is a reasonable value.

With the results from the measurements of the atomic flux per longitudinal velocity the atomic flux can be determined by integration over velocity:

$$\Phi_{\mathrm{tot}} = \int_0^\infty \mathrm{d}v_x \, \Phi(v_x) \, . \tag{3.8}$$

It is shown as a function of the pushing beam intensity in Fig. 3.4 (c). The flux rises to $1.4 \times 10^9\,\mathrm{s}^{-1}$ with increasing I_p, and decreases to about $1.0 \times 10^9\,\mathrm{s}^{-1}$ beyond saturation intensity. The rise of Φ_{tot} for small I_p is correlated with the increase of v_p, resulting in a better beam collimation and an avoided clipping at the differential pumping tube. However, although v_p still increases with a larger I_p, the total atomic flux no longer continues to rise but instead decreases slightly. A possible reason is that the cooling process of the 2D-MOT is perturbed by the force exerted by the pushing beam. The optimum flux of $1.4 \times 10^9\ \mathrm{s}^{-1}$ is achieved around the saturation intensity of the pushing beam light intensity. Without additional Zeeman slowing it is about $4 \times 10^8\ \mathrm{s}^{-1}$.

Its order of magnitude agrees well with the theoretical order of magnitude of the 2D-MOT loading rate for the ^{88}Sr isotope, which can be calculated by the formula

$$L_{\mathrm{2D}}^{88} = a_{88} \frac{1}{4} \, n_a \, \bar{v} \, A_{\mathrm{oven}} \times \left(\frac{w_{\mathrm{cool}}}{d_{\mathrm{oven}}} \right)^2 \times \frac{1}{2} \left(\frac{v_{c,\mathrm{2D}}}{v_{\mathrm{mp}}} \right)^4 , \tag{3.9}$$

with the isotope abundance $a_88 = 82.58\,\%$ [98], the atomic density in the oven n_a, the most probable speed $v_{\mathrm{mp}} = \sqrt{2k_BT/m}$ and the mean thermal speed $\bar{v} = \sqrt{4/\pi}\, v_{\mathrm{mp}}$ of an atom, the oven aperture area A_{oven}, the 2D-MOT cooling beam $1/e^2$ radius w_{cool}, the distance from the oven bottom to the 2D-MOT d_{oven}, and the capture velocity of the 2D-MOT $v_{c,\mathrm{2D}}$. For our parameters the 2D-MOT loading rate is calculated to be $2.0 \times 10^8\ \mathrm{s}^{-1}$ without additional Zeeman slowing, however there are considerable uncertainties in the 2D-MOT capture velocity and the saturated vapor pressure of strontium. The derivation of Eq. (3.9) and the parameters in our system are given in the Appendix B.2.

3.4 Prospects for future designs

In our setup, without an additional Zeeman slower applied and $40\,\mathrm{mW}$ of power available in the single recycled 2D-MOT cooling beam configuration [see Fig. 3.2 (b)], a ^{88}Sr cold atomic flux of $4 \times 10^8\ \mathrm{s}^{-1}$ can be achieved at an oven temperature of $465\ ^\circ\mathrm{C}$. Together with the Zeeman

slower beam and at an oven temperature of $500\ ^{\circ}\mathrm{C}$, this flux can be increased by one order of magnitude to $4 \times 10^{9}\ \mathrm{s}^{-1}$, without any sign of saturation versus the oven temperature. The strontium 2D-MOT design can certainly be optimized in a few ways in future setups, in order to increase the atomic flux. Some of the possibilities are:

- The adding of heated microtubes in the oven aperture could increase the atomic beam collimation and such the fraction of the incident flux on the 2D-MOT trapping region and the total flux from the oven [104, 169, 170]. A minor downside of this technique is that the oven has to be operated at slightly higher temperatures which results in faster atoms and a lower 2D-MOT loading rate, see Eq. (3.9). However, the positive effect of microtubes is certainly much higher, as it can increase the incident fraction of atoms from the current value of $\simeq 0.3\%$ (for the calculation see the Appendix B.2) to a much higher value.

- In case there is no beam collimation due to microtubes, a decrease of the distance between the oven and the 2D-MOT trapping region d_{oven} is expected to also lead to an increase of the incident flux, which scales as $\propto d_{\mathrm{oven}}^{-2}$, see Eq. (3.9). In that case heat insulation from the oven becomes more challenging.

- Another idea is to simply put more strontium chunks inside the oven and to operate the oven at a higher temperature, to have a correspondingly higher oven flux at the same oven lifetime. In this case it would be insightful to measure the oven temperature at which the 2D-MOT loading rate peaks, which can for example be due to atom loss mechanisms by collisions at the oven orifice or in the 2D-MOT trapping region [118].

- The Zeeman slower design can certainly be improved, for example by adding more magnet stacks in order to optimize the fringe magnetic field of the 2D-MOT for the Zeeman slowing process. For measurements of the flux enhancement due to the auxiliary Zeeman slower beam see Sec. 4.2.3.

- To increase the 2D-MOT loading rate, its cooling beam sizes could be increased. In this case, however, it has to be made sure that there is still a direct line of sight from the oven aperture to the 2D-MOT cooling beam such that the hot oven beam is not clipped. This could for example be achieved by a slightly vee-shaped tube between the oven and the 2D-MOT trapping area.

Chapter 4 Three-dimensional magneto-optical traps

Part of this chapter is based on the following publication:
Ingo Nosske, Luc Couturier, Fachao Hu, Canzhu Tan, Chang Qiao, Jan Blume, Y. H. Jiang, Peng Chen, and Matthias Weidemüller. Two-dimensional magneto-optical trap as a source for cold strontium atoms. *Phys. Rev. A* 96, 053415 (2017).

In this chapter, the laser cooling procedure of strontium atoms from the cold atomic beam of the 2D-MOT to a magneto-optically trapped cloud of ultracold atoms with temperatures in the low μK regime and with atomic densities of $> 10^{10}\ \mathrm{cm}^{-3}$ is described. ^{88}Sr loading rates into the blue MOT exceeding $10^9\ \mathrm{s}^{-1}$ are achieved. Our laser cooling procedure includes two subsequent 3D-MOTs [67] operating on the broad closed transition at 461 nm and on the narrow closed transition at 689 nm of strontium. As it is usual in the literature about laser cooling of strontium atoms, these two types of MOTs are called *blue MOT* and *red MOT*, named after the colors of their transition wavelengths.

First the blue MOT for strontium atoms in our setup will be described in detail, i.e. its setup and diagnostic techniques in Sec. 4.1, and the achieved atom numbers and the dependencies of the loading rate on various parameters in Sec. 4.2. This description is followed by an investigation of the enhancement of the blue MOT atom number if the repumping laser at 481 nm is applied in Sec. 4.3, and by an investigation of the performance of our magnetic trap acting on atoms in the $5s5p\ ^3P_2$ metastable state which result from a loss mechanism in the MOT cooling cycle in Sec. 4.4. In the end of this chapter the loading and operation of our red MOT is described in Sec. 4.5.

4.1 Setup and diagnostics

The setup is shown in Sec. 4.1.1, and diagnostics methods are described in Sec. 4.1.2.

4.1.1. 3D-MOT setup

The blue and the red MOTs are formed in the center of our science chamber. The atoms are trapped by the interplay of the magnetic field gradient, which is generated by a pair of anti-Helmholtz coils, and by three circularly polarized orthogonal pairs of counter-propagating cooling beams for each MOT, see Fig. 4.1 (a). The cooling beams are red-detuned to the respective

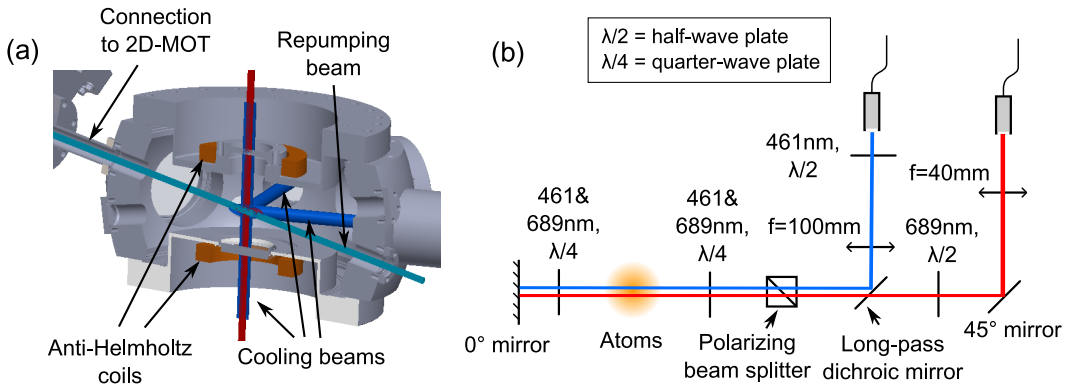

Fig. 4.1 Setup of the blue and red 3D-MOTs. (a) A visualization of the science chamber, the MOT laser beams, the repumping beam and the anti-Helmholtz coils. (b) The optical setup for each of the three blue and red cooling beam pairs.

atomic transitions. The blue cooling beams at 461 nm address the ${}^1\mathrm{S}_0 \rightarrow {}^1\mathrm{P}_1$ transition and have $1/e^2$ radii of $6\ \mathrm{mm}$, and the red cooling beams at 689 nm address the ${}^1\mathrm{S}_0 \rightarrow {}^3\mathrm{P}_1$ transition and have radii of $3.5\ \mathrm{mm}$. The blue and the red cooling beams are both split into three on the laser table and coupled into polarization maintaining fibers to the vacuum table, where they are overlapped on dichroic mirrors. For a visualization of the optical layout for one MOT axis on the vacuum table see Fig. 4.1 (b). The 2D-MOT cold atomic beam hits the blue MOT at angles of $10°$ towards the horizontal plane and of $18.5°$ towards the nearest 3D-MOT cooling beam axis in the horizontal plane. From this tilted geometry it follows that the largest fraction of the slowing process of the cold atomic beam is due to the blue cooling beam which is roughly counter-propagating to the slow atomic beam.

A repumping beam at 481 nm addresses the transition from the metastable $5\mathrm{s}5\mathrm{p}\,{}^3\mathrm{P}_2$ state to the doubly-excited $5\mathrm{p}^2\,{}^3\mathrm{P}_2$ state. It has a $1/e^2$ radius of $2.5\ \mathrm{mm}$ and is shined on the atoms through the viewport which is opposite to the 2D-MOT, see Fig. 4.1 (a). Atoms can accumulate in the metastable state due to the $5\mathrm{s}5\mathrm{p}\,{}^1\mathrm{P}_1 \rightarrow 5\mathrm{s}4\mathrm{d}\,{}^1\mathrm{D}_2 \rightarrow 5\mathrm{s}5\mathrm{p}\,{}^3\mathrm{P}_2$ decay which has a probability of $\approx$ 1:150,000 if compared to the decay of the cooling transition. For more information on the cooling and the repumping transitions refer to Sec. 2.1.2. The level scheme relevant for laser cooling of strontium atoms is shown in Fig. 2.2.

4.1.2. Diagnostics

The blue MOT is diagnosed by collecting its fluorescence light on a photodiode, which delivers information about the temporal behavior of the MOT atom number, and by performing absorption imaging on a camera, which gives information about the spatial size of the MOT. Exclusively absorption imaging is performed to analyze the red MOT behavior, as due to the low scattering rate on the red transition the MOT fluorescence is weak.

The conversion factor from voltage to atom number C_{PD} of the photodiode which is used for fluorescence light collection from the MOT can be calculated in the same way like it was done for the photodiode setup which was used for the atomic flux determination from the 2D-MOT, Eq. (3.1), as was described in Sec. 3.2.2. Typical values for the 3D-MOT fluorescence collecting photodiode which enter this formula are excitation beam power $P = 7\ \mathrm{mW}$ (power of a single out of six beams), excitation beam $1/e^2$ radius $w = 6\ \mathrm{mm}$, beam intensity $I = 6 \times 2P/(\pi w_{\mathrm{3D}}^2)$ (combined peak intensity of six beams) and excitation beam detuning $\Delta/2\pi = -30\ \mathrm{MHz}$ which according to Eq. (3.2) results in the scattering rate $\Gamma_{\mathrm{sc}} = 2.8 \times 10^7\ \mathrm{s}^{-1}$; and the optics loss factor $L = 0.94$, the solid angle $\Omega_{\mathrm{PD}} = 8.3 \times 10^{-4}$ (with a 1-inch lens at 220 mm distance from the MOT), the dipole radiation enhancement factor $F_{\mathrm{dip}} = 1$ and the gain $G = 10^8\ \mathrm{V/A}$ which according to Eq. (3.1) results in a conversion factor of $C_{\mathrm{PD}} = 7.6 \times 10^6\,\mathrm{atoms/V}$. With all these numbers we can such relate the signal voltage to the atom number. At this gain the 10% to 90% rise time of the detection setup is $370\ \mu\mathrm{s}$.

Absorption images are taken by shining an on-resonant imaging beam addressing the broad closed transition at 461 nm on the atoms and by subsequently recording the atomic absorption on a CMOS camera (Imaging Development Systems GmbH, UI-3240ML-NIR-GL) on the opposite side of the chamber. The imaging beam has a $1/e^2$ radius of $5.5\ \mathrm{mm}$ and a power of typically a few μW, which results in a low saturation parameter of $I/I_{\mathrm{sat}} \sim 10^{-4}$. Turning on and off the imaging beam is controlled by an AOM, with a rise time of $< 1\ \mu\mathrm{s}$. The objective in front of the camera has a magnification of $0.22(2)$, and each pixel of the camera chip in the atom plane corresponds to a length of $24(2)\ \mu\mathrm{m}$. The imaging beam collimator and the camera are located at two opposing CF16 viewports of our science chamber [not shown in Fig. 4.1 (a)].

In each experimental cycle we take three pictures: one with the imaging beam and atoms (Abs), one with the imaging beam and without atoms (Div), and one without both (Bg). Following the Lambert-Beer law the optical density for each position (x, y) is calculated by:

$$\mathrm{OD}(x,y) = -\ln\left(\frac{I_{\mathrm{Abs}}(x,y) - I_{\mathrm{Bg}}(x,y)}{I_{\mathrm{Div}}(x,y) - I_{\mathrm{Bg}}(x,y)}\right). \tag{4.1}$$

Then a two-dimensional Gaussian function with six fitting parameters is fitted to this optical density map, i.e. the peak optical density OD_0, the two Gaussian standard deviations σ_x and σ_y, the two MOT center position coordinates x_0 and y_0, and an angle θ adjusting the x and y directions. Assuming that the density distribution of the MOT is Gaussian, the atom number can then be calculated by

$$N_{\mathrm{at}} = \frac{2\pi\,\sigma_x\sigma_y \mathrm{OD}_0}{\sigma_{\mathrm{abs},0}}\,, \tag{4.2}$$

with the on-resonant absorption cross section $\sigma_{\mathrm{abs},0} = 3\lambda^2/2\pi = 1.01 \times 10^{-13}\ \mathrm{m}^2$. This atom

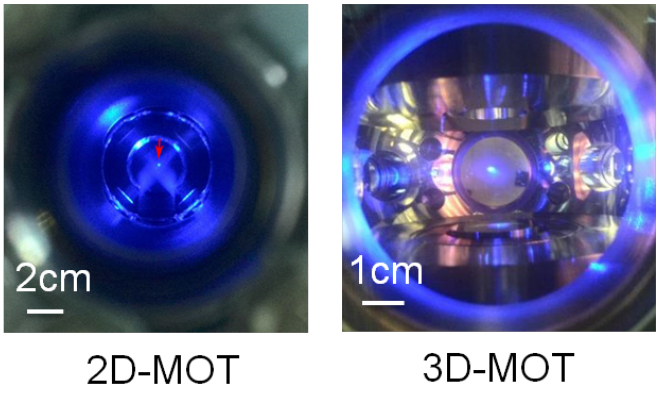

Fig. 4.2 Fluorescence pictures of the blue 2D- and 3D-MOTs. The length bar in each picture refers to the focal plane where the atoms are located.

number is consistent with the atom number obtained by the photodiode fluorescence within a factor of two.

We can then calculate the peak atomic density of our MOT by

$$n_a = \frac{N_{\mathrm{at}}}{(2\pi)^{3/2}\sigma_x\sigma_y\sigma_z}\,, \tag{4.3}$$

whereby the MOT size along the third unseen direction is approximated with the geometric mean of the two fitted directions, $\sigma_z = \sqrt{\sigma_x\,\sigma_y}$.

4.2 Loading of the broad-line MOT

In this section, first loading curves in different conditions and the loss mechanism in the broad-line MOT are introduced in Sec. 4.2.1. Then the dependences of the MOT loading rates on various 2D-MOT parameters are investigated in Sec. 4.2.2. The effect of additional Zeeman slowing in the 2D-MOT is investigated in Sec. 4.2.3.

4.2.1. Loading and loss mechanism

The blue 3D-MOT is located 335 mm downstream from the 2D-MOT. Fluorescence pictures of both are shown in Fig. 4.2.

Atoms of the cold atomic beam emerging from the 2D-MOT are captured by the blue cooling beams, which typically have a power of 7 mW each and a red detuning of 30 MHz. The magnetic field gradient is typically set to $40\,\mathrm{G/cm}$ along the z symmetry axis. By turning the blue cooling beams on by a mechanical beam shutter and measuring the rising atom fluorescence on a photodiode, MOT loading curves can be measured. The laser beams involved in the 2D-MOT atom source and the MOT magnetic field gradient are on during all the time. MOT loading curves for the ^{88}Sr isotope are shown for the four situations with repumping beam on/off and

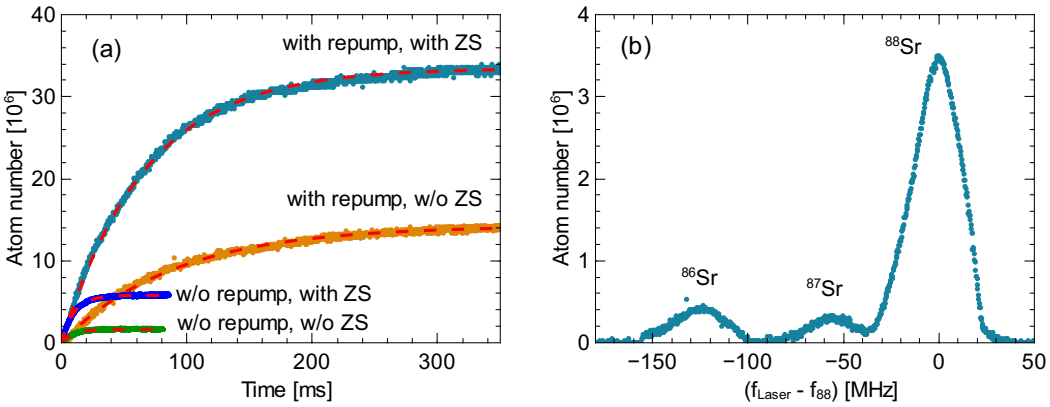

Fig. 4.3 Loading curves and isotope spectrum of the blue MOT. (a) ^{88}Sr MOT loading curves with and without the repumping and the Zeeman slower (ZS) beams. Dashed red curves are fits which solve the MOT rate equation with a one-body loss rate. The repumping beam enhances the MOT lifetime, while the Zeeman slower beam enhances the MOT loading rate. (b) Isotope spectrum of the blue MOT when scanning the frequency of the blue laser (f_{Laser}) relative to the optimum frequency for trapping of ^{88}Sr (f_{88}).

the Zeeman slower beam on/off in Fig. 4.3 (a).

While an additional repumping beam at 481 nm increases the loading time, an additional Zeeman slower beam increases the initial slope of the loading curve. Both beams increase the atom number in steady state. The repumping enhancement, which we define as the atom number in the presence of the repumper divided by the atom number without the repumper, $F = N_{\mathrm{rep}}/N_{\mathrm{no\ rep}}$, is about one order of magnitude. As the blue MOT operates on a nearly closed transition, it can be operated without a repumper and still trap $10^6 \ldots 10^7$ atoms, which is contrary to MOTs consisting of alkali atoms.

All loading curves are fitted by saturating exponentials of the form

$$N(t) = \frac{L}{R}[1 - \exp(-R\,t)]\ , \tag{4.4}$$

which are solutions to the rate equation $\dot{N} = L - RN$ for the MOT atom number N, with the loading rate L and the one-body loss rate R. From the good quality of the fits we conclude that two-body losses are not significant in our atomic density regime. At higher atomic densities two-body losses in a strontium MOT become important [117].

An isotope spectrum of the blue MOT without the repumper is shown in Fig. 4.3 (b). It is obtained by scanning the frequency of the blue laser (f_{Laser}) relative to the optimum frequency for trapping of ^{88}Sr (f_{88}). Such, the frequencies of the 2D-cooling, the Zeeman slower, the pushing and the blue cooling beams which all originate from the blue laser were changed all together. The MOT fluorescence for the three isotopes ^{88}Sr, ^{87}Sr and ^{86}Sr are visible on this plot at different frequencies, reflecting the isotope shifts on the blue transition. The fluorescence of a

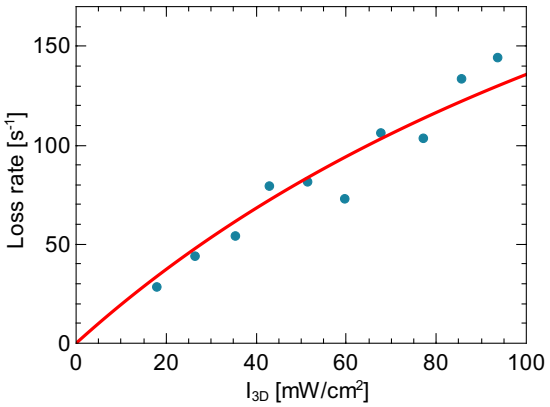

Fig. 4.4 Blue MOT loss rate versus the cooling beam intensity. The experimental data (blue dots) is fitted with Eq. (4.5) (red line), with the only fitting parameter $\Gamma_{^1\mathrm{P}_1\rightarrow{}^1\mathrm{D}_2}$.

^{84}Sr MOT can also be seen on our photodiode at the isotope shift of -271 MHz [192], however due its low natural isotope abundance (0.56% [98]) only at a larger gain of the preamplifier, and such it is not shown in this plot.

A measurement of the MOT loss rate R versus cooling laser intensity is presented in Fig. 4.4. The cooling beam detuning is set to $\Delta_{3\mathrm{D}} = -1\ \Gamma$. For higher intensities, the loss rate increases from $30\ \mathrm{s}^{-1}$ to $140\ \mathrm{s}^{-1}$, which corresponds to $1/e$ loading times in the range from $35\ \mathrm{ms}$ to $7\ \mathrm{ms}$. The experimental data is fitted with the curve [103, 106]

$$R = \frac{1}{2}\frac{I_{3\mathrm{D}}/I_{\mathrm{sat}}}{1 + I_{3\mathrm{D}}/I_{\mathrm{sat}} + 4\Delta_{3\mathrm{D}}^2/\Gamma^2}\Gamma_{^1\mathrm{P}_1\rightarrow{}^1\mathrm{D}_2}B_{^1\mathrm{D}_2\rightarrow{}^3\mathrm{P}_2}\ , \tag{4.5}$$

with the combined cooling beam intensity $I_{3\mathrm{D}} = 6\,I_{\mathrm{max}}$, the cooling beam detuning $\Delta_{3\mathrm{D}}$, the decay rate $\Gamma_{^1\mathrm{P}_1\rightarrow{}^1\mathrm{D}_2} = 3.85(1.47)\times 10^3\ \mathrm{s}^{-1}$ [107] and the branching ratio $B_{^1\mathrm{D}_2\rightarrow{}^3\mathrm{P}_2} = 1/3$. This formula follows from the model that the MOT loss rate is determined by the $5\mathrm{s}5\mathrm{p}\,{}^1\mathrm{P}_1 \rightarrow 5\mathrm{s}4\mathrm{d}\,{}^1\mathrm{D}_2 \rightarrow 5\mathrm{s}5\mathrm{p}\,{}^3\mathrm{P}_2$ decay channel, which depends on the fraction of atoms in the $5\mathrm{s}5\mathrm{p}\,{}^1\mathrm{P}_1$ state and on the subsequent decay rate and branching ratio. Atoms decaying to the $5\mathrm{s}5\mathrm{p}\,{}^3\mathrm{P}_1$ state are not lost from the MOT, as this state is relatively short-lived and atoms do not leave the MOT capture volume on that time scale. The decay rate due to collisions with background atoms ($\sim 0.1\,\mathrm{Hz}$) is small and can be neglected, see Sec. 4.4. The only fitting parameter is $\Gamma_{^1\mathrm{P}_1\rightarrow{}^1\mathrm{D}_2}$. The fitted result is $2.4\times 10^3\ \mathrm{s}^{-1}$ which is still within the error bar of the literature value [107].

Except being lower by one order of magnitude, the loss rate in the presence of the repumping beam follows the same cooling beam intensity dependence (not shown in Fig. 4.4). Similarly to this intensity dependence, smaller loss rates were observed for larger cooling beam detunings. The findings about the dominant loss channel from the blue MOT are thus consistent with earlier studies [103, 106].

While the loss rate has a clear dependence on the cooling beam intensity, the atom number is roughly constant in the cooling beam intensity range of 20 ... $100\ \mathrm{mW/cm^2}$, both without and with the repumper. The atom number reaches a peak around $\sim 7 \times 10^7$ atoms around a small magnetic field gradient of $20\ \mathrm{G/cm}$, in the presence of the repumping beam. For higher gradients the atom number decreases to $\sim 2 \times 10^7$ atoms at $60\ \mathrm{G/cm}$. Here the atom number largely follows the shrinking MOT volume, while the atomic density stays roughly constant around $6 \times 10^9\ \mathrm{cm^{-3}}$.

The temperature of the MOT is measured by a time-of-flight technique expansion technique [193]. The cooling beam is extinguished by a mechanical beam shutter and the originally trapped atoms expand for a variable time t, after which their shadow is imaged on a camera. The magnetic field gradient is kept on during the atom expansion and is turned off $100\ \mu\mathrm{s}$ before the imaging pulse. To the measured MOT size two Gaussians are fitted, with standard deviations σ_x and σ_y. The squares of these standard deviations are then plotted over the squared time, see Fig. 4.5. To the experimental data we then fit the formula $\sigma^2(t) = \sigma_0^2 + \frac{k_B T}{m} t^2$, with the mass of a strontium atom $m = 88\,u$, and with the only fitting parameter being the temperature T. The fit results are $4.9(1)\ \mathrm{mK}$ for the x axis and $2.8(1)\ \mathrm{mK}$ for the y axis. While the reason for the different temperatures along the two axes is unclear during the time of writing this thesis, the approximate value of a few mK is in agreement with the reported values of other groups [125, 194]. It is a few times larger than the Doppler temperature of the cooling transition of $770\ \mu\mathrm{K}$. One reason for the higher temperature could be the relatively large cooling beam intensity in this measurement, as it is known from the literature that the temperature in a strontium blue MOT rises to a few times over the Doppler limit for high cooling beam intensities and small detunings [106].

4.2.2. Dependences on 2D-MOT parameters

The MOT loading rate as a function of the pushing beam intensity I_p is shown in Fig. 4.6 (a). The loading rate reaches a peak at pushing beam intensities around $I_p = 0.2\, I_{\mathrm{sat}}$, beyond which it decreases rapidly as I_p becomes larger. The red triangles depict the following model calculation, in which we multiply the atomic flux Φ_{tot} from Fig. 3.4 (c) with the normalized longitudinal velocity distribution $f(v_x)$ and the normalized transverse density distribution $T(r, \sigma_r)$ of the atomic beam, with its standard deviation from the center axis σ_r, which are integrated up to a finite capture velocity v_c and capture radius r_c of the MOT:

$$L = \Phi_{\mathrm{tot}} \int_0^{v_c} \mathrm{d}v_x\, f(v_x) \int_0^{r_c} \mathrm{d}r\, 2\pi r\, T(r, \sigma_r)\ . \tag{4.6}$$

The capture radius is set to the $1/e^2$ radius of the MOT cooling beams of $6\,\mathrm{mm}$. Thus, the

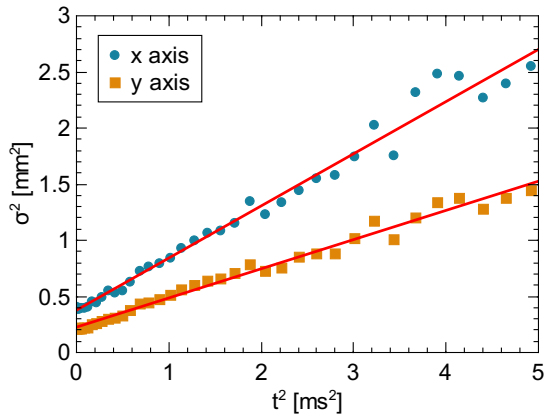

Fig. 4.5 Blue MOT temperature. The used method is the time-of-flight technique. The squares of the MOT sizes (Gaussian standard deviations) along two directions are plotted versus the squared expansion time with the cooling beams off. The linear fits to the data show that the atoms have temperatures of a few mK.

only free parameter in the model is the capture velocity v_c. As the 3D-MOT loading rate was measured under slightly different conditions as the data given in Fig. 3.4 concerning 2D-MOT parameters, we have also included a scaling parameter of the loading rate, which we find to range between 0.2 and 2. Comparison with measured data as shown, e.g., in Fig. 4.6 (a), yields 3D-MOT capture velocities between $20\,\mathrm{m/s}$ and $30\,\mathrm{m/s}$, which lies slightly below an estimate based on the actual parameters of the 3D-MOT laser intensities and beam sizes.

From this model, we deduce that the initial increase of the loading rate reflects the increase of the total flux of Fig. 3.4 (c), while the decrease at larger pushing beam intensities results from the finite capture efficiency of longitudinal velocities beyond the capture velocity, see Fig. 3.4 (a) for the longitudinal velocity trend. Larger pushing beam intensities lead to a better collimation of the atomic beam, but also to too high velocities such that the atoms can not be captured anymore. The estimated capture efficiency at maximum loading rate is around 10%.

The loading rate as a function of $I_{2\mathrm{D}}$, which is the peak intensity of the four 2D-MOT cooling beams combined, is shown in Fig. 4.6 (b). It rises monotonically with increasing $I_{2\mathrm{D}}$ beyond a threshold value of about I_{sat}, while at larger intensities it begins to saturate. The data is fitted by the function $L = a\,[(I_{2\mathrm{D}}/b)/(1 + I_{2\mathrm{D}}/b)]^2$. The setup of this function is motivated by i) the 2D-MOT loading rate scaling with the fourth power of the 2D-MOT capture velocity, $L_{2\mathrm{D}} \propto v_{c,2\mathrm{D}}^4$, see Eq. (B.18) in the Appendix B.2 about the model for the 2D-MOT loading rate, and ii) by the scaling $v_{c,2\mathrm{D}} \sim [s/(1+s)]^{1/2}$ with $s = I_{2\mathrm{D}}/b$ [118, 162]. Hereby it is assumed that the loading rates of the 3D- and the 2D-MOTs are proportional to each other, $L \propto L_{2\mathrm{D}}$. The fitted values are $a_{\mathrm{fit}} = 3.0(3) \times 10^8\,\mathrm{s}^{-1}$ and $b_{\mathrm{fit}} = 3.7(4)\,I_{\mathrm{sat}}$. This means that according to the fit the 3D-MOT loading rate saturates around the point when the combined

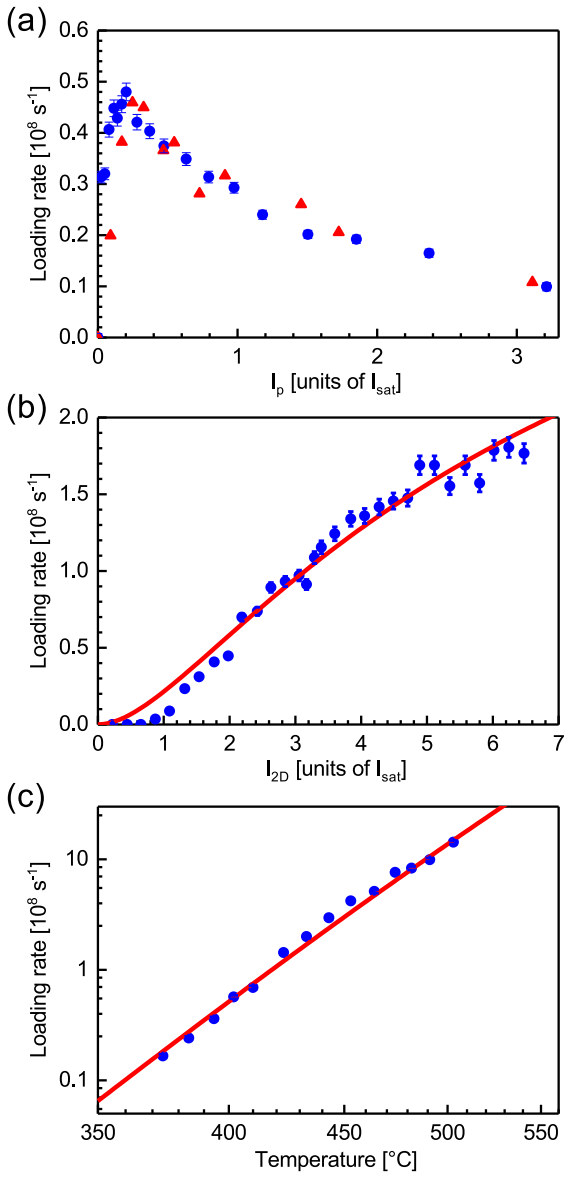

Fig. 4.6 Blue MOT loading rate as a function of 2D-MOT parameters. For each panel, the unvaried parameters are set to $I_p = 0.2\ I_{\mathrm{sat}}$, $I_{\mathrm{2D}} = 4\ I_{\mathrm{sat}}$ (four beams combined), and $T_{\mathrm{oven}} = 465\ ^{\circ}\mathrm{C}$, respectively. (a) Loading rate versus the pushing beam light intensity. The triangles indicate results of a model calculation. (b) Loading rate versus the 2D-MOT cooling beam light intensity. The solid line represents a fit with a model. (c) Loading rate versus the oven temperature, using flux enhancement of the 2D-MOT by the decreasing field Zeeman slower for this set of measurements. The solid line represents a model calculating the flux from the strontium vapor pressure and the 2D-MOT capture efficiency. Details on all model calculations can be found in the text.

average intensity of two 2D-MOT cooling beam reaches I_{sat}. While this model quantitatively captures the essential trend of the observed data, it fails to qualitatively reproduce the observed threshold of the loading rate at smaller intensities.

The loading rate versus the oven temperature is shown in the double-logarithmic plot in Fig. 4.6 (c). It increases with temperature and shows no sign of saturation. The same behavior was measured for the flux of the cold atomic beam. The data is fitted by the function $L = a \times P(T) \times T^{-5/2}$, with the single fitting parameter a and the saturated vapor pressure of solid strontium $P(T)$ at temperature T [101]. Here we again assume that the loading rates of the 3D- and the 2D-MOTs are proportional to each other, $L \propto L_{\mathrm{2D}}$. According to Eq. (B.18), $L_{\mathrm{2D}} \propto P(T) \times T^{-5/2}$. Comparing to this model, we conclude that there is no additional loss mechanism up to oven temperatures of $500\,^{\circ}\mathrm{C}$. We obtain the maximum 3D-MOT loading rate of $1.4 \times 10^{9}\,\mathrm{s}^{-1}$ for ^{88}Sr in our experiment. We expect to achieve higher loading rates by further increasing the oven temperature, but so far did not dare to do so in order to avoid rapid depletion of the oven or possible damage to our apparatus, in particular the Zeeman slower viewport. At the oven operating temperature of $465\,^{\circ}\mathrm{C}$ the pressure in the oven is about two orders of magnitude lower than at $600\,^{\circ}\mathrm{C}$, the latter being a common oven operating temperature in strontium setups employing a Zeeman slower [64, 104].

The pushing beam detuning can be varied in about the range $-\Gamma \ldots +\Gamma$ without significantly lowering the 3D-MOT loading rate, if the pushing beam intensity is accordingly adjusted for each detuning. For the red-detuned side the optimum pushing beam intensity is higher than for the blue-detuned side.

By adjusting the laser frequencies appropriately, we have operated the 2D- and 3D-MOTs under conditions to capture each of the stable isotopes of strontium. Their loading rates at our typically used oven temperature of $465\,^{\circ}\mathrm{C}$ are summarized in Table 4.1. We find that for the bosonic isotopes the loading rates in this experimental run are consistent with the natural abundancies, which indicates that the physical processes of the 2D- and 3D-MOTs do not depend on the isotope, as expected from the simple level structure. The slightly lower loading rate for fermionic ^{87}Sr is likely due to its unresolved hyperfine structure on the cooling transition.

We also measured the influence of a repumping beam in the 2D-MOT on the MOT loading rate. The repumping beam, with a $1/e^2$ radius of 4 mm and an average intensity of $10\,\mathrm{mW/cm^2}$, is overlapped with the Zeeman slower beam. On resonance it enhances the MOT loading rate by about $20\,\%$. This enhancement is observed for a wide range of parameters, such as for different repumping beam sizes, for different 2D-MOT cooling beam intensities and with or without an applied additional Zeeman slower beam. The optimum repumping frequency is red-detuned as if compared to the optimum frequency in the 3D-MOT, which is an indication for that the

Isotope	Statistics	Abundance [98]	Δf [MHz] [192, 195]	$L\,[10^6\ \mathrm{s}^{-1}]$	L_{rel}
^{88}Sr	Bosonic	82.58%	0	480(18)	1
^{87}Sr	Fermionic	7.00%	-51.9	35(2)	0.87(6)
^{86}Sr	Bosonic	9.86%	-124.8	61(2)	1.06(5)
^{84}Sr	Bosonic	0.56%	-270.8	3.5(8)	1.0(3)

Table 4.1 Overview of achieved blue MOT loading rates at an oven temperature of $465\ ^{\circ}\mathrm{C}$ for all stable isotopes of strontium. Atomic flux enhancement of the 2D-MOT by the decreasing field Zeeman slower was used for this set of measurements. Δf is the relative frequency shift to ^{88}Sr for the singlet cooling transition. L_{rel} shows the relative loading rate to ^{88}Sr, scaled with the natural abundance.

repumping enhancement stems from atoms which are not completely slowed down yet along the axis to the Zeeman slower viewport. However, in our setup we do not permanently shine a repumping beam on the 2D-MOT, as it would need additional optics and add to the complexity of the setup.

4.2.3. Effect of Zeeman slowing

Motivated by the results for a sodium 2D-MOT reported by Lamporesi *et al.* 2013 [120], we investigated the effect of an auxiliary Zeeman slower realized in the fringe field of the permanent magnet configuration. The fringe magnetic field, with the increasing field region ① and the decreasing field region ②, is shown in the right graph of Fig. 3.1, while the coordinate system used in the following is introduced in the left part of Fig. 3.1.

By switching the Zeeman slower beam on and off, we measure the enhancement factor of the 3D-MOT loading rate with and without the Zeeman slower beam for different Zeeman slower beam powers and frequencies in the decreasing field region ②, see Fig. 4.7. Using the decreasing field region ②, a maximum enhancement of 4 is observed at an optimum detuning of $\Delta_Z = -210\,\mathrm{MHz}$ (corresponding to $-6.6\,\Gamma$) and a maximum available peak intensity of the Zeeman slower beam of $I_Z = 1.2\,I_{\mathrm{sat}}$ ($1/e^2$ radius 6 mm) at the position of the atoms. This beam intensity corresponds to a laser power of 37 mW before the vacuum system. We find that for a smaller detuning the enhancement factor is generally smaller and saturates at a lower light intensity. For example, at the detuning of $\Delta_Z = -175\,\mathrm{MHz}$ ($-5.5\,\Gamma$), we observe an enhancement factor of 3 at a low intensity of $I_Z = 0.3\,I_{\mathrm{sat}}$, where it already shows clear signs of saturation versus power.

In the increasing slope region ① of the magnetic field we also find a Zeeman slowing

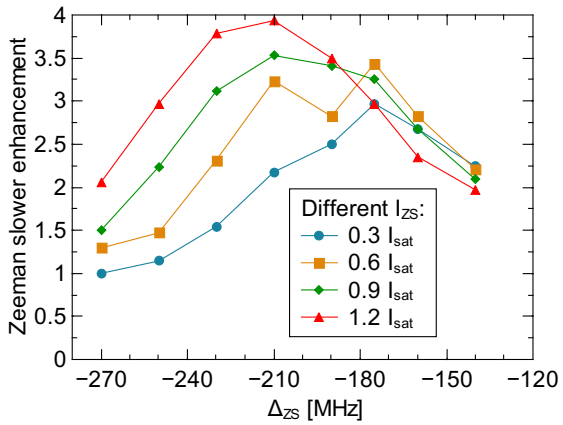

Fig. 4.7 Blue MOT loading rate enhancement due to an additional Zeeman slower beam. The loading rate enhancement is shown for different Zeeman slower beam detunings Δ_{ZS} and intensities I_{ZS}.

effect, at an about 300 MHz higher red-detuning, yet with a smaller enhancement factor of 2. This region should in principle be better suited for slowing strontium atoms, as it has a smaller magnetic field slope at most of its positions, and as at a too high slope the atoms can not be decelerated fast enough in the Zeeman slower beam light field anymore. Nevertheless, we find that region ② is more effective for Zeeman slowing. One possible reason is that the slowing effect is disrupted in region ① before atoms are trapped in the 2D-MOT, due to collisions with surrounding hot atoms.

As a comparison, using the increasing slope region of the fringe magnetic field Lamporesi *et al.* 2013 [120] measured an enhancement factor of 12 for sodium atoms at laser intensities corresponding to an order of magnitude higher saturation for the Zeeman slower and using larger beam diameters capturing more atoms. Therefore, we would expect a larger enhancement effect of the Zeeman slower if more laser power was available in our setup.

4.3 Repumping from the $^3P_2$ state

To gain a better understanding about the repumping enhancement, we perform frequency scans of the repumper over resonance for different repumping beam average intensities. The scan speed is $\approx 80\ \mathrm{MHz}/100\ \mathrm{ms}$. Resulting example spectra for the ^{88}Sr isotope are shown in Fig. 4.8 (a). It can be seen that for higher intensities the enhancement becomes larger on- as well as off-resonance. The on-resonant enhancement and the FWHM linewidth of the repumping enhancement deduced from these spectra are then shown in Fig. 4.8 (b). The enhancement saturates around 10 for high intensities. However, in our experiment we observed an enhancement of up to about 20 for the low-abundance isotope ^{84}Sr in another measurement, which is certainly

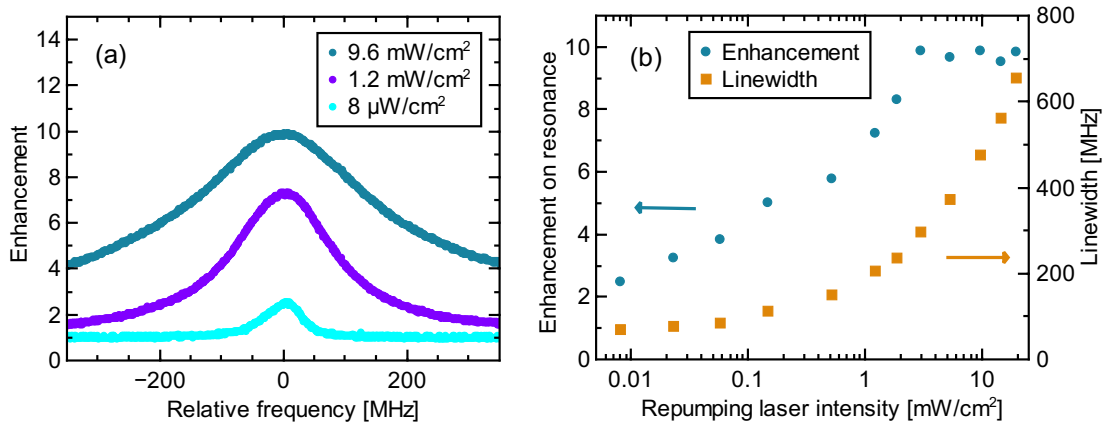

Fig. 4.8 Atom number enhancement in the blue MOT due to the repumping beam. (a) Enhancement spectra for for different repumping beam intensities and detunings. (b) On-resonant enhancement and FWHM linewidths for different repumping beam intensities.

related to the lower steady-state MOT atom number of that isotope as there is no saturation. The linewidth is ~ 70 MHz for low intensities, and then rises proportional to the square root of the intensity from a repumping intensity of a few 100s of $\mu\mathrm{W/cm}^2$ on. From this measurement it can be seen that the requirement on the frequency stability of the repumping beam is not high, as for intensities from around $10\ \mathrm{mW/cm}^2$ on the repumping enhancement has a linewidth of a few 100s of MHz.

One possible reasons for the limited repumping enhancement on resonance are the not very well-known decay channels $5s5p\,{}^1P_1 \rightarrow 5s5p\,{}^3P_0$ and $5s5p\,{}^1P_1 \rightarrow 5s4d\,{}^3D_1 \rightarrow 5s5p\,{}^3P_0$ [109]. The branching ratios from the $5s5p\,{}^1P_1$ to the $5s5p\,{}^3P_{0,1,2}$ states were estimated to be about $< 0.01 : 2 : 1$ [109]. Another possible reason is that atoms leave the repumping beam (with $1/e^2$ radius 2.5 mm) before they get repumped. The latter loss mechanism could be especially important for atoms falling into anti-trapped m_J states of the transient $5s4d\,{}^1D_2$ state or the metastable $5s5p\,{}^3P_2$ state, such that the available time for repumping is lower due to the acceleration of the atoms in the magnetic field.

4.4 Magnetic trapping of $^3P_2$ atoms

Neutral atoms can be magnetically trapped in a quadrupolar magnetic field [196, 197]. Following theoretical proposals for magnetic trapping of metastable two-electron atoms [113, 198], experimentally realized magnetic trapping of strontium atoms in the $5s5p\,{}^3P_2$ state was for the first time described in Ref. [114].

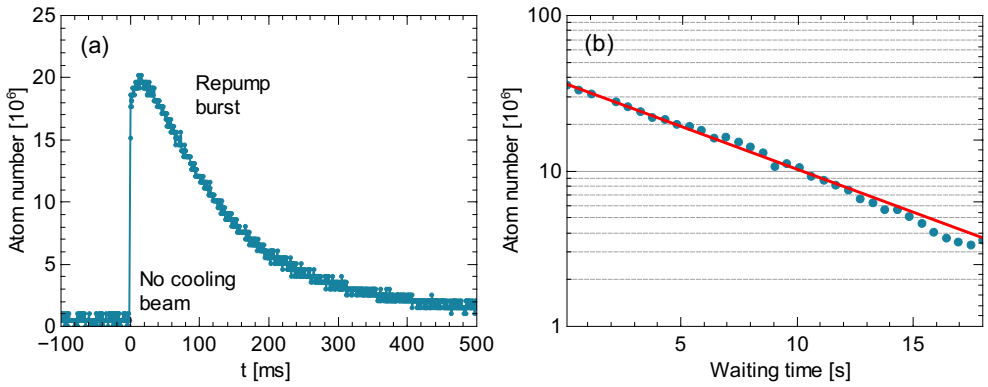

Fig. 4.9 Magnetic trap lifetime. (a) Example for a fluorescence burst when the repump and cooling beams are turned on after a variable waiting time. (b) The maximum of the fluorescence burst is plotted over waiting time. The data is fitted by a decaying exponential, with a $1/e$ decay time of $7.9(1)$ s. The magnetic field gradient is set to 58 G/cm for this measurement.

The depth of the magnetic trap is given by [114]

$$U_{\mathrm{MT}} = -\boldsymbol{\mu}\,\boldsymbol{B} = \mu_B\, g_J\, m_J\, \frac{\partial B_z}{\partial z} \sqrt{\frac{x^2}{4} + \frac{y^2}{4} + z^2}\,, \tag{4.7}$$

with the Landé g-factor for the $5s5p\,{}^3P_2$ state $g_J = 3/2$, the magnetic quantum number m_J and the magnetic field gradient along the symmetry axis of the quadrupole coil $\partial B_z/\partial z$. From this it can be seen that only atoms in the low-field seeking $m_J = 1$ and $m_J = 2$ states are trapped. With $m_J = 2$, with the maximum magnetic field gradient in our setup of $60\ \mathrm{G/cm}$ and with the maximum distance along the z direction of $30\ \mathrm{mm}$, which is given by the distance from the MOT to the lower re-entrant glass surface, the magnetic trap depth corresponds to $760\ \mathrm{MHz}$, which translates to a temperature of $36\ \mathrm{mK}$ and a velocity of $3\ \mathrm{m/s}$. From this it can be seen that only cooled atoms from the MOT can be trapped in the magnetic trap, but not possibly existing metastable atoms emerging from the 2D-MOT in the cold atomic beam, whose atoms typically have velocities which are larger than $10\ \mathrm{m/s}$.

To get information about the lifetime of the $5s5p\,{}^3P_2$ atoms in our magnetic trap, the magnetic trap is first loaded for a constant loading time of 5 s, and then the blue cooling beam is turned off for a variable waiting time while the magnetic field is still on. Then the blue cooling beam is turned on again together with the repumping beam, and the amplitude of the fluorescence spike originating from the repumped atoms is measured, see Fig. 4.9 (a). The fluorescence maximum is plotted versus waiting time in Fig. 4.9 (b). An exponential decay function is fitted to the experimental data, with the fitted $1/e$ decay time of $7.9(1)$ s.

The atom lifetime due to collisions with background atoms, also called vacuum lifetime, is given by [141, 199]

$$\tau_{\mathrm{bg}} = \sqrt{\frac{\pi\, m\, k_B\, T}{8}}\, \frac{1}{\sigma\, P}\,, \tag{4.8}$$

with the mass of an atom m, the environment temperature T, the collision cross section of a trapped atom with a background atom σ and the background pressure P. At room temperature, at a pressure of 1.7×10^{-9} mbar (which is the pressure in our science chamber according to the ion gauge readout) and with a collision cross section of 10^{-17} m^2 (which is the typical order of magnitude for collisions between trapped atoms and background atoms [199]), we calculate a vacuum lifetime of 9 s. This is very close to our measured value of $7.9(1)$ s. This good agreement might be coincidental, as there is a large uncertainty in the theoretical calculation, due to the uncertainty of the collision cross section of a strontium atom with background atoms, which are most likely N_2 molecules in our case. Our result also agrees well with the measurement of the pressure dependence of the magnetic trap lifetime in Ref. [114].

Lifetimes of $5s5p\,^3P_2$ atoms in the magnetic trap of 30 s [97] and of 54 s [173] were measured by other groups, which in presence of a good vacuum are limited by black-body coupling to subsequently decaying slightly higher-lying $5s4d\,^3D_J$ states [115]. At this background our atom lifetime is most likely limited by collisions with background atoms.

When the blue MOT is operated for a few seconds and the repumping beam is suddenly turned on, then $5s5p\,^3P_2$ atoms get pumped back into the ground state and a huge fluorescence spike is seen on the photodiode, see Fig. 4.10 (a). The $5s5p\,^3P_2$ state acts as a reservoir state, and the fluorescence spike corresponds to atoms stored in that reservoir. In our setup, it can be up to 50 times higher than the MOT fluorescence without repumper. This fluorescence spike is followed by an exponential fluorescence decay on the time scale of the MOT lifetime with repumping beam on, ~ 100 ms. The fluorescence then equilibrates at the steady-state fluorescence level of the blue MOT with the repumping beam continuously on. We measure the magnetic trap atom number over loading times for different magnetic field gradients, by recording the fluorescence spike when turning on the repumper, see Fig. 4.10 (b). It can be seen that at a low gradient of 15 G/cm the magnetic trap is not efficient, certainly due to the low trap depth. It works the best with the highest gradient realized in our setup, 58 G/cm.

In Ref. [200], a higher magnetic trap loading rate and atom number were achieved by shining an additional laser beam at 688 nm addressing the $5s5p\,^3P_1 \rightarrow 5s6s\,^3S_1$ transition of strontium during the magnetic trap loading phase. Like this, atoms decaying from the $5s4d\,^1D_2$ to the $5s5p\,^3P_1$ state are pumped to the $5s6s\,^3S_1$ state and then have a high probability to decay to the $5s5p\,^3P_2$ state and to enter the magnetic trap (for a level scheme of strontium see Fig. 2.2). Atom number gains in the magnetic trap of 65% were achieved for the bosonic isotopes of strontium [200].

The idea of pumping atoms from the $5s5p\,^3P_1$ to one of the two long-lived metastable $5s5p\,^3P_{2,0}$ states could also have interesting applications in Rydberg physics. If performed at

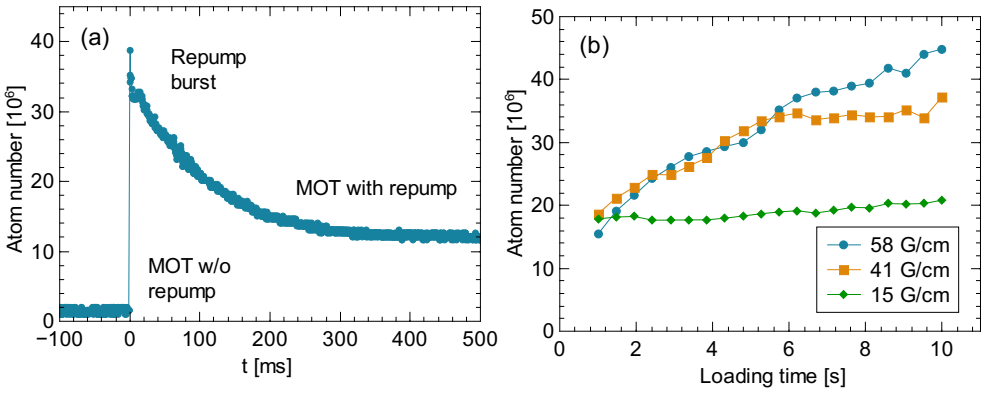

Fig. 4.10 Magnetic trap loading. (a) Example for a fluorescence burst when the repumping beam is turned on during the blue MOT after a variable loading time. (b) The maximum of the fluorescence burst is plotted over loading time for three different magnetic field gradients.

the end of the red MOT or in an optical dipole trap, then the atoms could already have gained a higher phase space density than achievable in the blue MOT or its accompanying magnetic trap. The metastable atoms could then be trapped in a dipole trap acting on a metastable state, and they could be coupled to Rydberg states with a single-photon transition, at wavelength 318 nm, with the advantages of having high potential Rabi couplings to the Rydberg state and having no additional decay term due to an intermediate state. The atom could then be coupled to the $5sns\,{}^3\mathrm{S}_1$ Rydberg series, which due to its isotropic van der Waals interactions is often preferred over P Rydberg series. The clock $5s5p\,{}^3\mathrm{P}_0$ state is certainly preferred over the magnetically trappable $5s5p\,{}^3\mathrm{P}_2$ state as it has a lower two-body loss rate [201] and would such allow for higher metastable state densities.

4.5 Narrow-line cooling and trapping

After strontium atoms are accumulated in the magnetic trap in the $5s5p\,{}^3\mathrm{P}_2$ state, they are repumped to the ground state by an a few ms long light pulse at wavelength 481 nm and trapped in the red MOT [68, 69, 71, 72, 126–129, 202]. The red MOT is operated at a lower magnetic field gradient than the blue MOT, as high gradients in order to achieve high magnetic trap depths are not necessary during this stage and can be even disadvantageous, as the magnetic field gradient shifts the atoms out of resonance on a too small length scale and thus limits the size of the MOT. When loading atoms into the red MOT, the magnetic field gradient is ramped down from $40\ \mathrm{G/cm}$ to $5\ \mathrm{G/cm}$ within $100\ \mu\mathrm{s}$.

During the operation of the red MOT, the blue cooling beams are blocked by a mechan-

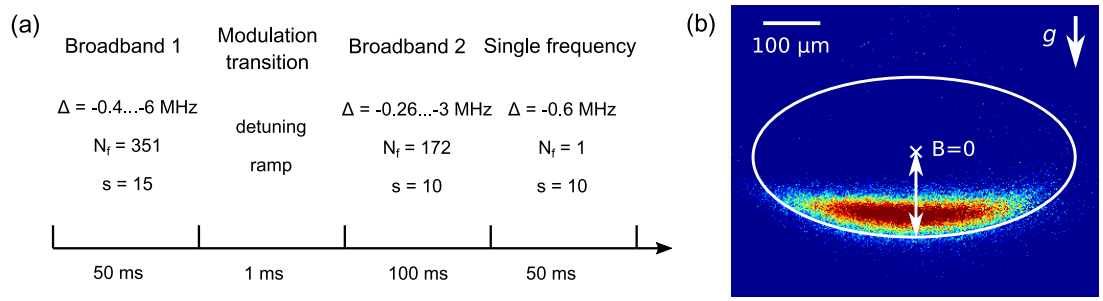

Fig. 4.11 Operation of the red MOT. (a) Detunings to the $^1\mathrm{S}_0 \rightarrow {}^3\mathrm{P}_1$ transition Δ, numbers of frequency sidebands N_f and saturation parameters s during the different phases of the red MOT. (b) An absorption picture of the red MOT during its last single-frequency phase. The cold atoms accumulate below the magnetic field center ($B = 0$) at position δz where the Zeeman shift equals the detuning of the cooling beam. The direction of the gravitational acceleration is indicated by the single-sided white arrow.

ical beam shutter. [①] The repumped atoms initially have a temperature of a few mK which corresponds to a Doppler width of a few MHz. As this width is three orders of magnitudes larger than the natural linewidth of the atomic transition addressed by the red cooling beam, $\Gamma_{689}/2\pi = 7.5$ kHz, the cooling beam is frequency-broadened in the first phase of the red MOT in order to address all velocity classes.

This first phase of the red MOT is called the first broadband phase, see Fig. 4.11 (a). In that phase, the 3 mW power of each cooling beam is near equally distributed on $N_f = 351$ frequency sidebands, which are equally spaced each $\gamma = 16$ kHz in the frequency range which corresponds to detunings of $-0.4 \ldots -6$ MHz from the atomic transition. The generation of frequency sidebands is achieved by sending a comb of RF frequencies to the red cooling beam AOM. The RF frequency comb is generated by the DDS-based AOM driver (Moglabs, XRF421), through sending commands controlling the microcontroller and FPGA inside the driver. The saturation parameter per frequency sideband of the red cooling beam, $s = I/(N_f\, I_{\mathrm{sat}})$, with $I_{\mathrm{sat}} = 3\ \mu\mathrm{W/cm}^2$ on the red transition, is around 15 in the first broadband phase. Hereby I is defined as being the peak intensity of a single cooling beam, following the definition in Refs. [71, 72]. This saturation parameter corresponds to a power-broadened linewidth of $\Gamma' = \Gamma_{689}\sqrt{1+s} = 30$ kHz, which is larger than the frequency sideband spacing γ. Such, the red cooling beam addresses all velocity classes.

After the first broadband phase, which typically lasts for 50 ms, the range of frequencies of

[①] This is necessary, as if the blue cooling beams are only extinguished by turning off an AOM in their beam paths, then the red MOT can be disturbed by the residual $\sim 1\,\%$ power leaking through the turned-off AOM. This can be understood by comparing the involved light forces of the blue and the red cooling beams: The residual $\sim 1\,\%$ blue cooling light power still accelerates the atoms on the order of $1000\ \mathrm{m/s}^2$, which is one order of magnitude larger than the maximum achievable light force on the red transition of $150\ \mathrm{m/s}^2$.

the red cooling beam is continuously narrowed down in a ramp lasting for 1 ms. After that the second broadband phase follows, lasting for 100 ms and with 172 frequency sidebands in the frequency range with detunings of -0.26 ... -3 MHz. Also in this phase the power-broadened linewidth per frequency sideband is larger than the frequency sideband spacing.

The single-frequency phase follows as the final phase of the red MOT, with a typical red detuning of 600 kHz, a saturation parameter of 10 and a power-broadened linewidth of 25 kHz. In this phase the red MOT has a pancake shape, as can be seen on the absorption picture in Fig. 4.11 (b). This distinctive shape is characteristic for the red MOT when the cooling beam detuning Δ is much larger than the power-broadened linewidth, $|\Delta|/\Gamma' \gg 1$ [71, 129]. In that regime, as due to the small involved cooling beam light forces gravity plays an important role in distributing the atoms, they accumulate on the lower shell of the ellipsoid where the cooling beam detuning equals the Zeeman shift. Along the vertical axis they accumulate at the position

$$\delta z \simeq \frac{\Delta}{\frac{\mu_B}{h} g_J \, m_J \frac{\partial B_z}{\partial z}} \, , \tag{4.9}$$

with the Landé g-factor of the $^1\mathrm{S}_0 \rightarrow {}^3\mathrm{P}_1$ transition $g_J = 1.5$. At a cooling beam detuning of $\Delta/2\pi = 600$ kHz and a magnetic field gradient of 5 G/cm, the atoms such accumulate ~ 600 μm below the magnetic field center, at a magnetic field of ~ 300 mG.

The atoms are measured to have a 1.3 μK temperature in the final single-frequency phase, measured by the TOF technique. Lower temperatures would be attainable in the 'quantum' regime when the saturation parameter drops below unity, $s \leqslant 1$ [71, 72, 129]. This is opposite to the so-called power-broadened regime in which the saturation parameter $s > 1$ [129]. In our setup, we trap up to 10^6 atoms of the ^{88}Sr isotope at peak densities of 10^{10} cm^{-3}.

Chapter 5 Ultracold strontium Rydberg atoms

After a cloud of strontium atoms is laser-cooled to temperatures in the low μK regime, the unwanted Doppler broadening is reduced to a low level of about 100 kHz. Apart from this, the atoms often can be approximated to be stationary on the time scale of the Rydberg state lifetime of about 100 μs, which is called the *frozen Rydberg gas* approximation. In this condition, we want to excite strontium atoms to Rydberg states, in order to investigate their properties and to ultimately use them for quantum simulation applications.

In this chapter first the properties of Rydberg atoms in general as well as of strontium Rydberg atoms in particular are introduced in Sec. 5.1. Then the first experimental results of excitations of strontium atoms to triplet Rydberg states in our laboratory, both in the blue and in the red MOTs, are described in Sec. 5.2.

5.1 Properties

General properties of Rydberg atoms, including related experimental techniques, were recently reviewed by Refs. [25, 51, 135, 203–205]. An excellent overview about the properties of Rydberg atoms can also be found in the thesis of P. Schauß [206].

In this section first the extreme scalings of the property values of Rydberg atoms with the principal quantum number n of the Rydberg state are introduced in Sec. 5.1.1. This is followed by a description of the huge and tunable interatomic Rydberg interactions in Sec. 5.1.2. While these two sections describe the properties of single-electron Rydberg atoms, in the next Sec. 5.1.3 some of the specific properties of the strontium Rydberg atom are described, which is a two-electron system. The latter section includes a discussion about when the single-electron treatment is valid for an accurate description of strontium Rydberg atom properties, and in which cases the second valence electron has to be taken into account in the description.

5.1.1. General properties

The discussion in this section largely follows the book of T. F. Gallagher about Rydberg atoms [23]. Rydberg atoms are atoms with an electron being in a highly excited state, with the principal quantum number $n \gtrsim 10$. Their understanding and study played an important role in the history of atomic physics. The frequencies of visible transitions to Rydberg states of the hydrogen atom were for the first time described by the Balmer formula in 1885. Swedish physicist J. Rydberg

then analyzed the measured transition frequencies of hydrogen and of other alkali atoms, and he realized that an additional term δ_{nlj} is needed to describe the frequencies for a certain series of an atom species.

The term δ_{nlj} is nowadays known as the quantum defect. It is unique for each Rydberg series of an atom species, which comprises all Rydberg states with different principal quantum numbers n but with the same orbital quantum number l and total angular momentum quantum number j. While the quantum defect mostly depends on the orbital quantum number l, additional weak dependences on n and j exist. For a single-electron system, the binding energy of a Rydberg state is given by

$$E_n = -\frac{\mathrm{Ry}^*}{(n-\delta_{nlj})^2} = -\frac{\mathrm{Ry}^*}{(n^*)^2} \,, \tag{5.1}$$

with $\mathrm{Ry}^* = \frac{1}{1+m_e/m}\mathrm{Ry}$ for an atom with mass m and with the electron mass m_e, and the Rydberg unit of energy being given by

$$\mathrm{Ry} = \frac{m_e e^4}{8\epsilon_0^2 h^2} = 13.6\ \mathrm{eV} \,. \tag{5.2}$$

Hereby the effective principal quantum number n^* was introduced, which is simply the principal quantum number n which is lowered by the quantum defect δ_{nlj}. The physical origin of the quantum defect is the non-complete screening of the Coulomb potential of the positively charged nucleus by negatively charged inner electrons. Because of this the quantum defect is zero for the hydrogen atom as here no inner electrons exist. It is larger for Rydberg states with low orbital quantum numbers l, as their Rydberg electron wave functions have larger amplitudes towards the nucleus, such that the nuclear potential can not be completely screened by the inner electrons. This results in the quantum defects for Rydberg series with low angular quantum number l, i.e. the $n\mathrm{s}_{1/2}$, $n\mathrm{p}_j$ and $n\mathrm{d}_j$ series for the alkali atoms, having distinctively different values which results in non-degenerate energy levels. The quantum defect for alkali and alkaline-earth-like atoms has values of up to ≈ 4 for $l = 0$ states [207]. Contrary to this, the quantum defects for high-l states for $l \geqslant 3$ are close to zero, which results in the so-called degenerate hydrogen manifold.

The quantum defect can be expanded by the Rydberg-Ritz formula, which reveals its n-dependence:

$$\delta_{nlj} = \delta_{lj,0} + \frac{\delta_{lj,2}}{(n-\delta_{lj,0})^2} + \frac{\delta_{lj,4}}{(n-\delta_{lj,0})^4} + \dots \,. \tag{5.3}$$

Various properties dependent on n^* of Rydberg atoms are summarized in Table 5.1. They are highlighted further in the following. From Eq. (5.1) it can already be seen that the binding energy of a Rydberg atom scales as $\propto (n^*)^{-2}$. At large n, the energy spacing between adjacent

Quantity	n^* scaling
Binding energy E_{n^*}	$(n^*)^{-2}$
Level spacing $\delta E_n = E_n - E_{n+1}$	$(n^*)^{-3}$
Orbital radius r_{orb}	$(n^*)^{2}$
Dipole matrix element $\mu_{\mathrm{gr}} = \langle r\|d\|g\rangle$	$(n^*)^{-3/2}$
Dipole matrix element $\mu_{\mathrm{rr'}} = \langle r\|d\|r'\rangle$	$(n^*)^{2}$
Radiative lifetime τ_{rad}	$(n^*)^{3}$
Ionizing electric field $\mathcal{E}_{\mathrm{ioniz}}$	$(n^*)^{-4}$
d.c. polarizability $\alpha_{\mathrm{d.c.}}$	$(n^*)^{7}$

Table 5.1 Overview about n^*-scalings of Rydberg atom properties.

n-levels scales as $\delta E_n \propto (n^*)^{-3}$. Additionally, the orbital radius r_{orb} of the Rydberg electron scales as $\propto (n^*)^2$, which results in a scaling of the geometrical cross section of a Rydberg atom as $\propto r_{\mathrm{orb}}^2 \propto (n^*)^4$. This large geometrical cross section for example leads to fast collision rates of Rydberg atoms in dense thermal gases.

The scalings described so far can be deduced from the Bohr model of the atom. For the following discussions, however, the quantum mechanical wave functions of the Rydberg electrons are needed. The dipole matrix element $\mu_{\mathrm{gr}} = \langle r|d|g\rangle$, with the dipole operator $d = -e\,r$ and the electron position r, from a low-lying state $|g\rangle$ to a Rydberg state $|r\rangle$ scales with $\propto (n^*)^{-3/2}$, as with higher n the location probability of the Rydberg electron near to the core becomes smaller. From this it follows that the value of the Rabi frequency on that transition (at a fixed laser electric field) scales in the same way, $\Omega_{\mathrm{gr}} \propto \mu_{\mathrm{gr}} \propto (n^*)^{-3/2}$. On the other hand, dipole matrix elements between neighboring Rydberg states, $|r\rangle$ and $|r'\rangle$, scale as $\mu_{\mathrm{rr'}} \propto (n^*)^2$.

The lifetime of a Rydberg state is determined by several effects. A Rydberg state can decay by a collision with another atom, which can lead to a de-excitation or to ionization of the Rydberg atom. The latter ionization process is also called Penning ionization. In cold Rydberg gases, however, due to the small velocity and the short typical time scale of the experiment, collisions typically can be neglected. Apart from collisions, Rydberg states can decay to a lower-lying state by the spontaneous emission of a photon. In the dipole approximation, the spontaneous decay rate of state $|i\rangle$ to state $|f\rangle$ in free space scales as [188]

$$\Gamma_{|i\rangle\rightarrow|f\rangle} \propto \omega_0^3\,\mu_{fi}^2\,, \tag{5.4}$$

with the angular frequency ω_0^3 and the dipole matrix element μ_{fi} of the respective transition. From this formula it can be seen that the decay rate from a Rydberg state $|r\rangle$ to a low-lying state $|g\rangle$ scales as $\propto \mu_{\mathrm{gr}}^2 \propto (n^*)^{-3}$, as in this case the transition frequency is about constant. For the decay rate scaling from a Rydberg state to a nearby lower Rydberg state the additional

$\propto \omega_0^3$ dependence has to be taken into account, and the decay rate scales as $\propto (\delta E_n)^3 \mu_{\mathrm{rr'}}^2 \propto (n^*)^{-9+4} = (n^*)^{-5}$. From these scalings it can be seen that decays to low-lying states are the dominant decay channels, if they are dipole-allowed. Decays to nearby Rydberg states, however, are the dominant decay channels for high-l states, which results in a $\propto (n^*)^5$ scaling of their lifetimes. On the other hand, the lifetime of low-l states due to spontaneous decay scales as $\propto (n^*)^3$.

Another decay or population redistribution mechanism is absorption of or stimulated emission by a black-body photon. The absorption scales as $\propto (n^*)^{-2}$ [208]. This depopulation dominates over the radiative decay to the ground state for $n \gtrsim 40$. Absorption of a black-body photon can also lead to photoionization of a Rydberg atom [209, 210]. Combining the radiative decay and the black-body contributions, the Rydberg state lifetime is given by:

$$\tau_{\mathrm{Ry}} = \left(\frac{1}{\tau_{\mathrm{rad}}} + \frac{1}{\tau_{\mathrm{bbr}}} \right)^{-1}. \tag{5.5}$$

The ionizing electric field of a Rydberg state is given by $\mathcal{E}_{\mathrm{ioniz}} \simeq \mathcal{E}_0/(16\,(n^*)^4)$, with $\mathcal{E}_0 = 5.1 \times 10^9\,\mathrm{V/cm}$ being the electric field which is experienced by a ground state electron in the hydrogen atom. This has the result that already a small electric field allows for the ionization of a Rydberg atom, after which the resulting ion can be detected by ion detection techniques. For low-l states and for weak electric fields $\mathcal{E}$ the Stark shift is quadratic, $\Delta E_{\mathrm{Stark}} = -\frac{1}{c}\alpha_{\mathrm{d.c.}}\mathcal{E}$, with the d.c. polarizability $\alpha_{\mathrm{d.c.}}$ scaling as $\propto (\mu_{\mathrm{rr'}})^2/\delta E_n \propto (n^*)^7$.

The hyperfine splitting for Rydberg $l = 0$ states scales as $\propto (n^*)^{-3}$ [211, 212]. Also the isotope shift due to the volume effect for $l = 0$ states scales as $\propto (n^*)^{-3}$ [211].

5.1.2. Rydberg interactions

To understand interactions between Rydberg atoms, a model is helpful which is outlined in Fig. 5.1 (a). Two interacting atoms A and B are approximated to be three-level systems. All the three states $|\mathrm{s}\rangle$ (with energy E_{s}), $|\mathrm{r}\rangle$ (with energy set to zero) and $|\mathrm{t}\rangle$ (with energy E_{t}) are Rydberg states, and both individual atoms are initially in state $|r\rangle$. The $|\mathrm{r}\rangle \leftrightarrow |\mathrm{s}\rangle$ and $|\mathrm{r}\rangle \leftrightarrow |\mathrm{t}\rangle$ transitions are connected by the dipole matrix elements $\boldsymbol{\mu}_s$ and $\boldsymbol{\mu}_t$, while the $|\mathrm{s}\rangle \leftrightarrow |\mathrm{t}\rangle$ transition is dipole-forbidden.

To simplify the description of our system, one can perform a multipole expansion of the Coulomb interactions in the range of interatomic separations $R_{\mathrm{LR}} \ll r \ll \lambda/2\pi$, where R_{LR} is the LeRoy radius and $\lambda/2\pi$ is the reduced transition wavelength, with the wavelength of the involved $|\mathrm{r}\rangle \leftrightarrow |\mathrm{s}\rangle$ or $|\mathrm{r}\rangle \leftrightarrow |\mathrm{t}\rangle$ transition λ [24]. The LeRoy radius is the distance to an atom from where the wave functions of the two Rydberg atoms do not overlap with each other and exchange interactions can be neglected. It can be approximated by the formula $R_{\mathrm{LR}} \approx$

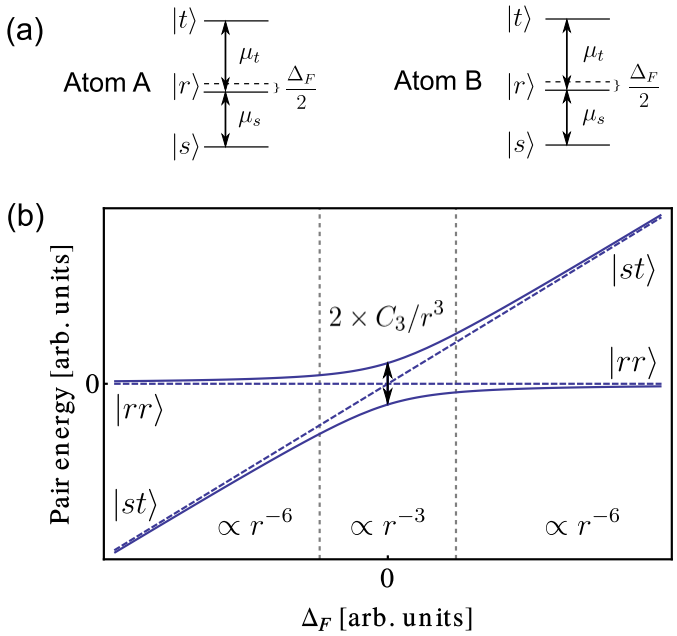

Fig. 5.1 Dipolar interactions between two Rydberg atoms. (a) Atomic level structure: Both atoms have the same three-level structure and dipole matrix elements, with all of the states being Rydberg states. The intermediate Rydberg state $|r\rangle$ is offset from the center of the two other Rydberg states $|s\rangle$ and $|t\rangle$ by half the Förster defect Δ_F. (b) Eigenvalues of the combined two-atom system in the pair state basis $\{|\mathrm{rr}\rangle, |\mathrm{st}\rangle\}$ according to Eq. (5.8) for different Förster defects Δ_F at a constant interatomic distance r. The continuous lines are the pair state energies with interaction, while the dashed lines are shown for vanishing interaction. At the Förster resonance of $\Delta_F = 0$ the pair state energies show an avoided crossing, with an energy gap of $2 \times C_3/r^3$ between the two pair states. The vertical dashed lines denote the crossover regions between the resonant dipole-dipole (scaling as $\propto r^{-3}$) and the van der Waals interactions (scaling as $\propto r^{-6}$) at $\Delta_F = \pm 2\, C_3/r^3$.

$5a_0(n^*)^2$ for alkali atoms [213] and is $\simeq$ 0.6 μm for $n = 50$. The maximum interatomic distance is given by the reduced transition wavelength which is on the order of 1 mm for the $|50\mathrm{s}_{1/2}\rangle \rightarrow |50\mathrm{p}_j\rangle$ transition of rubidium. Typical values for distances between next neighbors in ultracold gases are $r \approx n_a^{-1/3} = 1 \ldots 20$ μm, corresponding to atomic densities of $n_a = 10^{12} \ldots 10^8$ cm^{-3}. They such usually lie in the range for which the multipole expansion is justified. The leading order of the multipole expansion is the dipole-dipole interaction potential, felt by each of the two atoms: [①]

$$U_{\mathrm{dd}} = \frac{1}{4\pi\epsilon_0}\left(\frac{\boldsymbol{\mu}_s \cdot \boldsymbol{\mu}_t}{r^3} - \frac{3\,(\boldsymbol{\mu}_s \cdot \boldsymbol{n})\,(\boldsymbol{\mu}_t \cdot \boldsymbol{n})}{r^3}\right). \tag{5.6}$$

[①] In a more rigorous derivation, the dipole-dipole interaction potential has an additional r^{-1} term, differing by a factor of $\approx (kr)^2$ to the r^{-3} term, with k being the wave number of the associated transition [24, 25]. This so-called retarded dipole-dipole potential has its physical origin in the finite speed of the electromagnetic interaction. While the angular integral of the r^{-3} term vanishes, the angular integral of the r^{-1} term is finite. As its magnitude is small in ultracold Rydberg gases, however, it was not needed to describe experimental data up to now.

Here, the unit vector of the interatomic separation vector $\boldsymbol{n} = \boldsymbol{r}/r$ was used. For simplicity, in the following we ignore the angular-dependence term of the dipole-dipole interactions on the right side of Eq. (5.6), which is valid for isotropic interaction, such that $U_{\mathrm{dd}} = (4\pi\epsilon_0)^{-1}\mu_s\mu_t/r^3$. Apart from that, to get some insight into the interactions, it is then instructive to restrict ourselves to the pair state basis $\{|\mathrm{rr}\rangle, |\mathrm{st}\rangle\}$, out of the originally nine pair states of the two-atom system of three-level atoms. Then the system Hamiltonian is given by

$$H = \begin{pmatrix} 0 & U_{\mathrm{dd}} \\ U_{\mathrm{dd}} & \Delta_F \end{pmatrix} . \tag{5.7}$$

Hereby the Förster defect $\Delta_F = E_{\mathrm{s}} + E_{\mathrm{t}}$ is introduced, with $\Delta_F \ll E_{\mathrm{s,t}}$ in our system. The eigenvalues of this Hamiltonian are given by:

$$U_{\mathrm{rr,st}} = \frac{\Delta_F}{2} \mp \sqrt{\frac{\Delta_F^2}{4} + \frac{C_3^2}{r^6}} . \tag{5.8}$$

In this step, the C_3 coefficient was introduced, as $C_3 = (4\pi\epsilon_0)^{-1}\mu_s\mu_t$. The eigenenergies are plotted in Fig. 5.1 (b). Dependent on the size of the interaction, C_3/r^3, compared to half the Förster defect, $\Delta_F/2$, two limiting cases of the electric dipole-dipole interaction can be described: the van der Waals and the resonant dipole-dipole interaction.

(1) Van der Waals interaction This interaction type occurs in the regime $C_3/r^3 \ll \Delta_F/2$. These interactions are often present between two atoms in the same Rydberg state. A Taylor expansion yields the energy shift for the $|\mathrm{rr}\rangle$ and $|\mathrm{st}\rangle$ states,

$$U_{\mathrm{rr,st}}^{\mathrm{vdW}} = -\frac{\Delta_F}{2} \mp \left(\frac{\Delta_F}{2} + \frac{C_6}{r^6} \right) . \tag{5.9}$$

Here the van der Waals coefficient $C_6 = C_3^2/\Delta_F$ is defined. It is worth noting that ground-state atoms, having a positive Förster defect Δ_F, always display attractive van der Waals interactions, while excited atoms can both interact attractively or repulsively, dependent on the neighboring level structure. An interesting feature of the C_6 coefficient is its strong n^*-dependency:

$$C_6 \propto \frac{C_3^2}{\Delta_F} \propto \frac{\mu_{rr'}^4}{\Delta_F} \propto \frac{(n^*)^8}{(n^*)^{-3}} = (n^*)^{11} . \tag{5.10}$$

(2) Resonant dipole-dipole interaction This interaction type occurs in the regime $C_3/r^3 \gg \Delta_F/2$, that means if the Förster defect approaches zero and the two pair states become degenerate. In this case, the energy shifts are much larger than in the van der Waals case, and they are given by:

$$\Delta U_{\mathrm{rr,st}}^{\mathrm{res}} = \frac{\Delta_F}{2} \mp \frac{C_3}{r^3} . \tag{5.11}$$

The energy shift has a weaker n^*-dependency with $\propto (n^*)^4$. By setting the two interactions equal, one can estimate the crossover distance at which the transition between these two interactions occurs:

$$r_{\mathrm{short}} = \left(\frac{C_3}{\Delta_F}\right)^{1/3}. \tag{5.12}$$

For typical experimental and atomic parameters it is below $1\ \mu\mathrm{m}$. If present, the resonant dipole-dipole interaction yields much bigger interaction strengths between two Rydberg atoms at a given bigger distance than the van der Waals interaction. It is possible to tune the value of r_{short} ideally to infinity by tuning the Förster defect to zero. An experimentally widely employed technique for this is the application of an electric field, taking advantage of different d.c. polarizabilities of the different atomic states. Enhanced resonant dipole-dipole interactions, as if compared to the van der Waals case, can also occur at certain distances and angles where the energies of two pair states cross.

Two other aspects are worth noting: First, resonant dipole-dipole interactions will generally be present between two atoms in different Rydberg states ϕ_1 and ϕ_2, via the exchange interaction channel $|\phi_1\phi_2\rangle \leftrightarrow |\phi_2\phi_1\rangle$. And second, the populations of the two pair states oscillate at a frequency of $f_{\mathrm{osc}} = 2|C_3/r^3|/h$ [34], on typically a much faster time scale than the Rydberg state lifetime. The population transfer can be coherent at cold temperatures [214]. This means that resonant energy transport can be observed in cold Rydberg gases, similar to FRET (Förster Resonant Energy Transport) in biology [215], which was the reason to call the degeneracy between two pair states a Förster resonance [216].

The exact form of the angular dependence of the resonant dipole-dipole interaction depends on the absolute change of the combined magnetic quantum number $|\Delta M| = |\Delta m_{jA}| + |\Delta m_{jB}| \in \{0, 1, 2\}$, with $\Delta m_{jA}, \Delta m_{jB} \in \{-1, 0, +1\}$ being the changes of the magnetic quantum numbers of atoms A and B [217]. The three types of theoretically expected angular dependencies were experimentally confirmed [34, 218].

As the van der Waals interaction is the most commonly present in cold Rydberg atom experiments, the calculation of C_6 coefficients is of special importance. For the determination of the van der Waals interaction between a pair of atoms in the pair state $|rr\rangle$ one has to sum C_3^2/Δ_F over all the possible dipole-coupled pair states. Due to the many coupled channels, the angular dependency of van der Waals interactions is not trivial and can in some cases be both positive and negative for different angles. A truncated basis of thousands of pair states is usually employed to let the C_6 coefficient converge. [213, 217, 219] The multipole expansion approach, however, fails to describe interactions accurately at small interatomic distances. At

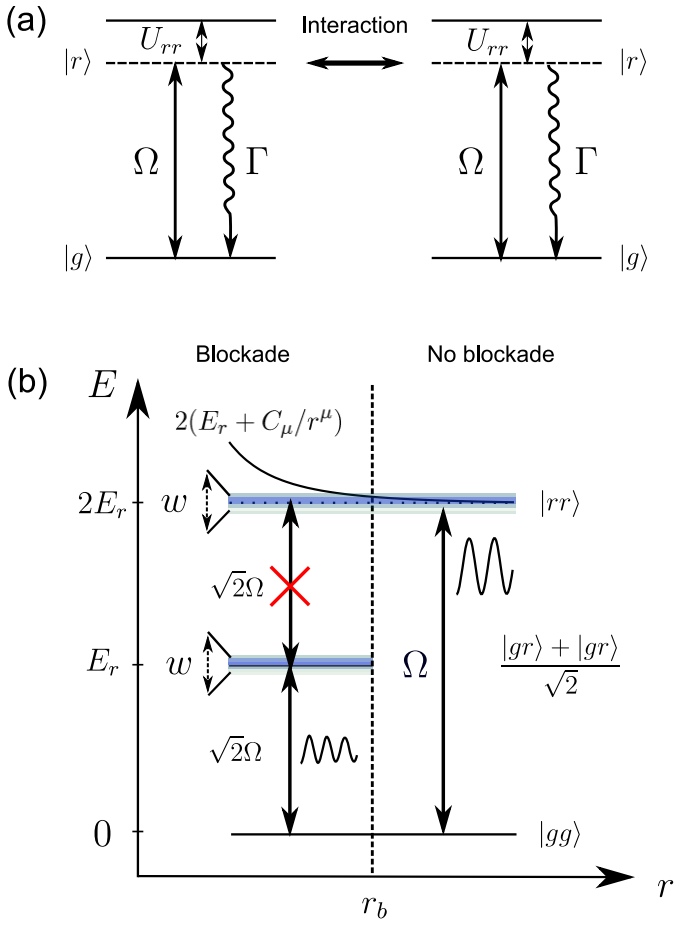

Fig. 5.2 Illustration of Rydberg blockade in a two-atom system. a) Level scheme of two interacting two-level Rydberg atoms which are subject to a laser field. The laser field is resonant with the atomsic bare transitions in the absence of interatomic Rydberg interactions U_{rr}. b) Illustration of the blockade radius r_b. For $r > r_b$ the two-atom system oscillates with the single-atom Rabi frequency between the states $|gg\rangle$ and $|rr\rangle$. For $r < r_b$ the doubly-excited state $|rr\rangle$ is shifted out of resonance, as its interaction shift $2\,C_\mu/r^\mu$ is bigger than the excitation linewidth w. In this case, the two-atom system oscillates between the ground state and the symmetric singly-excited state with the collective Rabi frequency $\sqrt{2}\Omega$.

these small distances the complete Hamiltonian has to be constructed and diagonalized [220]. Avoided crossings and state mixing between interacting pair states at low interparticle spacings are then predicted, a feature that the multipole expansion approach fails to describe [220–222].

The strong Rydberg interactions can lead to a phenomenon called Rydberg blockade [26, 27]. The respective physical situation is illustrated in Fig. 5.2 (a). Two atoms are both approximated by a two-level system with a ground state $|g\rangle$ and a Rydberg state $|r\rangle$, whereby the latter one decays with spontaneous decay rate Γ. The two atoms are driven by a laser beam, in resonance if Rydberg interactions can be neglected and with Rabi frequency Ω. Additionally, the two Rydberg states experience the energy shift U_{rr} due to the Rydberg interaction.

The resulting two-atom level scheme is shown in Fig. 5.2 (b). For small interatomic distances r the long-range Rydberg interaction $U_{rr} = C_\mu / r^\mu$ can exceed the excitation bandwidth w, which for typical experiments is either given by the Rabi frequency Ω or the laser linewidth γ, such that the doubly-excited state $|rr\rangle$ is shifted out of resonance. For van der Waals interaction $\mu = 6$ and for resonant dipole-dipole interaction $\mu = 3$. The crossover distance between the blockaded and the not blockaded regime is given by

$$r_b = \left(\frac{2|C_\mu|}{\hbar w} \right)^{1/\mu}, \tag{5.13}$$

which is calculated by setting the Rydberg interaction equal to the excitation bandwidth. As the blockade volume is a sphere for isotropic interaction, r_b is also called the blockade radius. It is a measure for the transition between the two regimes of resonant driving ($r > r_b$) and suppressed excitation ($r < r_b$).

Furthermore, if double-excitations are suppressed in a blockade sphere with N atoms inside, the Rydberg excitation is shared among these atoms. In the case of perfect blockade there are only two allowed states, i.e. the collective ground and the collective excited state. Due to this simple two-level structure this situation is called a superatom [223]. These two collective states couple with an enhanced collective or many-body Rabi frequency $\Omega_{\mathrm{coll}} = \sqrt{N}\Omega$. A superatom has a bigger optical cross section and is robust versus particle fluctuation or loss as compared with a single atom. Furthermore it can be used as a single-photon [49], single-atom [224] or single-ion source [50, 225] and for quantum information processing [51].

5.1.3. Strontium Rydberg atoms

After a few general properties of Rydberg atoms were introduced, we now take a look on the specific properties of strontium Rydberg atoms.

The experimental study of ultracold strontium Rydberg gases was pioneered by the groups of M. Jones in Durham [53, 57, 132, 157, 226, 227] and of T. Killian and B. Dunning in Houston [54, 58, 228–232]. There also exist recent related studies in strontium atomic beams [233–239]. Recent experimental progress on two-electron Rydberg physics was reviewed by Dunning *et al.* 2016 [55].

Fitted values for the quantum defects for the Rydberg series of strontium are given in Ref. [207]. For the $^3\mathrm{S}_1$ series they are given by $\delta_0 = 3.371(2)$, $\delta_2 = 0.5(2)$ and $\delta_4 = -1(2) \times 10^1$. The quantum defect δ_0 such has a large uncertainty on the 10^{-3} level, which is also the case for the $^3\mathrm{D}_{2,1}$ series and which is due to the limited accuracy of experimental data. For these triplet Rydberg series of strontium the uncertainty of the quantum defect is such around two orders of magnitudes larger than for the $^2\mathrm{s}_{1/2}$ and $^2\mathrm{d}_{5/2,3/2}$ series of rubidium in the 1980s [240], and

around three to four orders of magnitudes larger than for these series of rubidium nowadays [241].

As the overlap of the wave functions of the Rydberg electron and the second valence electron is small, the *single active electron* treatment is often a good approximation also for two-electron Rydberg atoms [207], and it can such serve for the calculation of Rydberg interactions. Thus, the C_6 coefficients, which are often the interaction parameters being of the highest interest in experiments involving cold Rydberg atoms, can be computed from the Rydberg energy levels using the aforementioned quantum defects and from the dipole matrix elements between these levels, as it is the case for single-electron Rydberg atoms. The second valence electron does, however, influence the C_6 coefficients by altering the wave functions of the Rydberg electron, which results in different energy levels and dipole matrix elements. This leads to the $^1\mathrm{S}_0$ series of strontium being attractive, which is contrary to all $^2\mathrm{s}_{1/2}$ series of alkali atoms which are all repulsive [213]. On the other hand, the $^3\mathrm{S}_1$ series of strontium displays repulsive interactions, which are stronger by a factor of around two if compared to the $^2\mathrm{s}_{1/2}$ series of rubidium. The n-dependent C_6 coefficient of the $^3\mathrm{S}_1$ series of strontium is calculated to be: [207]

$$C_6[\mathrm{GHz}\,\mu\mathrm{m}^6] = 1.4448 \times 10^{-19}\, n^{11}(-2.387 \times 10^{-3}\, n^2 + 1.211\, n - 21.18)\,. \qquad (5.14)$$

Another consequence of the modified energy levels is the greater scarcity of Förster resonances, as compared to the alkali atoms. For strontium, only the $2\times5\mathrm{s}35\mathrm{p}\,^3\mathrm{P}_1 \rightarrow 5\mathrm{s}35\mathrm{s}\,^3\mathrm{S}_1 + 5\mathrm{s}36\mathrm{s}\,^3\mathrm{S}_1$ and the $2 \times 5\mathrm{s}37\mathrm{d}\,^3\mathrm{D}_2 \rightarrow 5\mathrm{s}34\mathrm{f}\,^3\mathrm{F}_3 + 5\mathrm{s}35\mathrm{f}\,^3\mathrm{F}_3$ channels were identified, while for Rydberg states of ytterbium and calcium, both being other examples of two-electron systems, no Förster resonances were found [207].

Another more fundamental difference of singly-excited two-electron Rydberg atoms caused by the second valence electron is the existence of perturber states and interseries couplings. Specifically, if a doubly-excited state has the same angular momentum J and parity P as the singly-excited Rydberg state and is nearby in energy, then the doubly-excited state is known as perturber state and is mixed into the Rydberg state wave function, which manifests itself as an energy shift. The condition of the perturber state being nearby in energy to the singly-excited Rydberg state implies that both electrons occupy low-excited states. Additionally, as perturber states are typically very short-lived if compared to Rydberg states, even their small admixtures into the Rydberg state wave functions are responsible for a non-negligible decrease of the Rydberg lifetimes. For strontium, most of the perturber states are made up of the lowest electronic Sr^+ excitations, e.g. $4\mathrm{d}_{3/2}$, $4\mathrm{d}_{5/2}$, $5\mathrm{p}_{1/2}$, $5\mathrm{p}_{3/2}$ and $6\mathrm{s}_{1/2}$. A partial level scheme of the singly-charged strontium ion Sr^+ is shown in Fig. 5.3.

One method to calculate the wave functions of Rydberg states, taking into account mixing

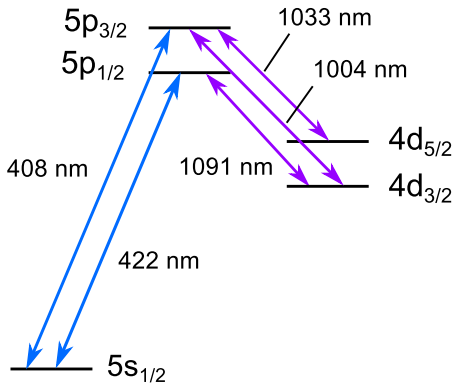

Fig. 5.3 Level scheme of the singly-charged strontium ion Sr^+. The values for the transition wavelengths are taken from Ref. [242].

with perturber states, is multichannel quantum defect theory (MQDT) [59]. A channel is a Rydberg series including its continuum. It can be either a singly-excited channel, e.g. $5sns\,^3S_1$, or a doubly-excited channel, e.g. $5pnp\,^3P_1$. In MQDT, the wave function is expressed as a linear superposition of wave functions from other channels. It relies on input of experimental data of the quantum state energy levels.

For strontium, according to Vaillant *et al.* 2014 [243], the $5sns\,^3S_1$ series appears to be weakly perturbed by the $5p^2\,^3P_1$ doubly-excited state, however more accurate level energies are needed to confirm this result. The $5snd\,^3D_2$ and $5snd\,^3D_1$ series are strongly perturbed at $n < 20$. Additionally, the triplet $5snd\,^3D_2$ series and the singlet $5snd\,^1D_2$ series are strongly coupled to each other. These perturbations or channel fractions become smaller at higher n [243, 244]. Series perturbations due to perturber states and interseries interactions also can influence the Rydberg interactions [245]. This leads to the predicted spin-changing Förster resonance $2 \times 5s30d\,^3D_2 \rightarrow 5s28f\,^1F_3 + 5s27f\,^3F_3$, in which a triplet Rydberg state evolves into a singlet Rydberg state and vice versa [246].

The second valence electron can be used for the detection of Rydberg atoms. In general, the ion core of a strontium Rydberg atom can be excited at visible wavelengths, see Fig. 5.3. The D_2 and D_1 lines of the strontium ion Sr^+ are the $5s_{1/2} \rightarrow 5p_{3/2}$ transition at 408 nm and the $5s_{1/2} \rightarrow 5p_{1/2}$ transition at 422 nm, see Fig. 5.3. For low angular quantum numbers L of the Rydberg electron, an excitation of the ion core results in fast autoionization on the picosecond timescale, due to the large overlap of the Rydberg and the low-lying excited state electrons. The resulting ion can then be accelerated in an electric field and be detected on an ion detector, e.g. on a micro-channel plate [53]. Due to a laser beam which addresses the ion transition, this Rydberg detection method is spatially selective, which is an otherwise hard-to-achieve feature in detection schemes of Rydberg atoms. By this method the electric field distribution could be measured accurately, due to the large Rydberg d.c. polarizability [57].

For high angular quantum numbers L of the Rydberg electron no autoionization occurs, but the D_2 and D_1 ion transitions are closed transitions, at least if one does not consider decays to the metastable $4\mathrm{d}_j$ states. Thus it is possible to use those transitions for fluorescence imaging of Rydberg atoms and to distinguish between different L states [58].

5.2 Experimental results

In this section experiments on excitations of ultracold strontium atoms to triplet Rydberg states are described, with the atoms being held either in the blue or in the narrowband red MOT. By atom loss spectroscopy, a Rydberg loss feature in the red MOT with a ~ 1 MHz linewidth is achieved. First the excitation level scheme and the loss channels are described in Sec. 5.2.1. Then the actual experimental results for the Rydberg excitations are described for the blue MOT in Sec. 5.2.2, and for the red MOT in Sec. 5.2.3.

5.2.1. Principle of Rydberg loss spectroscopy

In our laboratory, we perform Rydberg excitations by a two-photon excitation scheme, see Fig. 5.4. A successful excitation to a Rydberg state can be shown by the loss of ground state atoms. The used method is called atom loss spectroscopy. Atoms are lost due to decay channels from Rydberg states to the two long-lived metastable $^3\mathrm{P}_{2,0}$ states, which have lifetimes on the order of 100 s at room temperature and of thousands of years for bosonic isotopes, respectively (see Sec. 2.1.4 for more details on the metastable state lifetimes). These lifetimes are much longer than the time scale of our experimental cycles.

To get an estimate about the fraction of atoms which decay from a Rydberg state to one of the two long-lived metastable *dark* states, the Wigner 6J symbols for the respective direct decays are calculated. This is only an estimate, as no indirect decay paths are taken into account in our calculation, which could alter the decay fractions. An additional weak dependence on the transition wavelengths of the dipole matrix elements is neglected, as it only creates changes of the relative decay rates on the percent level. The result for the $5\mathrm{s}n\mathrm{s}\,^3\mathrm{S}_1$ series are the decay probabilities of 5/9 to $^3\mathrm{P}_2$, 3/9 to $^3\mathrm{P}_1$ and 1/9 to $^3\mathrm{P}_0$, see also Ref. [156]. In other words, about 2/3 of the Rydberg atoms decay to one of the two long-lived metastable states. This loss mechanism due to decays to metastable states, which is specific for triplet Rydberg states of alkaline-earth atoms, is qualitatively similar to loss due to decays to another hyperfine ground state, which also exists in alkali atoms.

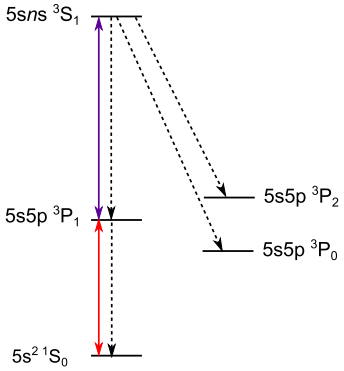

Fig. 5.4 Level scheme for Rydberg excitation. A triplet Rydberg state is excited by a two-photon excitation scheme from the ground state via the metastable $5s5p\,^3P_1$ state. It can then ultimately decay to the metastable $5s5p\,^3P_{2,0}$ states which are lost from the experiment.

5.2.2. Rydberg excitation in the broad-line MOT

In this experiment we excite strontium atoms via the $5s^2\,^1S_0 \rightarrow 5s5p\,^3P_1 \rightarrow 5s45s\,^3S_1$ two-photon pathway. While the lower transition is addressed by a red laser beam at 689 nm, the upper transition is addressed by a UV laser beam. To avoid confusion regarding the UV excitation wavelength, it shall be noted that while from the $5s5p\,^3P_1$ state a $318.2\,\mathrm{nm} \approx 318\,\mathrm{nm}$ photon is needed to reach the first ionization threshold, the transition to the $5s45s\,^3S_1$ Rydberg state is addressed with a $318.8\,\mathrm{nm} \approx 319\,\mathrm{nm}$ photon. The UV beam is linearly polarized along the gravity (z) axis, has a $1/e^2$ radius of $0.8\,\mathrm{mm}$ and is generated by frequency doubling of a dye laser (for more details on the laser system see Sec. 2.4).

The experimental setup and sequence for Rydberg loss spectroscopy in the blue MOT are shown in Fig. 5.5 (a) and (b). While the blue MOT is continuously loaded by the cold atomic beam resulting from the 2D-MOT, it is exposed by both the UV and the red excitation beams, with the latter originating from the red cooling beam collimators. For each UV frequency, the MOT fluorescence is recorded on a photodiode without and with the UV beam for 100 ms each. The fluorescence average of the last 20 ms of each of these two steps is converted into the atom numbers N_1 and N_2. Only the last 20 ms are taken in each step, as the blue MOT needs sufficient time to equilibrate on a time scale of $\sim 10\,\mathrm{ms}$. Then the fraction of remaining atoms during UV exposure N_2/N_1 is recorded for each UV frequency.

A Rydberg loss spectrum of the $5s45s\,^3S_1$ state in the blue MOT is shown in Fig. 5.5 (c). For this measurement the atom number in the blue MOT is about 2×10^5, and the red and UV intensities are set to about $100\,\mathrm{mW/cm^2}$ and $10\,\mathrm{mW/cm^2}$, respectively. The detuning of the red beam, which addresses the lower transition, is set to zero, and no repumping beam is applied during this experiment. The blue MOT spectrum exhibits two large loss minima with a separation of about 15 MHz.

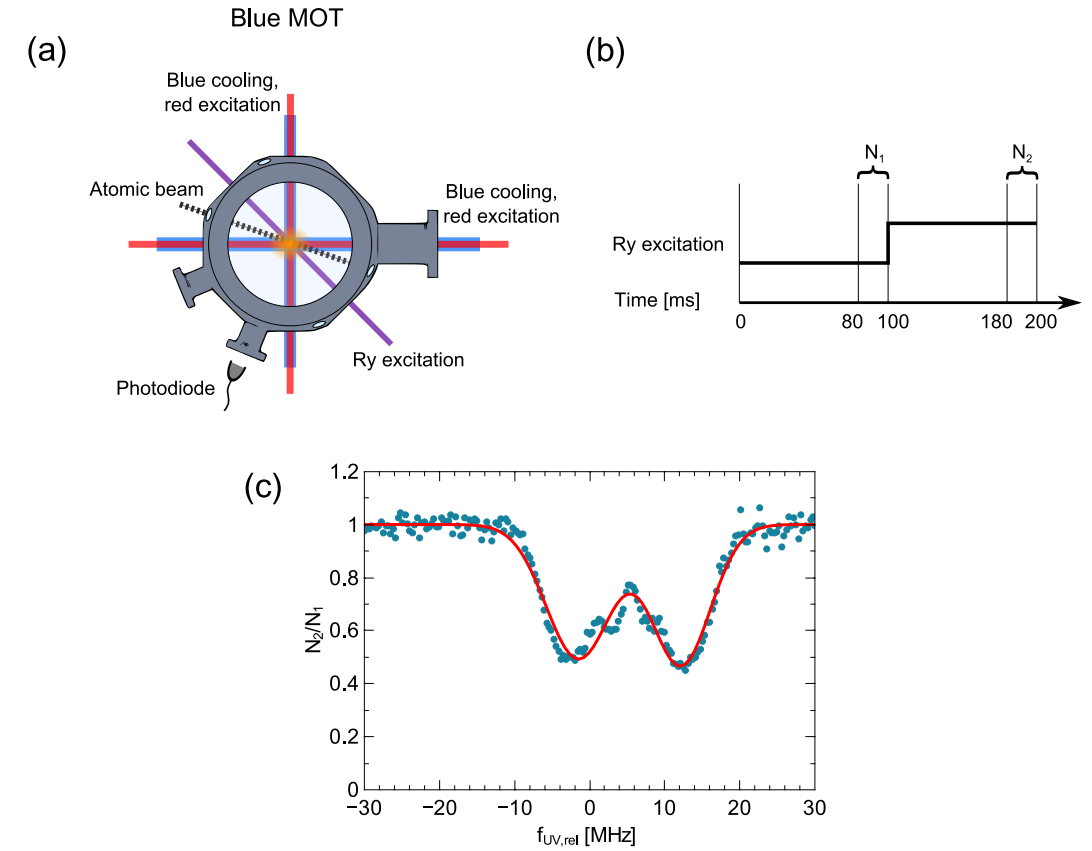

Fig. 5.5 Rydberg excitation in the blue MOT. (a) Top view of the schematic science chamber setup. (b) Experimental sequence. The atom numbers N_1 and N_2 are measured without and with the Rydberg excitation beam in a steady-state blue MOT. (c) Rydberg loss spectrum for the $5s45s\,^3S_1$ state. The experimental data is fitted by two overlapping Gaussians. The zero point of the relative UV frequency $f_{\mathrm{UV,rel}}$ is chosen arbitrarily.

Two overlapping Gaussians are fitted to these loss minima, with full-width-at-half-maximum (FWHM) widths of about 10 MHz. The widths of the individual loss features agree well with the expected width due to Gaussian Zeeman and Doppler broadenings in the blue MOT. For different principal quantum numbers n and Rydberg series different spectrum shapes were observed, with typically two or three clearly distinguishable peaks. Measurements on population transfer in the blue MOT to and from the $5s5p\,^3P_1$ state, in the situations when a near-resonant red beam is suddenly turned on or off with the UV beam being off all the time, indicate that the sub-structure at least partially has its origin in this vee-type sub-system. Overall, the Rydberg excitations in the blue MOT represent a complicated situation with many laser beams and continuous atom loading being involved, and apart from this the Zeeman and the Doppler effects are responsible for a ~ 10 MHz broadening of the lines.

Another aspect is worth noting: An atom loss of around one half can already be seen at low UV intensities of $\sim 10\ \mathrm{mW/cm^2}$. In other words, this coupling to Rydberg states introduces

another loss mechanism in the MOT, which is on the order of the blue MOT one-body loss rate of $\sim 100\,\mathrm{Hz}$. Also loss features of high-n states at $n \sim 90$ can be seen in the blue MOT.

5.2.3. Rydberg excitation in the narrow-line MOT

The experimental setup and sequence for Rydberg loss spectroscopy in the narrowband red MOT are shown in Fig. 5.6 (a) and (b). First the narrowband red MOT is prepared according to the procedures described in Sec. 4.5. 20 ms after the beginning of the red MOT narrowband phase, which corresponds to $t = 0$ in Fig. 5.6 (b), the atoms are imaged on a camera to measure atom number N_1, with the red cooling beams and the magnetic field gradient being on. Then the UV beam is turned on for a variable excitation time τ. The UV excitation time τ is controlled by the UV AOM. [②] 5.8 ms later the red cooling beams and the magnetic field are turned off, and the atoms are imaged again $200\,\mu$s after that to measure atom number N_2.

The resulting Rydberg loss spectrum in the red MOT is shown in Fig. 5.6 (c). The fraction of remaining atoms N_2/N_1 is additionally scaled with the factor κ in order to set it to one if the Rydberg excitation beam is off-resonance. It represents a physically more clean situation than in the blue MOT, due to the much lower Doppler and Zeeman broadening and the absent a.c. light shift of the blue cooling beams. In this measurement the red MOT contains about 2×10^5 atoms, has a horizontal (vertical) $1/e^2$ radius of 750 (100) μm and a peak atomic density of about $2 \times 10^9\,\mathrm{cm}^{-3}$. The average intensity of the six red beams combined is about $100\,\mu\mathrm{W/cm}^2$, and a UV beam with an average intensity of about $800\,\mathrm{mW/cm}^2$ is turned on for an excitation time of 1 ms. In this experiment only a single Rydberg loss feature is visible. A Lorentzian is fitted to the experimental data, with a full-width-at-half-maximum width of $1.02(15)$ MHz. This is somewhat larger than the UV laser linewidth of about 200 kHz and the FWHM Doppler width at the UV wavelength of $\Delta f_\mathrm{D} = 2\sqrt{\ln 2}\, v_\mathrm{mp}/\lambda \simeq 100\,\mathrm{kHz}$ [247], with the most probable velocity $v_\mathrm{mp} = \sqrt{2\,k_B T/m}$ and a typical red MOT temperature of $2\,\mu$K. It is, however, comparable to Zeeman broadening of the $^3\mathrm{P}_1$ state in the cloud along the vertical direction, $\frac{\mu_B}{h}\, g_J(^3\mathrm{P}_1)\, \partial B_z/\partial z \times \Delta z \simeq 1\,\mathrm{MHz}$, with $g_J(^3\mathrm{P}_1) = 1.5$, the magnetic field gradient $\partial B_z/\partial z = 5\,\mathrm{G/cm}$ and the vertical FWHM diameter of the cloud $\Delta z = 100\,\mu\mathrm{m}$.

The level scheme of this experiment is shown in Fig. 5.7 (a). Due to the pancake shape of the narrowband red MOT [for a typical absorption picture of its shape see Fig. 4.11 (b)] there is an offset magnetic field of about $B_z = 300\,\mathrm{mG}$ at its position. Such, the atoms are predominantly excited by σ^--polarized red cooling light shining on the atoms from the bottom,

[②] Additionally to this time, in our experiment, due to the timing of the UV mechanical shutter, there is still residual UV light with a 0.5 % power of the power at turned-on AOM which shines on the atoms for a few 100s of μs before and for a few ms after the set UV exposure time τ.

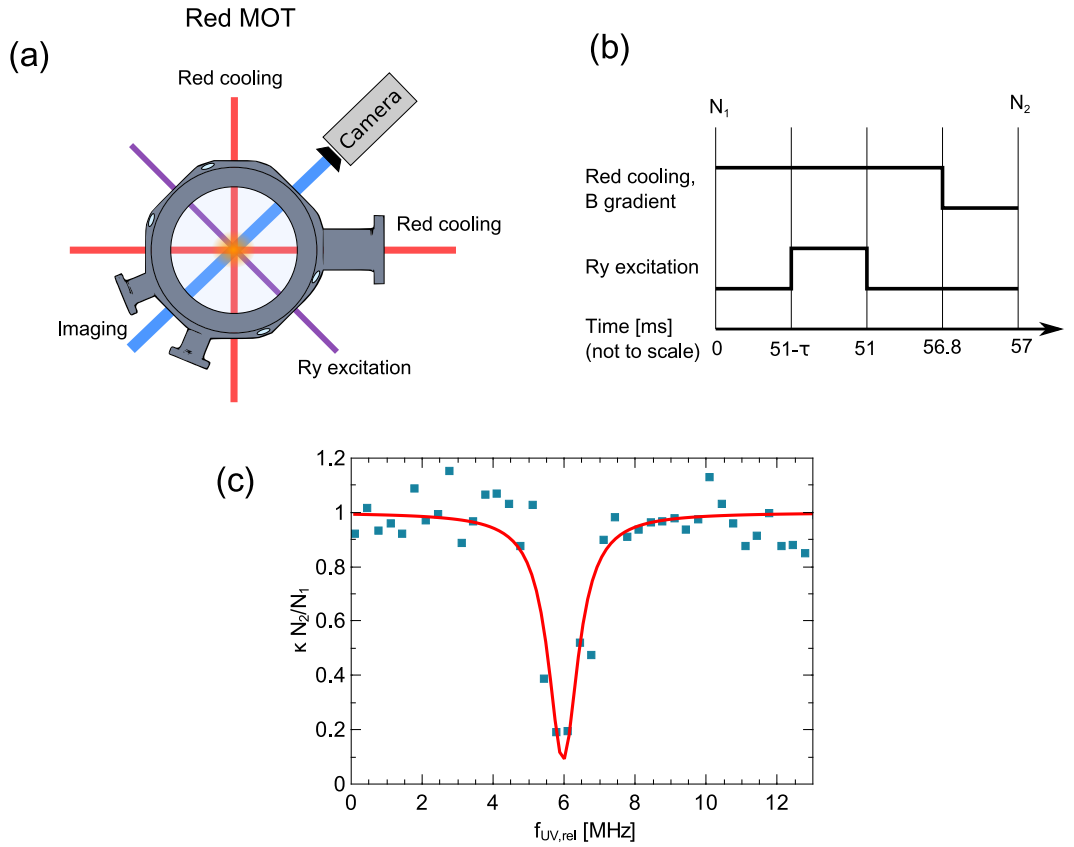

Fig. 5.6 Rydberg excitation in the red MOT. (a) Top view of the schematic science chamber setup. (b) Experimental sequence (time axis not to scale). $t = 0$ corresponds to the time 20 ms after the beginning of the narrowband phase. The atom numbers N_1 and N_2 are measured before and after the Rydberg excitation pulse with variable duration τ. (c) Rydberg loss spectrum for the $5s45s\,^3S_1$ state. The experimental data is fitted by a Lorentzian, with a FWHM width of $1.02(15)$ MHz.

and then by π-polarized UV light. This small offset magnetic field is also expected to result in a small shift of the Rydberg line, $\frac{\mu_B}{h}\,[g_J(^3S_1) - g_J(^3P_1)]\,m_J\,B_z \simeq -200\,\mathrm{kHz}$, with $g_J(^3S_1) = 2$ and $m_J = -1$.

The UV excitation time τ in the red MOT is then varied. Rydberg loss spectra for different excitation times are shown in Fig. 5.7 (b). The loss is clearly visible for excitation times being larger or equal than $300\,\mu$s. For large times, nearly no atoms are left on resonance, and at the same time the Rydberg line broadens. The data for the smallest excitation time $300\,\mu$s can be fitted by a Lorentzian with a width of $0.5(1)$ MHz. For an excitation time of $100\,\mu$s or shorter no unambiguous Rydberg loss is visible in our experiment [not shown in Fig. 5.7 (b)].

The observed loss spectra appear to be largely consistent with the solution of a model based on the optical Bloch equations for our system and our experimental parameters, using the Rydberg state lifetime from Ref. [248] and the dipole matrix element of the $5s5p\,^3P_1(m_J = 1) \rightarrow 5s24s\,^3S_1(m_J = 1)$ transition from the measured Autler-Townes splitting in Ref. [54],

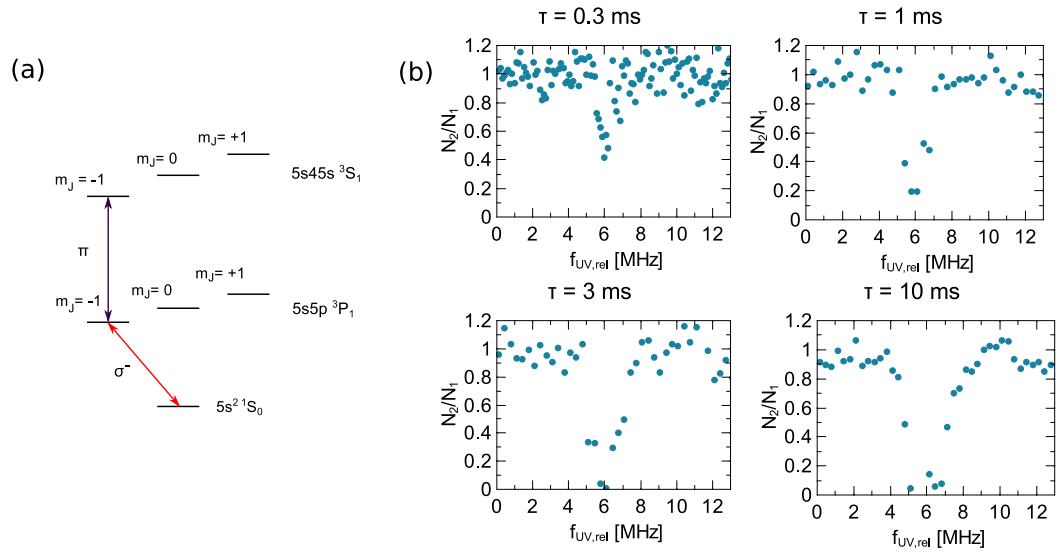

Fig. 5.7 $5s45s\,^3S_1$ loss spectra in the red MOT for different excitation times. (a) Level scheme in the narrowband red MOT. At the position of the atoms in the pancake-shaped red MOT an offset magnetic field is present which defines the quantization axis during the experiment. (b) Experimental results. The loss feature due to Rydberg excitations becomes larger on- and off-resonance for higher excitation times.

both being scaled to our value of $n = 45$ with the general $\propto (n^*)^3$ and $\propto (n^*)^{-3/2}$ scaling laws, respectively. However, no attempt of further data extraction from this measurement, regarding atomic parameters, is undertaken in the framework of this thesis.

In conclusion, we excited strontium atoms to Rydberg states both in the blue and in the red MOTs. We detected the Rydberg states by atom loss spectroscopy. While the loss feature is broadened to a ~ 10 MHz width in the blue MOT, we achieved a ~ 1 MHz loss feature in the red MOT.

Chapter 6 Conclusion and outlook

This thesis described an experimental setup and procedure for the generation of ultracold strontium atoms, as well as first experimental results on subsequent excitations to triplet Rydberg states. The experimental setup comprises the ultra-high vacuum system in which the experiments take place, the magnetic field sources and the laser systems which are used for cooling, repumping and for Rydberg excitation of strontium atoms. The lasers addressing the broad cooling and the repumping transitions of strontium are frequency-stabilized by a wavelength meter [150], with an achieved RMS cooling laser frequency deviation of $2\ \mathrm{MHz}$.

While the laser cooling scheme and findings largely follow established routines of other groups [64], one key innovative component of the setup is a 2D-MOT for strontium atoms [119]. It minimizes black-body radiation and vacuum contamination at the position of the final experiments, as if compared to a Zeeman slower. The 2D-MOT chamber has a low background pressure of $\sim 2 \times 10^{-10}\ \mathrm{mbar}$ at an oven temperature of $465\ ^\circ\mathrm{C}$. A model of the theoretically captured flux of the 2D-MOT is presented, and the flux and divergence of the cold atomic beam emerging from the 2D-MOT are characterized by a TOF method and by fluorescence imaging on a camera. The properties of the cold atomic beam, i.e. its longitudinal velocity distribution and its divergence, are particularly sensitive on the pushing beam intensity. FWHM divergences of the cold atomic beam are between 60 and 40 mrad, dependent on the longitudinal velocity of the cold atomic beam. An auxiliary Zeeman slower beam which makes use of the transverse fringe field of the quadrupolar magnetic field of the 2D-MOT increases the atomic flux by a factor of up to four. Both the increasing and the decreasing field parts of the fringe magnetic field can be used for Zeeman slowing. ^{88}Sr MOT loading rates exceeding $10^9\ \mathrm{s}^{-1}$ are achieved in our setup. The 2D-MOT can serve as a cold atom source of all four stable isotopes of strontium, with both bosonic and fermionic quantum statistics. No saturation of the atomic flux or of the MOT loading rate versus temperature of the strontium oven were noticed up to a maximum temperature of $500\ ^\circ\mathrm{C}$. Prospects for future designs of strontium 2D-MOTs were discussed, for example the addition of heated microtubes in the oven aperture to increase the oven beam collimation. A further miniaturization of the cold atom source seems to be possible, which might be advantageous for satellite-based atomic clock setups which require a low exposure to black-body radiation in the MOT region and for which space and weight are limited.

The setup of the 3D-MOTs operating on the blue broad closed and the red narrow closed transitions of strontium were described. The broadband blue MOT contains up to about 5×10^6

atoms in the absence of a repumping beam, with the dominant loss channel from the MOT being the $5s5p\,^1P_1 \rightarrow 5s4d\,^1D_2 \rightarrow 5s5p\,^3P_2$ decay, and with a temperature of a few mK. If an additional repumping beam at 481 nm addressing the $5s5p\,^3P_2 \rightarrow 5p^2\,^3P_2$ transition is shined on the atoms, the atom number is enhanced by about an order of magnitude. The linewidth of the atom number enhancement in the blue MOT in presence of a continuous repumping beam is found to be power-dependent and can be up to a few 100s of MHz. Additionally, it is shown that $5s5p\,^3P_2$ atoms can be accumulated in a magnetic trap [114]. The lifetime of atoms stored in the magnetic trap is determined by the collision rate with background atoms in our vacuum system and is about 8 s.

In the narrowband red MOT the atoms are then cooled down to temperatures in the low μK regime. In its last phase the red MOT has a pancake shape, as the atoms accumulate on the lower shell of the ellipsoid where the Zeeman shift of the quadrupolar magnetic field equals the cooling beam detuning of the lower beam. In the end of this thesis Rydberg excitation spectra both in the broadband blue and in the narrowband red MOT were shown, by shining an ultraviolet laser beam at 319 nm on the atoms. This is possible by atom loss spectroscopy, due to the decays from the Rydberg state to the long-lived metastable $5s5p\,^3P_{2,0}$ states. While the Rydberg spectra in the blue MOT are Zeeman and Doppler broadened, the Rydberg spectra in the red MOT have a linewidth of ~ 1 MHz for low excitation times of the Rydberg excitation beam. This makes our experiment comparable to other state-of-the-art setups investigating triplet Rydberg states of ultracold strontium atoms [54, 157].

Future experiments in our laboratory will aim for a systematic determination of the energy levels of triplet Rydberg states of strontium, whose literature values still have large uncertainties on the order of a few GHz [207, 249]. With these measurements the determination of more accurate quantum defects would be possible. Also series perturbations, which are especially pronounced for states with $n \approx 15$ for the $^3D_2$ and the $^3D_1$ series of strontium [243], could be studied.

Another possible line of research, which does not rely on atom loss spectroscopy, is to record the absorption or the fluorescence of the lower narrow line in the two-photon $5s^2\,^1S_0 \rightarrow 5s5p\,^3P_1 \rightarrow \mathrm{Ry}$ excitation scheme. This signal is generally very weak due to the small photon scattering rate on that transition. Additionally, for untrapped atoms the lower excitation beam pulse has to be short in order not to accelerate the atoms out of the narrow resonance [250]. Former studies on the fluorescence characteristics of this narrow line [96], which constitutes a pure two-level system, could be pursued with an additional Rydberg coupling beam in the future. In this case already very small a.c. light or Rydberg interaction shifts could shift the atoms out of resonance, which could be used for precise measurements.

A systematic investigation of Rydberg loss spectra in the red MOT, similar to the one presented in Sec. 5.2.3, can certainly be used for the determination of the dipole matrix elements of the $5s5p\,^3P_1 \rightarrow Ry$ transitions and of the Rydberg state lifetimes [248]. An alternative way for the determination of the dipole matrix elements is Autler-Townes spectroscopy [54, 212]. Furthermore it would be insightful to measure from which atomic density and which Rydberg principal quantum number n on Rydberg interactions alter the loss spectrum [54].

Again another line of research is to pursue Rydberg dressing with strontium atoms [54, 227], to use them as quantum simulators for other physical systems. In our three-level system, this could either be done by adiabatically eliminating the intermediate state at large detunings of the lower and the upper laser beams to reduce the system to an effective two-level system [40], or on two-photon resonance with an intermediate state detuning [251, 252]. In both cases the narrow linewidth of the lower transition would increase the ratio of achieved dressed-atom interaction strength over the decoherence rate of the system, as compared to alkali atoms which have broad linewidths of the lower transition [251]. One could even think about single-photon Rydberg dressing from one of the two metastable $^3P_{2,0}$ states to the $^3S_1$ Rydberg series. This would then constitute a two-level system coupling to an isotropically interacting Rydberg state, which does not exist in alkali atoms.

To keep the atoms trapped during shining the Rydberg dressing lasers on them, one could employ an optical lattice at a magic wavelength, that means here with the same a.c. polarizability of the ground and the Rydberg state. For two-electron Rydberg atoms the a.c. polarizabilities at such magic wavelengths are usually larger than in single-electron Rydberg atoms, due to the additional polarizability contribution from the second valence electron [56]. This larger a.c. polarizability allows for deeper potentials at a fixed trapping laser intensity. Magic wavelength trapping in general could also be beneficial to minimize heating and decoherence rates in quantum gates based on Rydberg atoms [52].

In conclusion, we now have an experimental platform available, which allows for the study of ultracold strontium atoms in triplet Rydberg states. The narrow linewidth of the intercombination line, which serves as the lower transition in a two-photon excitation scheme to Rydberg states, leads to an only minimal decoherence during the excitation process and to a high sensitivity. The teaming up of this narrow linewidth with the huge Rydberg interactions could open up a series of experiments on a new level of precision.

Appendix A Supplementary material for Chapter 2

A.1 Properties of the two laser cooling transitions

In Table A.1 a few parameters of interest for the blue broad closed $5s^2\ {}^1S_0 \rightarrow 5s5p\ {}^1P_1$ transition and the red narrow closed $5s^2\ {}^1S_0 \rightarrow 5s5p\ {}^3P_1$ transition of the ^{88}Sr isotope are listed. This isotope has a mass of $m = 88\,u$. The table contains more information than Table 2.2 in Sec. 2.1.3.

All formulas in Table A.1 including their derivations are for example given in Ref. [188]. Only two digits are given for all values which depend on the natural linewidth Γ, as they can change by a few percent due to the uncertainty in Γ. The frequency isotope shifts for the two transitions are on the order of $\sim 100\ \mathrm{MHz/amu}$.

	$5s^2\ {}^1S_0 \rightarrow 5s5p\ {}^1P_1$	$5s^2\ {}^1S_0 \rightarrow 5s5p\ {}^3P_1$
Spectroscopic wave number $\tilde{\nu}$	21 698.462 cm^{-1} [98]	14 504.338 24 cm^{-1}
Angular wave number $k = 2\pi\tilde{\nu}$	$1.363\,35 \times 10^7\ m^{-1}$	$9.113\,344\,493 \times 10^6\ m^{-1}$
Vacuum wavelength $\lambda = 1/\tilde{\nu}$	460.862 nm	689.448 896 8 nm
Frequency $f = c_0/\lambda$	650.504 THz	434.829 121 318 (10) THz [253]
On-resonant absorption cross section $\sigma_0 = 3\lambda^2/2\pi$	$1.014\,11 \times 10^{-13}\ m^2$	$2.269\,580\,275 \times 10^{-13}\ m^2$
Landé g-factor of the excited ${}^{2S+1}L_J$ state $g_J = \frac{3}{2} + \frac{S(S+1)-L(L+1)}{2J(J+1)}$	1	1.5
Natural linewidth $\Gamma/2\pi$	$32.0^{+0.5}_{-0.5}$ MHz [98]	$7.5^{+0.1}_{-0.2}$ kHz [98]
Natural lifetime $\tau = 1/\Gamma$	5.0 ns	21 μs
Maximum acceleration $a_{\max} = \frac{\Gamma}{2}\frac{\hbar k}{m}$	$9.9 \times 10^5\ m/s^2$	$150\ m/s^2$
Saturation intensity $I_{\text{sat}} = \frac{\pi c_0}{\sigma_0}\frac{\hbar\Gamma}{\lambda}$	$43\ mW/cm^2$	$3.0\ \mu W/cm^2$
Dipole matrix element $\mu = \left(\frac{3\epsilon_0\hbar\Gamma\lambda^3}{8\pi^2}\right)^{1/2}$	3.1 ea_0	0.087 ea_0
Velocity which corresponds to a Doppler shift of the natural linewidth $v_\Gamma = \Gamma/k$	15 m/s	5.2 mm/s
Doppler temperature $T_D = \frac{\hbar\Gamma}{2k_B}$	770 μK	0.18 μK
Doppler velocity $v_D = \sqrt{\frac{\hbar\Gamma}{2m}} = v_R\left(\frac{T_D}{T_R}\right)^{1/2}$ (1D rms velocity)	270 mm/s	4.1 mm/s
Recoil temperature $T_R = \frac{\hbar^2k^2}{k_B m}$	1.0 μK	0.46 μK
Recoil velocity $v_R = \frac{\hbar k}{m}$	9.8 mm/s	6.6 mm/s

Table A.1 Extended table of the properties of the two laser cooling transitions for ^{88}Sr. All values in this table are derived from the spectroscopic wave number (blue) or frequency (red) and the natural linewidths (blue and red) of the respective transitions.

A.2 Heating of the Zeeman slower viewport

To avoid strontium coating which would deteriorate its optical transmission properties, the Zeeman slower viewport which is located directly opposite to the strontium oven has to be heated to a high temperature. To get a rough estimate about the required minimum temperature of the viewport, the deposited flux from the oven on the viewport is compared with the evaporated flux from the viewport. In a simple model these two fluxes are given by:

$$\Phi_{\mathrm{depos}} = \frac{1}{4} n_{\mathrm{oven}} \bar{v}_{\mathrm{oven}} A_{\mathrm{oven}} \times \frac{A_{\mathrm{vp}}}{\pi d^2} \,, \tag{A.1a}$$

$$\Phi_{\mathrm{evap}} = \frac{1}{4} n_{\mathrm{vp}} \bar{v}_{\mathrm{vp}} A_{\mathrm{vp}} \,. \tag{A.1b}$$

Hereby $n_i = P_i/k_B T_i$ is the strontium atomic density at pressure P_i and temperature T_i, P_i is the saturated vapor pressure of strontium which is given by $\log_{10}(P_i[\mathrm{mbar}]) = 10.62 - 9450/T_i[\mathrm{K}] - 1.31 \log_{10}(T_i[\mathrm{K}])$ [97], and $\bar{v}_i = (8 k_B T_i/\pi m)^{1/2}$ is the most probable velocity in a Maxwell-Boltzmann distribution. Furthermore, $A_{\mathrm{oven}} = 2\,\mathrm{cm}^2$ is the oven aperture area, $A_{\mathrm{vp}} = 5\,\mathrm{cm}^2$ is the window area (limited by the 1-inch diameter vacuum tube before the viewport), and $d = 42\,\mathrm{cm}$ is the distance between these two areas.

We demand the evaporated flux to be larger than the deposited flux to avoid strontium coating, $\Phi_{\mathrm{evap}} \geqslant \Phi_{\mathrm{depos}}$, from which we calculate a minimum viewport temperature which fulfills this condition. At an oven design temperature of $500\,^\circ\mathrm{C}$ the viewport such has to have a minimum temperature of $\simeq 320\,^\circ\mathrm{C}$. While Eq. (A.1a) for the deposited flux should be quite accurate, Eq. (A.1b) for the evaporated flux has a large uncertainty, as this is the formula for the flux of a gas being in thermal equilibrium with its environment which effuses out from an aperture, and we do not know about the chemical details of strontium deposition and re-emission from the window surface. However, we take this estimate of $320\,^\circ\mathrm{C}$ as the design temperature for the Zeeman slower viewport.

The design of the heating system of the Zeeman slower viewport is shown in Fig. A.1. We use a CF40 sapphire viewport (MDC Vacuum Products) with a maximum specified temperature of $450\,^\circ\mathrm{C}$, limited by the glass-to-metal sealing. [①] A nickel gasket (Lesker, GA-0275NIA) instead of a copper gasket is used at the flange to a full nipple, due to its better temperature resistance. The heating is done by a band heater (Chromalox, 142-053939-020), with maximum sheath temperature $482\,^\circ\mathrm{C}$, which is clamped around the viewport. For temperature insulation reasons, an aluminum cylinder is built around the viewport. It is screwed on two aluminum

[①] In our case sapphire is brazed to the steel type 304L. If a higher temperature is needed, then the sapphire can be brazed to 316LN, which would result in a higher tolerable temperature.

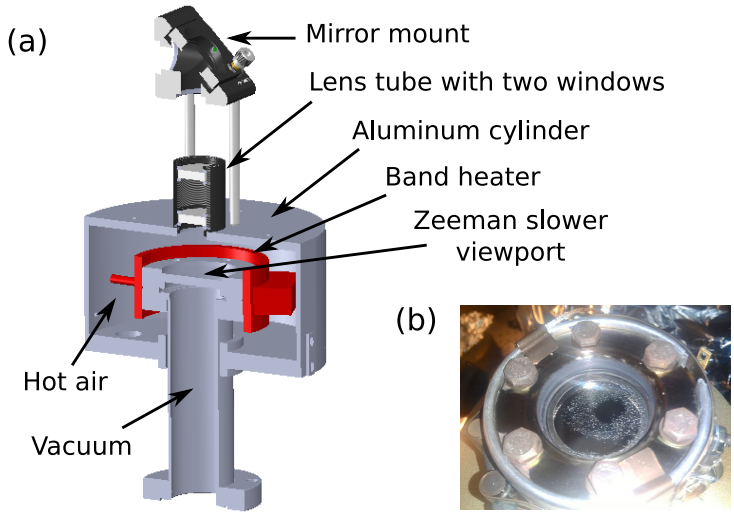

Fig. A.1 Heating of the Zeeman slower viewport. (a) An annotated cut through a model of the vacuum tube and the surrounding heating system. (b) A photo of partial strontium coating of the window surface after about three months of operation.

plates which are clamped around the vacuum tube, with aluminum foil in between. [②] With this design the whole structure is only fixed to the vacuum system, and not directly to the optical table. The latter would not be convenient in our setup as the viewport is located at a height of around 70 cm above the optical table surface. The aluminum cylinder has holes for wires connecting to the band heater and to three thermocouples. We additional put glass wool and aluminum foil around the aluminum cylinder for thermal insulation. The cylinder has a 1-inch internal thread, to which a Thorlabs lens tube made of aluminum with two optically uncoated windows can be attached. It additionally has screw holes to which additional optics can be installed.

The Zeeman slower viewport was first tested and baked in a separate setup. After the first heating the uncoated windows connected to the black anodized lens tube got dirty, but they could be cleaned. After a second bakeout the optical surfaces stayed clean, and the combined transmission of all three windows at 461 nm was measured to be 82 %. The Zeeman slower viewport was then installed to the 2D-MOT chamber in a protective nitrogen atmosphere, and no vacuum degradation in the 2D-MOT chamber due to the heating or the installation of the viewport was noticed.

Partial strontium coating was, however, observed after about three months of operation, when the viewport was examined at room temperature. This coating only seems to have occurred around a spot relatively close to the center, possibly where the Zeeman slower beam was

[②] This design bears the risk that a leak in the full nipple occurs, as the clamping is done at room temperature, and aluminum has a higher temperature expansion coefficient than steel. However, we chose aluminum due to its lower weight, and no problems occurred in our setup.

located. However, no degradation of the flux enhancement of the 2D-MOT due to the additional Zeeman slower beam over time was noticed. Usually, in our setup, the viewport is heated continuously at $\sim 330\,^{\circ}\mathrm{C}$. The maximum temperature which we used was $\sim 350\,^{\circ}\mathrm{C}$. No water or air cooling is used.

A.3 Vacuum system installation

Prior to assembly, the steel pieces were washed in an ultrasonic bath of 99.7% purity ethanol at $50\ ^\circ\mathrm{C}$ for 20 minutes. We first installed the 2D-MOT chamber, with a CF40 full nipple and a CF40 six-way cross after the gate valve, to test our 2D-MOT. The system was baked at $150\ ^\circ\mathrm{C}$ for eleven days, in order to speed up the outgassing and such to reduce the finally attainable pressure at room temperature. This was done in a customized bakeout tent, with a temperature homogeneity of about $5\ ^\circ\mathrm{C}$ across the setup. The pressure evolution in that high-temperature phase is shown in Fig. A.2.

In the end of the $150\ ^\circ\mathrm{C}$ phase the NEG element of the NEXTorr pump was conditioned at $\sim 250\ ^\circ\mathrm{C}$ for one hour, which decreased the pressure by one order of magnitude from $2.4 \times 10^{-7}\ \mathrm{mbar}$ to $2.1 \times 10^{-8}\ \mathrm{mbar}$. After ramping the system down to room temperature, the system pressure was in the low $10^{-10}\ \mathrm{mbar}$ range. The ion pump was flushed, and the NEG element was activated by heating it to $\sim 450\ ^\circ\mathrm{C}$ for one hour, with the ion pump being turned off in order not to saturate it. When the ion gauge was off, the obtained pressure was in the low $10^{-11}\ \mathrm{mbar}$ range, according to the ion pump current.

The system was vented with a buffer gas to atmospheric pressure two times after the initial bakeout: One time when $5\,\mathrm{g}$ of $99.99\,\%$ purity dendritic strontium pieces (Sigma & Aldrich, 441889-5G) were put into the oven, and one time when the initial blank flange opposite to the oven was replaced with the Zeeman slower viewport, whose heating was tested prior in a separate setup. For both used buffer gases argon and nitrogen, each with purity $\geqslant 99.999\,\%$, no harm to the vacuum degree or to the strontium pieces was noticed. New system bakeouts after the vents were such not necessary. When the oven was heated for the first time with strontium inside, the pressure rose up to an oven temperature of $\sim 110\ ^\circ\mathrm{C}$, fell by a factor of two up to $\sim 260\ ^\circ\mathrm{C}$, and then rose again. This partial pressure decrease versus oven temperature is possibly due to getter qualities of strontium. After around one year of operation the pressure in the 2D-MOT chamber is $< 10^{-10}\ \mathrm{mbar}$ if the oven is at room temperature, and $\sim 2 \times 10^{-10}\ \mathrm{mbar}$ if the oven is at the operating temperature of $465\ ^\circ\mathrm{C}$, according to the ion pump current.

Later the science chamber was installed to our system and we baked the entire system at $150\ ^\circ\mathrm{C}$ for another eleven days. However, only a pressure in the low $10^{-9}\ \mathrm{mbar}$ range could be achieved in our science chamber after the bakeout. No external leaks were found, when performing tests with a helium leak detector (Agilent, VS MD302). To find the reason for this relatively high pressure, we performed pressure rise tests by turning off the science chamber ion pump in different situations, see Fig. A.3. If the gate valve to the 2D-MOT chamber was

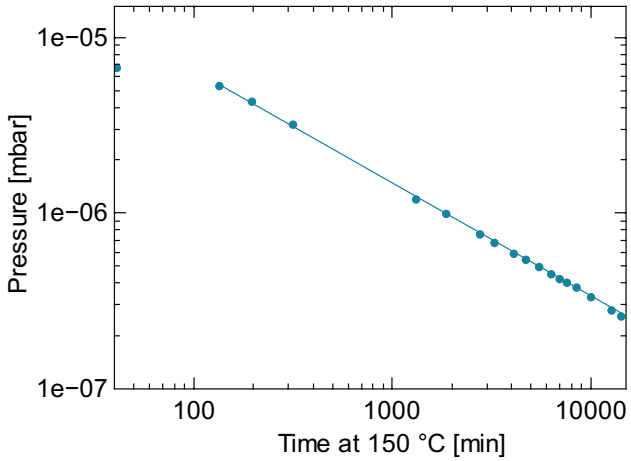

Fig. A.2 Pressure during the 2D-MOT chamber bakeout. The data, except the first data point when the system did not reach thermal equilibrium yet, is fitted with the function $P(t) = P_0 \times t^q$.

closed, the pressure rose at a fast rate of about $10^{-8}\,\mathrm{mbar/min}$. This rate was slightly lower if the gate valve was open and the ion pump in the 2D-MOT chamber was off, certainly because the outpouring gas from the science chamber had to fill a larger volume and thus needed more time for it. If the gate valve was open and the ion pump of the 2D-MOT chamber was running, however, the pressure saturated at a value of about $4 \times 10^{-8}\,\mathrm{mbar}$ after 10 minutes. That strong influence of the ion pump is an indication for the major gas type of that pressure rise being a non-reactive gas, which is solely pumped by the ion pump but not by the continuously pumping NEG element.

This assumption was confirmed by a later measurement with a residual gas analyzer (Stanford Research Systems, RGA200) which was installed to our system. When detecting the gases in our vacuum system, after a pressure rise and when they were released by opening a nearby angle valve, the biggest peak in the residual gas analyzer was found at atomic mass unit (amu) 40, which corresponds to argon (^{40}Ar). The residual gas did not consist of hydrocarbons, which could have resulted from a contamination of the system and would be visible at high amu numbers. If the system has a leak, then gases with the atmospheric composition of 78% nitrogen, 21% oxygen and $\sim 1\%$ argon stream inside. While the first two gases are continuously pumped by the NEG element, argon, which is the third most abundant gas in the atmosphere, can not be pumped anymore if no ion pump is working. As we could not find an external leak, we concluded that we most likely have an internal leak in our system, also called a virtual leak, which is a small constantly outgassing cavity inside the system. According to our pumping rates, system volume and achieved pressures we estimate it to be in the low $10^{-7}\,\mathrm{mbar\,l/s}$ range. [3]

[3] This is the same order of magnitude as the leak rate of an external leak which we orignally found at the position of a welding of the science chamber body to one of its extended CF40 tubes. We shipped our chamber back to

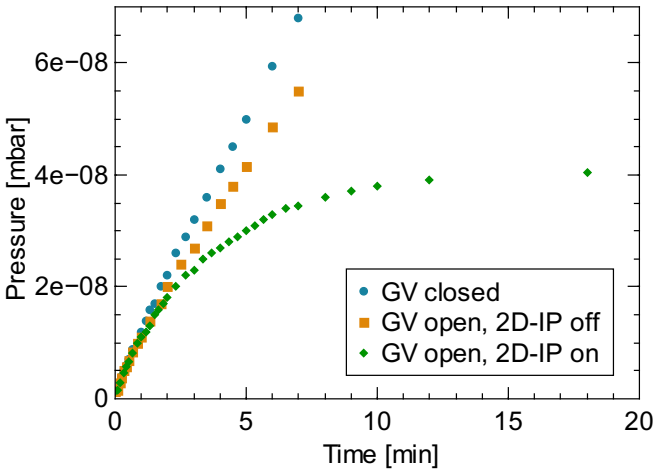

Fig. A.3 Pressure rise tests in the science chamber. Pressure evolutions are shown in different situations after the science chamber ion pump is turned off at $t = 0$. The results indicate the presence of a virtual leak, for details see text. Legend: GV = gate valve, 2D-IP = 2D-MOT chamber ion pump.

During one of our attempts to solve that problem we installed an additional 20 l/s ion pump at our science chamber. However, it only decreased the finally attained pressure by around 30 %.

In conclusion, the pressure in our atom source chamber is about $\sim 2 \times 10^{-10}$ mbar when the strontium oven is on, and the pressure in the science chamber is 1.7×10^{-9} mbar. The latter pressure certainly has that relatively high value because of a virtual leak inside the system.

Kimball Physics, who could not locate a leak, after what we finally agreed on that the chamber should be sent back to us. But when the chamber was washed before the shipment, resealed and again leak tested, Kimball Physics could locate the (external) leak. This was explained by the rare situation that micro-debris got lodged into the problem area, which was dislodged by the ultrasonic bath. After rewelding the tube no external leak was found. However, in the end we can not be sure if the science chamber itself, a viewport or another part in the science chamber region is responsible for our virtual leak.

Appendix B Supplementary material for Chapter 3

B.1 Atomic flux determination by the TOF method

The density of an atomic beam can be determined be measuring its fluorescence when it is subject to an excitation laser beam. The *atomic flux*, however, does not only depend on the atomic density but also on the longitudinal velocity distribution. One method to measure the longitudinal velocity distribution is to turn off the atomic beam at its origin and then to record the time-dependent fluorescence drop in a downstream detection region. The quantitative details of this time-of-flight (TOF) method are shown in the following.

B.1.1. Density and flux

We first look at the case in which all atoms move with the same velocity v_x in x direction through the yz plane, with $n_v(\vec{r})$ the *density of atoms moving at velocity* v_x. Velocity components in other directions are approximated to be negligible. Then the total atomic flux is given by:

$$\Phi_{\mathrm{tot},1v} = v_x \iint \mathrm{d}y\mathrm{d}z\, n_v(\vec{r}) \,. \tag{B.1}$$

We then write the density as $n_v(\vec{r}) = \hat{n}_v\, T(y,z)$, with $\hat{n}_v$ the one-dimensional *line density of atoms moving at velocity* v_x and $T(y,z)$ the normalized transverse distribution, with $\int_{-\infty}^{\infty}\mathrm{d}y \int_{-\infty}^{\infty}\mathrm{d}z\; T(y,z) = 1$. Then the total atomic flux (integrated over the whole radial plane) is simply the product of longitudinal velocity and line density:

$$\Phi_{\mathrm{tot},1v} = v_x\, \hat{n}_v \,. \tag{B.2}$$

We then introduce other longitudinal velocities, with a normalized distribution $f(v_x)$ such that $\int_0^{\infty}\mathrm{d}v_x\, f(v_x) = 1$. We can then write the *line density of atoms moving at all velocities*, or *total line density*, as $\hat{n} = \int_0^{\infty}\mathrm{d}v_x\, f(v_x)\, \hat{n}_v$. The total atomic flux is then given by:

$$\begin{aligned} \Phi_{\mathrm{tot}} &= \int_0^{\infty}\mathrm{d}v_x\, v_x f(v_x)\, \hat{n}_v \\ &= \int_0^{\infty}\mathrm{d}v_x\, \Phi(v_x) \,. \end{aligned} \tag{B.3}$$

In the last step the atomic flux per velocity $\Phi(v_x)$ was introduced, with unit $[\mathrm{m}^{-1}]$ or atoms per second per velocity. We then introduce a time dependence of the line density of atoms moving at velocity v_x in the detection region at $x = \ell$, by $\hat{n}_v(t) = \hat{n}_v\, \Theta(\ell/t - v_x)$. Due to the introduced

Heaviside step function it is larger than zero only for sufficiently small times with $t < \ell/v_x$. Then the total line density can be expressed as:

$$\begin{aligned} \hat{n}(t) &= \int_0^{\ell/t} \mathrm{d}v_x \, f(v_x)\, \hat{n}_v \\ &= \int_\infty^t \mathrm{d}t' \left(-\frac{\ell}{t'^2}\right) f(\ell/t')\, \hat{n}_v \, . \end{aligned} \tag{B.4}$$

In the latter step the substition $t' = \ell/v_x$ was done. We then take the time derivative of the total line density:

$$\begin{aligned} \frac{\mathrm{d}}{\mathrm{d}t}\hat{n}(t) &= -\frac{\ell}{t^2} f(\ell/t)\, \hat{n}_v \\ &= -\frac{v_x^2}{\ell} f(v_x)\, \hat{n}_v \\ &= -\frac{v_x}{\ell}\Phi(v_x) \, . \end{aligned} \tag{B.5}$$

In the first step it was assumed that the primitive becomes zero for $t' \to \infty$, and then the relation $v_x = \ell/t$ was used. Such, after all, we see that the time derivative of the total line density is proportional to the atomic flux per velocity.

B.1.2. Measuring the flux

The geometry of the TOF setup in our experiment is shown in Fig. B.1. An atomic beam has its origin at the point ($x = y = z = 0$), propagates along positive x direction and has a full-width-at-half-maximum (FWHM) diameter of d_{at} at $x = \ell$. It is assumed to have radial symmetry in the yz plane. It is excited by an on-resonant retro-reflected laser beam with $1/e^2$ diameter d_{exc} which propagates along z direction and is centered at ($x = \ell$, $y = 0$). The excitation beam addresses the ${}^1\mathrm{S}_0 \to {}^1\mathrm{P}_1$ transition of strontium, with saturation intensity $I_{\mathrm{sat}} = 43\,\mathrm{mW/cm}^2$ and natural linewidth $\Gamma/2\pi = 32\,\mathrm{MHz}$. The detection volume V of the photodiode is approximated to be a cube with length $2\,a$ being centered around the point ($x = \ell$, $y = 0$, $z = 0$).

The spatially dependent saturation parameter of the atomic transition due to the excitation beam is given by

$$s(x,y) = \frac{I_0}{I_{\mathrm{sat}}} \exp\left(-\frac{2[(x-\ell)^2 + y^2]}{(d_{\mathrm{exc}}/2)^2}\right), \tag{B.6}$$

with $I_0 = 4P/\pi w^2$ the peak intensity of the retro-reflected beam and P the power of a single beam. The total fluorescence power emitted from the atoms in the detection region is given by the convolution of the saturation parameter-dependent scattering rate $\frac{\Gamma}{2}\frac{s}{s+1}$ and the atomic density $n(\vec{r},t)$, multiplied by the photon energy $\hbar\omega$:

$$P(t) = \int_{\ell-a}^{\ell+a} \mathrm{d}x \int_{-a}^{a} \mathrm{d}y \int_{-a}^{a} \mathrm{d}z \, \frac{\Gamma}{2}\frac{s(x,y)}{s(x,y)+1} \hbar\omega \, n(\vec{r},t) \, . \tag{B.7}$$

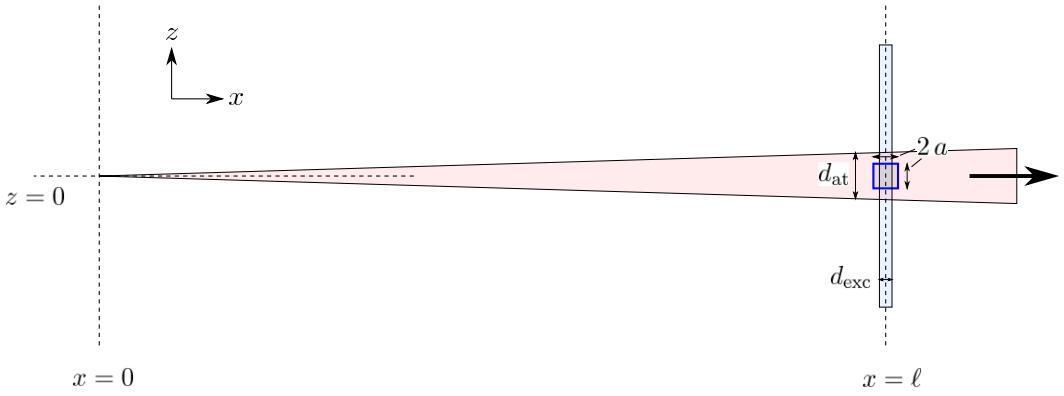

Fig. B.1 TOF setup geometry for the 2D-MOT atomic flux determination. Shown in the xz plane are the cone-shaped atomic beam in red with a FWHM diameter of d_{at} at position $x = \ell$, the cylindrical excitation beam in light blue with $1/e^2$ diameter d_{exc}, and the square detection region with dark blue edges with length $2\,a$. Lengths are to scale for the values in the experiment $\ell = 300\,\mathrm{mm}$, $d_{\mathrm{exc}} = 4.8\,\mathrm{mm}$, $d_{\mathrm{at}} \simeq 18\,\mathrm{mm}$ and $2\,a = 9.4\,\mathrm{mm}$.

The voltage on the oscilloscope is given by $U_{\mathrm{PD}}(t) = \hat{\eta}\,P(t)$, with $\hat{\eta} = L\,\Omega_{\mathrm{pd}}\,F_{\mathrm{dip}}\,\mathcal{R}\,G$. Hereby are the optics loss factor L, the solid angle Ω_{pd}, the enhancement factor due to the dipole radiation pattern F_{dip}, the photodiode responsitivity $\mathcal{R}$ and the gain G. Apart from that the density can be written as $n(\vec{r},t) = \hat{n}(t)\,T(y,z)$. Insertion into Eq. (B.7) gives:

$$\begin{aligned} U_{\mathrm{PD}}(t) &= \frac{\Gamma}{2}\,\hbar\omega\,\hat{\eta}\,\hat{n}(t)\int_{\ell-a}^{\ell+a}\mathrm{d}x\int_{-a}^{a}\mathrm{d}y\int_{-a}^{a}\mathrm{d}z\,\frac{s(x,y)}{s(x,y)+1}\,T(y,z) \\ &\approx \underbrace{\frac{\Gamma}{2}\frac{2I_{\mathrm{av}}/I_{\mathrm{sat}}}{2I_{\mathrm{av}}/I_{\mathrm{sat}}+1}\,\hbar\omega\,\hat{\eta}}_{=1/C_{\mathrm{AB}}}\,d_{\mathrm{exc}}\,\hat{n}(t)\,\underbrace{\int_{-a}^{a}\mathrm{d}y\int_{-a}^{a}\mathrm{d}z\,\frac{s(x=l,y)}{s(x=l,y)+1}\,T(y,z)}_{=g(\theta_{\mathrm{FWHM}})} \\ &= \frac{d_{\mathrm{exc}}}{C_{\mathrm{AB}}}\hat{n}(t)\,g(\theta_{\mathrm{FWHM}})\,. \end{aligned} \tag{B.8}$$

Hereby Eq. (3.1) for the conversion factor of voltage to atom number C_{AB} is used, and the dimensionless factor $g(\theta_{\mathrm{FWHM}})$ is defined, with $g(\theta_{\mathrm{FWHM}}) \leqslant 1$, which describes the overlap of the excitation laser beam intensity with the atomic beam density in the yz plane. It approaches unity if the transverse atomic beam distribution is entirely within the detection region and in the limit of large saturation parameters across the whole beam ($s \to \infty$). In our experiment we approximate $T(y,z)$ by a two-dimensional Gaussian function with radial symmetry:

$$T(y,z) = \frac{1}{2\pi\sigma_r^2}\exp\left(\frac{-(y^2+z^2)}{2\sigma_r^2}\right). \tag{B.9}$$

Then there is the relation $\theta_{\mathrm{FWHM}} = 2\sqrt{2\ln 2}\,\sigma_r/\ell$. For our experimental parameters $g(\theta_{\mathrm{FWHM}}) \approx 1/10$.

By combining Eq. (B.5) and Eq. (B.8), we can solve for the atomic flux per velocity:

$$\Phi(v_x) = \frac{C_{\mathrm{AB}}}{d_{\mathrm{exc}}}\frac{\ell}{v_x}\frac{1}{g(\theta_{\mathrm{FWHM}})}\left(-\frac{\mathrm{d}U_{\mathrm{PD}}(t)}{\mathrm{d}t}\right). \tag{B.10}$$

The total flux, with unit $[\mathrm{s}^{-1}]$, can be obtained by integration over velocity:

$$\Phi_{\mathrm{tot}} = \int_0^\infty \mathrm{d}v_x \, \Phi(v_x) \, . \tag{B.11}$$

This is the total flux encompassing all longitudinal velocities v_x and radial positions r. If we want to know the flux in a certain range of these quantities, i.e. with the conditions $v_x \leqslant v_c$ and $r \leqslant r_c$, then this partial flux can be calculated by only partially integrating the normalized distributions for the longitudinal velocity and the radial position:

$$L = \Phi_{\mathrm{tot}} \int_0^{v_c} \mathrm{d}v_x \, f(v_x) \int_0^{r_c} \mathrm{d}r \, 2\pi r \, T(r, \sigma_r) \, . \tag{B.12}$$

B.2 Model for the 2D-MOT loading rate

To estimate the expected loading rate of the 2D-MOT, the oven flux model of Tiecke *et al.* 2009 [118] is used in the following to describe our oven flux. As a high 2D-MOT loading rate is generally desired, this model can give insights into which parameters of the system have to be changed in order to achieve this.

The total emitted flux from the oven is given by

$$\Phi_{\mathrm{tot}} = \frac{1}{4}\, n_a\, \bar{v}\, A_{\mathrm{oven}}\ , \tag{B.13}$$

where $n_a = P/(k_B T)$ is the atomic density, P is the saturated vapor pressure of solid strontium which is given by $\log_{10}(P[\mathrm{mbar}]) = 10.62 - 9450/T[\mathrm{K}] - 1.31\log_{10}(T[\mathrm{K}])$ [97], $\bar{v} = (8k_B T/\pi\, m)^{1/2}$ with m the mass of an atom is the (3D) mean thermal speed, and $A_{\mathrm{oven}} \simeq 2\ \mathrm{cm}^2$ is the area of the oven aperture. At the oven operating temperature of $465\ ^\circ\mathrm{C}$ this results in a pressure in the oven of about $10^{-6}\,\mathrm{mbar}$, a density of about $10^{10}\ \mathrm{cm}^{-3}$ and a total flux of $2.4\times10^{14}\ \mathrm{s}^{-1}$. The expected oven lifetime when it is continuously heated can be estimated by the formula $\tau_{\mathrm{oven}} = (m_{\mathrm{chunks}}/m_{\mathrm{atom}})\,\Phi_{\mathrm{tot}}^{-1}$, with the mass of the strontium chunks in the oven m_{chunks} and the isotope-averaged mass per atom m_{atom}. It is about five years for our values. Indeed, after operating the oven for one year, during which the oven temperature was ramped down during the nights, no degradation of the atom flux from the 2D-MOT has been noticed.

One possible reason why an emitted atom does not get captured by the 2D-MOT is that it does not hit the trapping region. The normalized angular dependence function of the atomic flux in the half-sphere above the oven follows a cosine law and is given by

$$D(\theta,\phi) = \frac{1}{\pi}\cos\theta\ . \tag{B.14}$$

Hereby is the polar angle (the angle from the aperture normal) $\theta \in [0, \pi/2]$ and the azimuthal angle $\phi \in [0, 2\,\pi]$. In the following we neglect any effects resulting from an atom being emitted from different parts of the oven aperture and assume for simplicity that all atoms are being emitted from its center. Then the capture angles can be approximated as $\theta_c = \tan(w_{\mathrm{cool}}/d_{\mathrm{oven}}) \approx w_{\mathrm{cool}}/d_{\mathrm{oven}}$ as $w_{\mathrm{cool}} \ll d_{\mathrm{oven}}$, with the $1/e^2$ radius of the cooling beam $w_{\mathrm{cool}} = 7.5\,\mathrm{mm}$ and the distance from the oven bottom to the 2D-MOT $d_{\mathrm{oven}} = 145\,\mathrm{mm}$, and $\phi_c = 2\,\pi$. The incident flux on the 2D-MOT trapping region can then be written as:

$$\begin{aligned}\Phi_{\mathrm{inc}} &= \Phi_{\mathrm{tot}} \times \int_0^{\theta_c} \mathrm{d}\theta \sin\theta \int_0^{\phi_c} \mathrm{d}\phi\, D(\theta,\phi) \\ &\approx \Phi_{\mathrm{tot}} \times \left(\frac{w_{\mathrm{cool}}}{d_{\mathrm{oven}}}\right)^2 .\end{aligned} \tag{B.15}$$

Due to geometrical reasons the theoretical incident flux in the 2D-MOT region such is $6.3 \times 10^{11}\ \mathrm{s}^{-1}$, which is only $\simeq 0.3\%$ of the total flux.

Another possible reason why an emitted atom does not get trapped is that it is faster than the capture velocity of the 2D-MOT v_c. The normalized Maxwell-Boltzmann velocity distribution of a 1D beam, with $v \in [0, \infty]$, is given by [247]

$$f_{\mathrm{beam}}(v) = \frac{2}{v_{\mathrm{mp}}^4} v^3 e^{-v^2/v_{mp}^2}\ , \tag{B.16}$$

with the most probable velocity in a 3D gas $v_{\mathrm{mp}} = \sqrt{2k_BT/m}$. It scales with $\propto v^3$, which is contrary to the velocity distribution in a 3D gas which scales with $\propto v^2$ [247]. We introduce the 2D-MOT capture velocity v_c. The captured flux by the 2D-MOT, or in other words the *2D-MOT loading rate*, for the isotope ^{i}Sr, with the abundances a_i being listed in Table 2.1, can then be written as:

$$\begin{aligned} L_{\mathrm{2D}}^i &= a_i \Phi_{\mathrm{inc}} \times \int_0^{v_{c,\mathrm{2D}}} \mathrm{d}v\, f_{\mathrm{beam}}(v) \\ &\approx a_i \Phi_{\mathrm{inc}} \times \frac{1}{2} \left(\frac{v_{c,\mathrm{2D}}}{v_{\mathrm{mp}}} \right)^4 . \end{aligned} \tag{B.17}$$

Or, plugging Eq. (B.13) and Eq. (B.15) into Eq. (B.17), we can write:

$$L_{\mathrm{2D}}^i = a_i \frac{1}{4} n_a\, \bar{v}\, A_{\mathrm{oven}} \times \left(\frac{w_{\mathrm{cool}}}{d_{\mathrm{oven}}} \right)^2 \times \frac{1}{2} \left(\frac{v_{c,\mathrm{2D}}}{v_{\mathrm{mp}}} \right)^4 . \tag{B.18}$$

Here the 2D-MOT capture velocity $v_{c,\mathrm{2D}}$ was defined, and in the last step the approximation $v_{c,\mathrm{2D}} \ll v_{\mathrm{mp}}$ was made. This loading rate scaling to the fourth power of the capture velocity is the same as for VCMOTs [162]. A rough estimate for the capture velocity is [118]

$$v_c \simeq \sqrt{w_{\mathrm{cool}}\, a_{\mathrm{max}} \frac{s}{s+1}}\ , \tag{B.19}$$

with the maximum deceleration $a_{\mathrm{max}} = 9.9 \times 10^5\ \mathrm{m/s^2}$ and the saturation parameter $s = I/I_{\mathrm{sat}}$. Hereby $I = 2P/\pi w_{\mathrm{cool}}^2$ is chosen to be the combined average intensity of the two upper Gaussian cooling beams which slow the hot atoms down, and $I_{\mathrm{sat}} = 43\ \mathrm{mW/cm^2}$ is the saturation intensity. For a typical cooling beam power of 40 mW we obtain a capture velocity of $62\ \mathrm{m/s}$. According to Eq. (B.18) the ^{88}Sr 2D-MOT loading rate is then $2.0 \times 10^8\ \mathrm{s}^{-1}$, which is $\simeq 300$ ppm of the incident flux and $\simeq 1$ ppm of the total flux. While it has to be kept in mind that the saturated vapor pressure of strontium is subject to a large uncertainty (see Sec. 2.1.1), this oven flux model gives an estimate on the 2D-MOT loading rate and its dependencies on geometrical and other parameters.

Bibliography

[1] Richard P Feynman. Simulating Physics with Computers. *Int. J. Theor. Phys.*, 21(6-7):467–488, 1982.

[2] I. M. Georgescu, S. Ashhab, and Franco Nori. Quantum simulation. *Rev. Mod. Phys.*, 86:153–185, Mar 2014.

[3] Immanuel Bloch, Jean Dalibard, and Wilhelm Zwerger. Many-body physics with ultracold gases. *Rev. Mod. Phys.*, 80:885–964, Jul 2008.

[4] Immanuel Bloch, Jean Dalibard, and Sylvain Nascimbene. Quantum simulations with ultracold quantum gases. *Nat. Phys.*, 8(4):267, 2012.

[5] Harold J Metcalf and Peter Van der Straten. *Laser cooling and trapping of neutral atoms*. Wiley Online Library, 2007.

[6] Theodor W Hänsch and Arthur L Schawlow. Cooling of gases by laser radiation. *Opt. Commun.*, 13(1):68–69, 1975.

[7] William D Phillips and Harold Metcalf. Laser deceleration of an atomic beam. *Phys. Rev. Lett.*, 48(9):596, 1982.

[8] Steven Chu. Nobel Lecture: The manipulation of neutral particles. *Rev. Mod. Phys.*, 70(3):685, 1998.

[9] Claude N Cohen-Tannoudji. Nobel Lecture: Manipulating atoms with photons. *Rev. Mod. Phys.*, 70(3):707, 1998.

[10] William D Phillips. Nobel Lecture: Laser cooling and trapping of neutral atoms. *Rev. Mod. Phys.*, 70(3):721, 1998.

[11] K Dieckmann, RJC Spreeuw, M Weidemüller, and JTM Walraven. Two-dimensional magneto-optical trap as a source of slow atoms. *Phys. Rev. A*, 58(5):3891, 1998.

[12] Shayne Bennetts, Chun-Chia Chen, Benjamin Pasquiou, and Florian Schreck. Steady-State Magneto-Optical Trap with 100-Fold Improved Phase-Space Density. *Phys. Rev. Lett.*, 119(22):223202, 2017.

[13] K. Honda, Y. Takahashi, T. Kuwamoto, M. Fujimoto, K. Toyoda, K. Ishikawa, and T. Yabuzaki. Magneto-optical trapping of Yb atoms and a limit on the branching ratio of the $^1P_1$ state. *Phys. Rev. A*, 59:R934–R937, Feb 1999.

[14] Fujio Shimizu, Kazuko Shimizu, and Hiroshi Takuma. Laser cooling and trapping of Ne metastable atoms. *Phys. Rev. A*, 39:2758–2760, Mar 1989.

[15] Mike H Anderson, Jason R Ensher, Michael R Matthews, Carl E Wieman, and Eric A Cornell. Observation of Bose-Einstein condensation in a dilute atomic vapor. *Science*, 269(5221):198–

201, 1995.

[16] Cl C Bradley, CA Sackett, JJ Tollett, and Randall G Hulet. Evidence of Bose-Einstein condensation in an atomic gas with attractive interactions. *Phys. Rev. Lett.*, 75(9):1687, 1995.

[17] Kendall B Davis, M-O Mewes, Michael R Andrews, NJ Van Druten, DS Durfee, DM Kurn, and Wolfgang Ketterle. Bose-Einstein condensation in a gas of sodium atoms. *Phys. Rev. Lett.*, 75(22):3969, 1995.

[18] Brian DeMarco and Deborah S Jin. Onset of Fermi degeneracy in a trapped atomic gas. *Science*, 285(5434):1703–1706, 1999.

[19] Cheng Chin, Rudolf Grimm, Paul Julienne, and Eite Tiesinga. Feshbach resonances in ultracold gases. *Rev. Mod. Phys.*, 82(2):1225, 2010.

[20] Stefan Kuhr. Quantum-gas microscopes: a new tool for cold-atom quantum simulators. *Natl. Sci. Rev.*, 3(2):170–172, 2016.

[21] H. Weimer, M. Müller, I. Lesanovsky, P. Zoller, and H. P. Büchler. A Rydberg quantum simulator. *Nat. Phys.*, 6:382, 2010.

[22] H. Weimer, M. Müller, H. Büchler, and I. Lesanovsky. Digital quantum simulation with Rydberg atoms. *Quantum Inf. Process.*, 10:885–906, 2011. 10.1007/s11128-011-0303-5.

[23] Thomas F Gallagher. *Rydberg atoms*, volume 3. Cambridge University Press, 2005.

[24] Thomas F. Gallagher and Pierre Pillet. Dipole-Dipole Interactions of Rydberg Atoms. In P.R. Berman E. Arimondo and C.C. Lin, editors, *Advances in Atomic, Molecular, and Optical Physics*, volume 56, pages 161–218. Academic Press, 2008.

[25] Daniel Comparat and Pierre Pillet. Dipole blockade in a cold Rydberg atomic sample. *J. Opt. Soc. Am. B*, 27(6):A208–A232, 2010.

[26] D. Jaksch, J. I. Cirac, P. Zoller, S. L. Rolston, R. Côté, and M. D. Lukin. Fast Quantum Gates for Neutral Atoms. *Phys. Rev. Lett.*, 85:2208, 2000.

[27] M. D. Lukin, M. Fleischhauer, R. Côté, L. M. Duan, D. Jaksch, J. I. Cirac, and P. Zoller. Dipole Blockade and Quantum Information Processing in Mesoscopic Atomic Ensembles. *Phys. Rev. Lett.*, 87:037901, 2001.

[28] D. Tong, S. M. Farooqi, J. Stanojevic, S. Krishnan, Y. P. Zhang, R. Côté, E. E. Eyler, and P. L. Gould. Local Blockade of Rydberg Excitation in an Ultracold Gas. *Phys. Rev. Lett.*, 93:063001, 2004.

[29] Kilian Singer, Markus Reetz-Lamour, Thomas Amthor, Luis Gustavo Marcassa, and Matthias Weidemüller. Suppression of Excitation and Spectral Broadening Induced by Interactions in a Cold Gas of Rydberg Atoms. *Phys. Rev. Lett.*, 93:163001, 2004.

[30] Peter Schauß, Marc Cheneau, Manuel Endres, Takeshi Fukuhara, Sebastian Hild, Ahmed Omran, Thomas Pohl, Christian Gross, Stefan Kuhr, and Immanuel Bloch. Observation of

spatially ordered structures in a two-dimensional Rydberg gas. *Nature*, 491(7422):87–91, November 2012.

[31] Peter Schauß, Johannes Zeiher, Takeshi Fukuhara, S Hild, M Cheneau, T Macrì, T Pohl, Immanuel Bloch, and Christian Groß. Crystallization in Ising quantum magnets. *Science*, 347(6229):1455–1458, 2015.

[32] F. Nogrette, H. Labuhn, S. Ravets, D. Barredo, L. Béguin, A. Vernier, T. Lahaye, and A. Browaeys. Single-Atom Trapping in Holographic 2D Arrays of Microtraps with Arbitrary Geometries. *Phys. Rev. X*, 4:021034, May 2014.

[33] Lucas Béguin. *Measurement of the van der Waals interaction between two Rydberg atoms*. PhD thesis, Institut d'Optique Graduate School, 2013.

[34] Sylvain Ravets, Henning Labuhn, Daniel Barredo, Lucas Béguin, Thierry Lahaye, and Antoine Browaeys. Coherent dipole–dipole coupling between two single Rydberg atoms at an electrically-tuned Förster resonance. *Nat. Phys.*, 10(12):914, 2014.

[35] Sylvain Ravets, Henning Labuhn, Daniel Barredo, Thierry Lahaye, and Antoine Browaeys. Measurement of the angular dependence of the dipole-dipole interaction between two individual Rydberg atoms at a Förster resonance. *Phys. Rev. A*, 92(2):020701, 2015.

[36] Daniel Barredo, Henning Labuhn, Sylvain Ravets, Thierry Lahaye, Antoine Browaeys, and Charles S. Adams. Coherent Excitation Transfer in a Spin Chain of Three Rydberg Atoms. *Phys. Rev. Lett.*, 114:113002, Mar 2015.

[37] Henning Labuhn, Daniel Barredo, Sylvain Ravets, Sylvain De Léséleuc, Tommaso Macrì, Thierry Lahaye, and Antoine Browaeys. Tunable two-dimensional arrays of single Rydberg atoms for realizing quantum Ising models. *Nature*, 534(7609):667, 2016.

[38] N. Henkel, R. Nath, and T. Pohl. Three-Dimensional Roton Excitations and Supersolid Formation in Rydberg-Excited Bose-Einstein Condensates. *Phys. Rev. Lett.*, 104:195302, May 2010.

[39] G. Pupillo, A. Micheli, M. Boninsegni, I. Lesanovsky, and P. Zoller. Strongly Correlated Gases of Rydberg-Dressed Atoms: Quantum and Classical Dynamics. *Phys. Rev. Lett.*, 104:223002, 2010.

[40] Jens Honer, Hendrik Weimer, Tilman Pfau, and Hans Peter Büchler. Collective Many-Body Interaction in Rydberg Dressed Atoms. *Phys. Rev. Lett.*, 105(16):160404–, October 2010.

[41] J. E. Johnson and S. L. Rolston. Interactions between Rydberg-dressed atoms. *Phys. Rev. A*, 82(3):033412, September 2010.

[42] Y-Y Jau, AM Hankin, T Keating, IH Deutsch, and GW Biedermann. Entangling atomic spins with a Rydberg-dressed spin-flip blockade. *Nat. Phys.*, 12(1):71–74, 2016.

[43] Johannes Zeiher, Rick Van Bijnen, Peter Schauß, Sebastian Hild, Jae-yoon Choi, Thomas

Pohl, Immanuel Bloch, and Christian Gross. Many-body interferometry of a Rydberg-dressed spin lattice. *Nat. Phys.*, 12(12):1095, 2016.

[44] Johannes Zeiher, Jae-yoon Choi, Antonio Rubio-Abadal, Thomas Pohl, Rick van Bijnen, Immanuel Bloch, and Christian Gross. Coherent Many-Body Spin Dynamics in a Long-Range Interacting Ising Chain. *Phys. Rev. X*, 7:041063, Dec 2017.

[45] Jonathan D Pritchard, Kevin J Weatherill, and Charles S Adams. Nonlinear optics using cold Rydberg atoms. In *Annual Review of Cold Atoms and Molecules: Volume 1*, pages 301–350. World Scientific, 2013.

[46] C Murray and Thomas Pohl. Quantum and nonlinear optics in strongly interacting atomic ensembles. In *Advances In Atomic, Molecular, and Optical Physics*, volume 65, pages 321–372. Elsevier, 2016.

[47] Ofer Firstenberg, Charles S Adams, and Sebastian Hofferberth. Nonlinear quantum optics mediated by Rydberg interactions. *J. Phys. B: At., Mol. Opt. Phys.*, 49(15):152003, 2016.

[48] G. Günter, H. Schempp, M. Robert-de Saint-Vincent, V. Gavryusev, S. Helmrich, C. S. Hofmann, S. Whitlock, and M. Weidemüller. Observing the Dynamics of Dipole-Mediated Energy Transport by Interaction-Enhanced Imaging. *Science*, 342(6161):954–956, 2013.

[49] Y. O. Dudin and A. Kuzmich. Strongly Interacting Rydberg Excitations of a Cold Atomic Gas. *Science*, 336:887 – 889, 2012.

[50] TM Weber, M Höning, T Niederprüm, T Manthey, O Thomas, V Guarrera, M Fleischhauer, G Barontini, and H Ott. Mesoscopic Rydberg-blockaded ensembles in the superatom regime and beyond. *Nat. Phys.*, 11:157–161, 2015.

[51] Mark Saffman, Thad G Walker, and Klaus Mølmer. Quantum information with Rydberg atoms. *Rev. Mod. Phys.*, 82(3):2313, 2010.

[52] Mark Saffman. Quantum computing with atomic qubits and Rydberg interactions: progress and challenges. *J. Phys. B: At., Mol. Opt. Phys.*, 49(20):202001, 2016.

[53] J Millen, G Lochead, and MPA Jones. Two-electron excitation of an interacting cold Rydberg gas. *Phys. Rev. Lett.*, 105(21):213004, 2010.

[54] BJ DeSalvo, JA Aman, C Gaul, T Pohl, S Yoshida, J Burgdörfer, KRA Hazzard, FB Dunning, and TC Killian. Rydberg-blockade effects in Autler-Townes spectra of ultracold strontium. *Phys. Rev. A*, 93(2):022709, 2016.

[55] FB Dunning, TC Killian, S Yoshida, and J Burgdörfer. Recent advances in Rydberg physics using alkaline-earth atoms. *J. Phys. B: At., Mol. Opt. Phys.*, 49(11):112003, 2016.

[56] R Mukherjee, J Millen, R Nath, M P A Jones, and T Pohl. Many-body physics with alkaline-earth Rydberg lattices. *J. Phys. B: At., Mol. Opt. Phys.*, 44(18):184010, 2011.

[57] G Lochead, D Boddy, DP Sadler, CS Adams, and MPA Jones. Number-resolved imaging of

excited-state atoms using a scanning autoionization microscope. *Phys. Rev. A*, 87(5):053409, 2013.

[58] P. McQuillen, X. Zhang, T. Strickler, F. B. Dunning, and T. C. Killian. Imaging the evolution of an ultracold strontium Rydberg gas. *Phys. Rev. A*, 87:013407, Jan 2013.

[59] Mireille Aymar, Chris H Greene, and Eliane Luc-Koenig. Multichannel Rydberg spectroscopy of complex atoms. *Rev. Mod. Phys.*, 68(4):1015, 1996.

[60] Andrew J Daley, Martin M Boyd, Jun Ye, and Peter Zoller. Quantum computing with alkaline-earth-metal atoms. *Phys. Rev. Lett.*, 101(17):170504, 2008.

[61] Michael Hermele, Victor Gurarie, and Ana Maria Rey. Mott Insulators of Ultracold Fermionic Alkaline Earth Atoms: Underconstrained Magnetism and Chiral Spin Liquid. *Phys. Rev. Lett.*, 103:135301, Sep 2009.

[62] A V Gorshkov, A M Rey, A J Daley, M M Boyd, J Ye, P Zoller, and M D Lukin. Alkaline-Earth-Metal Atoms as Few-Qubit Quantum Registers. *Phys. Rev. Lett.*, 102:110503, Mar 2009.

[63] A V Gorshkov, M Hermele, V Gurarie, C Xu, P S Julienne, J Ye, P Zoller, E Demler, M D Lukin, and A M Rey. Two-orbital SU (N) magnetism with ultracold alkaline-earth atoms. *Nat. Phys.*, 6(4):289, 2010.

[64] Simon Stellmer, Florian Schreck, and Thomas C Killian. Degenerate quantum gases of strontium. *Annual Review of Cold Atoms and Molecules*, 2:1–80, 2014.

[65] F Sorrentino, G Ferrari, N Poli, R Drullinger, and GM Tino. Laser cooling and trapping of atomic strontium for ultracold atoms physics, high-precision spectroscopy and quantum sensors. *Mod. Phys. Lett. B*, 20(21):1287–1320, 2006.

[66] Takayuki Kurosu and Fujio Shimizu. Laser cooling and trapping of calcium and strontium. *Jpn. J. Appl. Phys.*, 29(11A):L2127, 1990.

[67] EL Raab, M Prentiss, Alex Cable, Steven Chu, and David E Pritchard. Trapping of neutral sodium atoms with radiation pressure. *Phys. Rev. Lett.*, 59(23):2631, 1987.

[68] Hidetoshi Katori, Tetsuya Ido, Yoshitomo Isoya, and Makoto Kuwata-Gonokami. Magneto-optical trapping and cooling of strontium atoms down to the photon recoil temperature. *Phys. Rev. Lett.*, 82(6):1116, 1999.

[69] Kurt R Vogel, Timothy P Dinneen, Alan Gallagher, and John L Hall. Narrow-line Doppler cooling of strontium to the recoil limit. *IEEE Trans. Instrum. Meas.*, 48(2):618–621, 1999.

[70] Tetsuya Ido, Yoshitomo Isoya, and Hidetoshi Katori. Optical-dipole trapping of Sr atoms at a high phase-space density. *Phys. Rev. A*, 61(6):061403, 2000.

[71] Thomas H Loftus, Tetsuya Ido, Andrew D Ludlow, Martin M Boyd, and Jun Ye. Narrow line cooling: finite photon recoil dynamics. *Phys. Rev. Lett.*, 93(7):073003, 2004.

[72] Thomas H Loftus, Tetsuya Ido, Martin M Boyd, Andrew D Ludlow, and Jun Ye. Narrow line cooling and momentum-space crystals. *Phys. Rev. A*, 70(6):063413, 2004.

[73] Simon Stellmer, Meng Khoon Tey, Bo Huang, Rudolf Grimm, and Florian Schreck. Bose-Einstein condensation of strontium. *Phys. Rev. Lett.*, 103(20):200401, 2009.

[74] Y. N. Martinez De Escobar, P. G. Mickelson, M. Yan, B. J. DeSalvo, S. B. Nagel, and T. C. Killian. Bose-Einstein Condensation of ^{84}Sr. *Phys. Rev. Lett.*, 103(20):200402, 2009.

[75] Yosuke Takasu, Kenichi Maki, Kaduki Komori, Tetsushi Takano, Kazuhito Honda, Mitsutaka Kumakura, Tsutomu Yabuzaki, and Yoshiro Takahashi. Spin-singlet Bose-Einstein condensation of two-electron atoms. *Phys. Rev. Lett.*, 91(4):040404, 2003.

[76] Sebastian Kraft, Felix Vogt, Oliver Appel, Fritz Riehle, and Uwe Sterr. Bose-Einstein Condensation of Alkaline Earth Atoms: ^{40}Ca. *Phys. Rev. Lett.*, 103(13):130401, 2009.

[77] Simon Stellmer, Meng Khoon Tey, Rudolf Grimm, and Florian Schreck. Bose-Einstein condensation of ^{86}Sr. *Phys. Rev. A*, 82(4):041602, 2010.

[78] Pascal Gerry Mickelson, YN Martinez De Escobar, M Yan, BJ DeSalvo, and Thomas C Killian. Bose-Einstein condensation of ^{88}Sr through sympathetic cooling with ^{87}Sr. *Phys. Rev. A*, 81(5):051601, 2010.

[79] Brian J DeSalvo, Mi Yan, Pascal Gerry Mickelson, YN Martinez De Escobar, and Thomas C Killian. Degenerate Fermi Gas of ^{87}Sr. *Phys. Rev. Lett.*, 105(3):030402, 2010.

[80] Meng Khoon Tey, Simon Stellmer, Rudolf Grimm, and Florian Schreck. Double-degenerate Bose-Fermi mixture of strontium. *Phys. Rev. A*, 82(1):011608, 2010.

[81] Simon Stellmer, Rudolf Grimm, and Florian Schreck. Production of quantum-degenerate strontium gases. *Phys. Rev. A*, 87(1):013611, 2013.

[82] Simon Stellmer, Benjamin Pasquiou, Rudolf Grimm, and Florian Schreck. Laser cooling to quantum degeneracy. *Phys. Rev. Lett.*, 110(26):263003, 2013.

[83] BJ Bloom, TL Nicholson, JR Williams, SL Campbell, M Bishof, X Zhang, W Zhang, SL Bromley, and J Ye. An optical lattice clock with accuracy and stability at the 10^{-18} level. *Nature*, 506(7486):71–75, 2014.

[84] Stephan Falke, Nathan Lemke, Christian Grebing, Burghard Lipphardt, Stefan Weyers, Vladislav Gerginov, Nils Huntemann, Christian Hagemann, Ali Al-Masoudi, Sebastian Häfner, et al. A strontium lattice clock with 3×10^{-17} inaccuracy and its frequency. *New J. Phys.*, 16(7):073023, 2014.

[85] Ichiro Ushijima, Masao Takamoto, Manoj Das, Takuya Ohkubo, and Hidetoshi Katori. Cryogenic optical lattice clocks. *Nat. Photonics*, 9(3):185, 2015.

[86] Sara L Campbell, RB Hutson, GE Marti, A Goban, N Darkwah Oppong, RL McNally, L Sonderhouse, JM Robinson, W Zhang, BJ Bloom, et al. A Fermi-degenerate three-dimensional

optical lattice clock. *Science*, 358(6359):90–94, 2017.

[87] Andrew D Ludlow, Martin M Boyd, Jun Ye, Ekkehard Peik, and Piet O Schmidt. Optical atomic clocks. *Rev. Mod. Phys.*, 87(2):637, 2015.

[88] Tanja E Mehlstäubler, Gesine Grosche, Christian Lisdat, Piet O Schmidt, and Heiner Denker. Atomic clocks for geodesy. *Rep. Prog. Phys.*, 81(6):064401, 2018.

[89] Benjamin M Roberts, Geoffrey Blewitt, Conner Dailey, Mac Murphy, Maxim Pospelov, Alex Rollings, Jeff Sherman, Wyatt Williams, and Andrei Derevianko. Search for domain wall dark matter with atomic clocks on board global positioning system satellites. *Nat. Commun.*, 8(1):1195, 2017.

[90] Matthew A Norcia, Julia RK Cline, and James K Thompson. Role of atoms in atomic gravitational-wave detectors. *Phys. Rev. A*, 96(4):042118, 2017.

[91] Vincent Barbé, Alessio Ciamei, Benjamin Pasquiou, Lukas Reichsöllner, Florian Schreck, Piotr S Żuchowski, and Jeremy M Hutson. Observation of Feshbach resonances between alkali and closed-shell atoms. *arXiv preprint arXiv:1710.03093*, 2017.

[92] BH McGuyer, M McDonald, GZ Iwata, MG Tarallo, W Skomorowski, R Moszynski, and T Zelevinsky. Precise study of asymptotic physics with subradiant ultracold molecules. *Nat. Phys.*, 11(1):32, 2015.

[93] Alessio Ciamei, Alex Bayerle, Chun-Chia Chen, Benjamin Pasquiou, and Florian Schreck. Efficient production of long-lived ultracold Sr_2 molecules. *Phys. Rev. A*, 96(1):013406, 2017.

[94] N Poli, F-Y Wang, MG Tarallo, A Alberti, M Prevedelli, and GM Tino. Precision measurement of gravity with cold atoms in an optical lattice and comparison with a classical gravimeter. *Phys. Rev. Lett.*, 106(3):038501, 2011.

[95] Y Bidel, B Klappauf, JC Bernard, Dominique Delande, Guillaume Labeyrie, Christian Miniatura, D Wilkowski, and Robin Kaiser. Coherent light transport in a cold strontium cloud. *Phys. Rev. Lett.*, 88(20):203902, 2002.

[96] Sarah L Bromley, Bihui Zhu, Michael Bishof, Xibo Zhang, Tobias Bothwell, Johannes Schachenmayer, Travis L Nicholson, Robin Kaiser, Susanne F Yelin, Mikhail D Lukin, et al. Collective atomic scattering and motional effects in a dense coherent medium. *Nat. Commun.*, 7:11039, 2016.

[97] Simon Stellmer. *Degenerate quantum gases of strontium*. PhD thesis, University of Innsbruck, 2013.

[98] JE Sansonetti and G Nave. Wavelengths, transition probabilities, and energy levels for the spectrum of neutral strontium (Sr I). *J. Phys. Chem. Ref. Data*, 39(3):033103, 2010.

[99] N Poli, RE Drullinger, G Ferrari, J Léonard, F Sorrentino, and GM Tino. Cooling and trapping of ultracold strontium isotopic mixtures. *Phys. Rev. A*, 71(6):061403, 2005.

[100] Kurt Richard Vogel. *Laser cooling on a narrow atomic transition and measurement of the two-body cold collision loss rate in a strontium magneto-optical trap*. PhD thesis, University of Colorado at Boulder, 1999.

[101] CB Alcock, VP Itkin, and MK Horrigan. Vapour pressure equations for the metallic elements: 298–2500K. *Can. Metall. Q.*, 23(3):309–313, 1984.

[102] Marco Schioppo, Nicola Poli, Marco Prevedelli, St Falke, Ch Lisdat, Uwe Sterr, and Guglielmo Maria Tino. A compact and efficient strontium oven for laser-cooling experiments. *Rev. Sci. Instrum.*, 83(10):103101, 2012.

[103] Timothy P Dinneen, Kurt R Vogel, Ennio Arimondo, John L Hall, and Alan Gallagher. Cold collisions of Sr*- Sr in a magneto-optical trap. *Phys. Rev. A*, 59(2):1216, 1999.

[104] I Courtillot, A Quessada, RP Kovacich, JJ Zondy, A Landragin, A Clairon, and P Lemonde. Efficient cooling and trapping of strontium atoms. *Opt. Lett.*, 28(6):468–470, 2003.

[105] Daniel A Steck. Rubidium 87 D line data, 2001.

[106] Xinye Xu, Thomas H Loftus, John L Hall, Alan Gallagher, and Jun Ye. Cooling and trapping of atomic strontium. *J. Opt. Soc. Am. B*, 20(5):968–976, 2003.

[107] LR Hunter, WA Walker, and DS Weiss. Observation of an atomic Stark–electric-quadrupole interference. *Phys. Rev. Lett.*, 56(8):823, 1986.

[108] Charles W Bauschlicher Jr, Stephen R Langhoff, and Harry Partridge. The radiative lifetime of the ^{1}D$_2$ state of Ca and Sr: a core-valence treatment. *J. Phys. B: At., Mol. Opt. Phys.*, 18(8):1523, 1985.

[109] Simon Stellmer and Florian Schreck. Reservoir spectroscopy of $5s5p\ ^3P_2$–$5snd\ ^3D_{1,2,3}$ transitions in strontium. *Phys. Rev. A*, 90(2):022512, 2014.

[110] HGC Werij, Chris H Greene, CE Theodosiou, and Alan Gallagher. Oscillator strengths and radiative branching ratios in atomic Sr. *Phys. Rev. A*, 46(3):1248, 1992.

[111] Robin Santra, Kevin V Christ, and Chris H Greene. Properties of metastable alkaline-earth-metal atoms calculated using an accurate effective core potential. *Phys. Rev. A*, 69(4):042510, 2004.

[112] Martin M. Boyd. *High Precision Spectroscopy of Strontium in an Optical Lattice: Towards a New Standard of Frequency and Time*. PhD thesis, University of Colorado at Boulder, 2007.

[113] Andrei Derevianko. Feasibility of cooling and trapping metastable alkaline-earth atoms. *Phys. Rev. Lett.*, 87(2):023002, 2001.

[114] Sarah B Nagel, CE Simien, S Laha, P Gupta, VS Ashoka, and TC Killian. Magnetic trapping of metastable $^3P_2$ atomic strontium. *Phys. Rev. A*, 67(1):011401, 2003.

[115] Masami Yasuda and Hidetoshi Katori. Lifetime Measurement of the ^{3}P$_2$ Metastable State of Strontium Atoms. *Phys. Rev. Lett.*, 92(15):153004, 2004.

[116] N Poli, G Ferrari, M Prevedelli, F Sorrentino, RE Drullinger, and GM Tino. Laser sources for precision spectroscopy on atomic strontium. *Spectrochim. Acta A*, 63(5):981–986, 2006.

[117] PG Mickelson, YN Martinez de Escobar, P Anzel, BJ DeSalvo, SB Nagel, AJ Traverso, M Yan, and TC Killian. Repumping and spectroscopy of laser-cooled Sr atoms using the $(5s5p)^3P_2$–$(5s4d)^3D_2$ transition. *J. Phys. B: At., Mol. Opt. Phys.*, 42(23):235001, 2009.

[118] TG Tiecke, SD Gensemer, A Ludewig, and JTM Walraven. High-flux two-dimensional magneto-optical-trap source for cold lithium atoms. *Phys. Rev. A*, 80(1):013409, 2009.

[119] Ingo Nosske, Luc Couturier, Fachao Hu, Canzhu Tan, Chang Qiao, Jan Blume, Y H Jiang, Peng Chen, and Matthias Weidemüller. Two-dimensional magneto-optical trap as a source for cold strontium atoms. *Phys. Rev. A*, 96(5):053415, 2017.

[120] G Lamporesi, S Donadello, S Serafini, and G Ferrari. Compact high-flux source of cold sodium atoms. *Rev. Sci. Instrum.*, 84(6):063102, 2013.

[121] Takayuki Kurosu and Fujio Shimizu. Laser cooling and trapping of alkaline earth atoms. *Jpn. J. Appl. Phys.*, 31(3R):908, 1992.

[122] Xinye Xu, Thomas H Loftus, Matthew J Smith, John L Hall, Alan Gallagher, and Jun Ye. Dynamics in a two-level atom magneto-optical trap. *Phys. Rev. A*, 66(1):011401, 2002.

[123] Xinye Xu, Thomas H Loftus, Josh W Dunn, Chris H Greene, John L Hall, Alan Gallagher, and Jun Ye. Single-stage sub-Doppler cooling of alkaline earth atoms. *Phys. Rev. Lett.*, 90(19):193002, 2003.

[124] ARL Caires, GD Telles, MW Mancini, LG Marcassa, VS Bagnato, D Wilkowski, and R Kaiser. Intensity dependence for trap loss rate in a magneto-optical trap of strontium. *Braz. J. Phys.*, 34(4A):1504–1509, 2004.

[125] Wang Shao-Kai, Wang Qiang, Lin Yi-Ge, Wang Min-Ming, Lin Bai-Ke, Zang Er-Jun, Li Tian-Chu, and Fang Zhan-Jun. Cooling and Trapping ^{88}Sr Atoms with 461 nm Laser. *Chin. Phys. Lett.*, 26(9):093202, 2009.

[126] Takashi Mukaiyama, Hidetoshi Katori, Tetsuya Ido, Ying Li, and Makoto Kuwata-Gonokami. Recoil-Limited Laser Cooling of ^{87}Sr Atoms near the Fermi Temperature. *Phys. Rev. Lett.*, 90(11):113002, 2003.

[127] Thierry Chaneliere, Ling He, Robin Kaiser, and David Wilkowski. Three dimensional cooling and trapping with a narrow line. *Eur. Phys. J. D*, 46(3):507–515, 2008.

[128] K Yu Khabarova, Aleksei A Galyshev, Sergei Aleksandrovich Strelkin, Aleksei Sergeevich Kostin, Gleb Sergeevich Belotelov, Oleg Igorevich Berdasov, A Gribov, Nikolai Nikolaevich Kolachevsky, and Sergei Nikolaevich Slyusarev. Spectroscopy of intercombination transition $^1S_0$–$^3P_1$ for secondary cooling of strontium atoms. *Quantum Electron.*, 45(2):166, 2015.

[129] Ryan K Hanley, Paul Huillery, Niamh C Keegan, Alistair D Bounds, Danielle Boddy, Ric-

cardo Faoro, and Matthew PA Jones. Quantitative simulation of a magneto-optical trap operating near the photon recoil limit. *J. Mod. Opt.*, pages 1–10, 2017.

[130] Eric Wille. *Preparation of an Optically Trapped Fermi-Fermi Mixture of ^{6}Li and ^{40}K Atoms and Characterization of the Interspecies Interactions by Feshbach Spectroscopy*. PhD thesis, University of Innsbruck, 2009.

[131] Marco Schioppo. *Development of a transportable strontium optical clock*. PhD thesis, University of Florence, 2010.

[132] James Millen. *A cold strontium Rydberg gas*. PhD thesis, Durham University, 2011.

[133] Oerlikon Leybold Vacuum. Fundamentals of Vacuum Technology, 2007.

[134] E Maccallini, P Manini, A Conte, F Siviero, and A Bonucci. New Approach to meet vacuum requirements in UHV/XHV systems by Non Evaporable Getter Technology. In *Journal of Physics: Conference Series*, volume 390, page 012006. IOP Publishing, 2012.

[135] TF Gallagher. Rydberg atoms. *Rep. Prog. Phys.*, 51(2):143, 1988.

[136] CS Hofmann, G Günter, H Schempp, Nele LM Müller, A Faber, H Busche, M Robert-de Saint-Vincent, S Whitlock, and M Weidemüller. An experimental approach for investigating many-body phenomena in Rydberg-interacting quantum systems. *Front. Phys.*, 9(5):571–586, 2014.

[137] M Viteau, J Radogostowicz, A Chotia, M G Bason, N Malossi, F Fuso, D Ciampini, O Morsch, I I Ryabtsev, and E Arimondo. Ion detection in the photoionization of a Rb Bose–Einstein condensate. *J. Phys. B: At., Mol. Opt. Phys.*, 43(15):155301, 2010.

[138] Robert Löw. *A versatile setup for experiments with Rubidium Bose Einstein condensates: From optical lattices to Rydberg matter*. PhD thesis, Universität Stuttgart, 2006.

[139] Nele Lotte Marie Müller. Excitation and Detection of Rydberg Atoms in an Ultracold Gas. Master's thesis, University of Heidelberg, 2010.

[140] T Arpornthip, CA Sackett, and KJ Hughes. Vacuum-pressure measurement using a magneto-optical trap. *Phys. Rev. A*, 85(3):033420, 2012.

[141] Jun He, Bao-dong Yang, Yong-jie Cheng, Tian-cai Zhang, and Jun-min Wang. Extending the trapping lifetime of single atom in a microscopic far-off-resonance optical dipole trap. *Front. Phys.*, 6(3):262–270, 2011.

[142] K. Metzger. Dreidimensionale Feldberechnung starr magnetisierter Permanentmagnete mit einer Anwendung in eisenlosen elektrischen Maschinen. *Arch. f. Elektrotech.*, 59(4):229–242, Jul 1977.

[143] Richard Allen Matula. Electrical resistivity of copper, gold, palladium, and silver. *J. Phys. Chem. Ref. Data*, 8(4):1147–1298, 1979.

[144] Gerhard Zürn. Realization of an Optical Microtrap for a Highly Degenerate Fermi Gas. Mas-

ter's thesis, University of Heidelberg, 2009.

[145] T. Bergeman, Gidon Erez, and Harold J. Metcalf. Magnetostatic trapping fields for neutral atoms. *Phys. Rev. A*, 35:1535–1546, Feb 1987.

[146] Aidan Arnold. *Preparation and Manipulation of an ^{87}Rb Bose-Einstein Condensate*. PhD thesis, University of Sussex, 1999.

[147] Yosuke Shimada, Yuko Chida, Nozomi Ohtsubo, Takatoshi Aoki, Makoto Takeuchi, Takahiro Kuga, and Yoshio Torii. A simplified 461-nm laser system using blue laser diodes and a hollow cathode lamp for laser cooling of Sr. *Rev. Sci. Instrum.*, 84(6):063101, 2013.

[148] C J H Pagett, P H Moriya, R Celistrino Teixeira, R F Shiozaki, M Hemmerling, and P W Courteille. Injection locking of a low cost high power laser diode at 461 nm. *Rev. Sci. Instrum.*, 87(5):053105, 2016.

[149] Alda Arias, Stephan Helmrich, Christoph Schweiger, Lynton Ardizzone, Graham Lochead, and Shannon Whitlock. Versatile, high-power 460 nm laser system for Rydberg excitation of ultracold potassium. *Opt. Express*, 25(13):14829–14839, 2017.

[150] Luc Couturier, Ingo Nosske, Fachao Hu, Canzhu Tan, Chang Qiao, Y H Jiang, Peng Chen, and Matthias Weidemüller. Laser frequency stabilization using a commercial wavelength meter. *Rev. Sci. Instrum.*, 89(4):043103, 2018.

[151] J. Deiglmayr, M. Reetz-Lamour, T. Amthor, S. Westermann, A. L. de Oliveira, and M. Weidemüller. Coherent excitation of Rydberg atoms in an ultracold gas. *Opt. Comm.*, 264:293, 2006.

[152] RE Scholten. Enhanced laser shutter using a hard disk drive rotary voice-coil actuator. *Rev. Sci. Instrum.*, 78(2):026101, 2007.

[153] RWP Drever, John L Hall, FV Kowalski, J Hough, GM Ford, AJ Munley, and H Ward. Laser phase and frequency stabilization using an optical resonator. *Appl. Phys. B*, 31(2):97–105, 1983.

[154] Eric D Black. An introduction to Pound–Drever–Hall laser frequency stabilization. *Am. J. Phys.*, 69(1):79–87, 2001.

[155] B. C. Young, F. C. Cruz, W. M. Itano, and J. C. Bergquist. Visible Lasers with Subhertz Linewidths. *Phys. Rev. Lett.*, 82:3799–3802, May 1999.

[156] Brian J. DeSalvo. *Ultralong-Range Molecules and Rydberg Blockade in Ultracold ^{84}Sr*. PhD thesis, Rice University, 2015.

[157] Elizabeth M Bridge, Niamh C Keegan, Alistair D Bounds, Danielle Boddy, Daniel P Sadler, and Matthew PA Jones. Tunable cw UV laser with <35 kHz absolute frequency instability for precision spectroscopy of Sr Rydberg states. *Opt. Express*, 24(3):2281–2292, 2016.

[158] Heiner Saßmannshausen, Frédéric Merkt, and Johannes Deiglmayr. High-resolution spec-

troscopy of Rydberg states in an ultracold cesium gas. *Phys. Rev. A*, 87(3):032519, 2013.

[159] Jieying Wang, Jiandong Bai, Jun He, and Junmin Wang. Single-photon cesium Rydberg excitation spectroscopy using 318.6-nm UV laser and room-temperature vapor cell. *Opt. Express*, 25(19):22510–22518, 2017.

[160] Hao-Ze Chen, Xing-Can Yao, Yu-Ping Wu, Xiang-Pei Liu, Xiao-Qiong Wang, Yu-Ao Chen, and Jian-Wei Pan. Narrow-linewidth cooling of ^{6}Li atoms using the 2S-3P transition. *Appl. Phys. B*, 122(11):281, 2016.

[161] R. J. Rengelink, R. P. M. J. W. Notermans, and W. Vassen. A simple 2 W continuous-wave laser system for trapping ultracold metastable helium atoms at the 319.8 nm magic wavelength. *Appl. Phys. B*, 122(5):122, Apr 2016.

[162] C Monroe, W Swann, H Robinson, and C Wieman. Very cold trapped atoms in a vapor cell. *Phys. Rev. Lett.*, 65(13):1571, 1990.

[163] S Weyers, E Aucouturier, C Valentin, and N Dimarcq. A continuous beam of cold cesium atoms extracted from a two-dimensional magneto-optical trap. *Opt. Commun.*, 143(1-3):30–34, 1997.

[164] Z T Lu, K L Corwin, M J Renn, M H Anderson, Eric A Cornell, and C E Wieman. Low-velocity intense source of atoms from a magneto-optical trap. *Phys. Rev. Lett.*, 77(16):3331, 1996.

[165] G Reinaudi, CB Osborn, K Bega, and T Zelevinsky. Dynamically configurable and optimizable Zeeman slower using permanent magnets and servomotors. *J. Opt. Soc. Am. B*, 29(4):729–733, 2012.

[166] Ian R Hill, Yuri B Ovchinnikov, Elizabeth M Bridge, E Anne Curtis, and Patrick Gill. Zeeman slowers for strontium based on permanent magnets. *J. Phys. B: At., Mol. Opt. Phys.*, 47(7):075006, 2014.

[167] V Lebedev and DM Weld. Self-assembled Zeeman slower based on spherical permanent magnets. *J. Phys. B: At., Mol. Opt. Phys.*, 47(15):155003, 2014.

[168] Wang Qiang, Lin Yi-Ge, Gao Fang-Lin, Li Ye, Lin Bai-Ke, Meng Fei, Zang Er-Jun, Li Tian-Chu, and Fang Zhan-Jun. A Longitudinal Zeeman Slower Based on Ring-Shaped Permanent Magnets for a Strontium Optical Lattice Clock. *Chin. Phys. Lett.*, 32(10):100701, 2015.

[169] HCW Beijerinck and NF Verster. Velocity distribution and angular distribution of molecular beams from multichannel arrays. *J. Appl. Phys.*, 46(5):2083–2091, 1975.

[170] B Jana, A Majumder, KB Thakur, and AK Das. Note: Design principles of a linear array multi-channel effusive metal-vapor atom source. *Rev. Sci. Instrum.*, 84(10):106113, 2013.

[171] Sören Dörscher, Alexander Thobe, Bastian Hundt, André Kochanke, Rodolphe Le Targat, Patrick Windpassinger, Christoph Becker, and Klaus Sengstock. Creation of quantum-

degenerate gases of ytterbium in a compact 2D-/3D-magneto-optical trap setup. *Rev. Sci. Instrum.*, 84(4):043109, 2013.

[172] Marianna S Safronova, Mikhail G Kozlov, and Charles W Clark. Blackbody radiation shifts in optical atomic clocks. *IEEE Trans. Ultrason. Ferroelectr. Freq. Control*, 59(3):439, 2012.

[173] Tao Yang, Kanhaiya Pandey, Mysore Srinivas Pramod, Frederic Leroux, Chang Chi Kwong, Elnur Hajiyev, Zhong Yi Chia, Bess Fang, and David Wilkowski. A high flux source of cold strontium atoms. *Eur. Phys. J. D*, 69(10):1–12, 2015.

[174] J Schoser, A Batär, R Löw, V Schweikhard, A Grabowski, Yu B Ovchinnikov, and T Pfau. Intense source of cold Rb atoms from a pure two-dimensional magneto-optical trap. *Phys. Rev. A*, 66(2):023410, 2002.

[175] Simone Götz, Bastian Höltkemeier, Christoph S Hofmann, Dominic Litsch, Brett D DePaola, and Matthias Weidemüller. Versatile cold atom target apparatus. *Rev. Sci. Instrum.*, 83(7):073112, 2012.

[176] Patrick Berthoud, Alain Joyet, Gregor Dudle, N Sagna, and Pierre Thomann. A continuous beam of slow, cold cesium atoms magnetically extracted from a 2D magneto-optical trap. *Europhys. Lett.*, 41(2):141, 1998.

[177] James R Kellogg, Dennis Schlippert, James M Kohel, Robert J Thompson, David C Aveline, and Nan Yu. A compact high-efficiency cold atom beam source. *Appl. Phys. B*, 109(1):61–64, 2012.

[178] J Catani, P Maioli, L De Sarlo, F Minardi, and M Inguscio. Intense slow beams of bosonic potassium isotopes. *Phys. Rev. A*, 73(3):033415, 2006.

[179] M Petersen, R Chicireanu, S. T. Dawkins, Daniel Varela Magalhães, C Mandache, Y Le Coq, A Clairon, and S Bize. Doppler-Free Spectroscopy of the $^1S_0$-$^3P_0$ Optical Clock Transition in Laser-Cooled Fermionic Isotopes of Neutral Mercury. *Phys. Rev. Lett.*, 101(18):183004, 2008.

[180] Marcin Witkowski, Bartłomiej Nagórny, Rodolfo Munoz-Rodriguez, Roman Ciuryło, Piotr Szymon Żuchowski, Sławomir Bilicki, Marcin Piotrowski, Piotr Morzyński, and Michał Zawada. Dual Hg-Rb magneto-optical trap. *Opt. Express*, 25(4):3165–3179, 2017.

[181] E Pedrozo-Peñafiel, F Vivanco, P Castilho, RR Paiva, KM Farias, and VS Bagnato. Direct comparison between a two-dimensional magneto-optical trap and a Zeeman slower as sources of cold sodium atoms. *Laser Phys. Lett.*, 13(6):065501, 2016.

[182] Colin D Bruzewicz, Robert McConnell, John Chiaverini, and Jeremy M Sage. Scalable loading of a two-dimensional trapped-ion array. *Nat. Commun.*, 7:13005, 2016.

[183] Matthew A Norcia, Matthew N Winchester, Julia RK Cline, and James K Thompson. Superradiance on the millihertz linewidth strontium clock transition. *Sci. Adv.*, 2(10):e1601231,

2016.

[184] Benjamin J. Bloom. *Building a Better Atomic Clock*. PhD thesis, University of Colorado at Boulder, 2014.

[185] Nelson Darkwah Oppong. Towards a Degenerate Fermi Gas of Strontium-87 in a 3D Optical Lattice. Master's thesis, University of Colorado at Boulder, 2015.

[186] Bjorn Ole Kock. *Magneto-optical trapping of strontium for use as a mobile frequency reference*. PhD thesis, University of Birmingham, 2013.

[187] Yuri B Ovchinnikov. A Zeeman slower based on magnetic dipoles. *Opt. Commun.*, 276(2):261–267, 2007.

[188] Daniel A. Steck. Quantum and atom optics, 2007.

[189] VS Letokhov and Vladimir Georgievich Minogin. Laser radiation pressure on free atoms. *Phys. Rep.*, 73(1):1–65, 1981.

[190] Bo Gao. Effects of Zeeman degeneracy on the steady-state properties of an atom interacting with a near-resonant laser field: Resonance flourescence. *Phys. Rev. A*, 50(5):4139, 1994.

[191] Michael A Joffe, Wolfgang Ketterle, Alex Martin, and David E Pritchard. Transverse cooling and deflection of an atomic beam inside a Zeeman slower. *J. Opt. Soc. Am. B*, 10(12):2257–2262, 1993.

[192] ER Eliel, W Hogervorst, T Olsson, and LR Pendrill. High Resolution Laser Spectroscopy of Low-Lying p-States in Sr I and Ba I. *Z. Phys. A*, 311(1):1–6, 1983.

[193] David S Weiss, Erling Riis, Yaakov Shevy, P Jeffrey Ungar, and Steven Chu. Optical molasses and multilevel atoms: experiment. *J. Opt. Soc. Am. B*, 6(11):2072–2083, 1989.

[194] Graham Lochead. *Excited state spatial distributions in a cold strontium gas*. PhD thesis, Durham University, 2012.

[195] H-Jürgen Kluge and Hatto Sauter. Levelcrossing Experiments in the First Excited $^1P_1$ States of the Alkaline Earths. *Z. Phys.*, 270(4):295–309, 1974.

[196] Alan L Migdall, John V Prodan, William D Phillips, Thomas H Bergeman, and Harold J Metcalf. First observation of magnetically trapped neutral atoms. *Phys. Rev. Lett.*, 54(24):2596, 1985.

[197] Jürgen Stuhler, Piet O Schmidt, Sven Hensler, Jörg Werner, Jürgen Mlynek, and Tilman Pfau. Continuous loading of a magnetic trap. *Phys. Rev. A*, 64(3):031405, 2001.

[198] T Loftus, JR Bochinski, and TW Mossberg. Magnetic trapping of ytterbium and the alkaline-earth metals. *Phys. Rev. A*, 66(1):013411, 2002.

[199] AM Steane, M Chowdhury, and CJ Foot. Radiation force in the magneto-optical trap. *J. Opt. Soc. Am. B*, 9(12):2142–2158, 1992.

[200] DS Barker, BJ Reschovsky, NC Pisenti, and GK Campbell. Enhanced magnetic trap loading

for atomic strontium. *Phys. Rev. A*, 92(4):043418, 2015.

[201] A Traverso, R Chakraborty, YN Martinez De Escobar, PG Mickelson, SB Nagel, M Yan, and TC Killian. Inelastic and elastic collision rates for triplet states of ultracold strontium. *Phys. Rev. A*, 79(6):060702, 2009.

[202] Danielle Boddy. *First observations of Rydberg blockade in a frozen gas of divalent atoms*. PhD thesis, Durham University, 2014.

[203] J.-H. Choi, B. Knuffman, T. Cubel Liebisch, A. Reinhard, and G. Raithel. Cold Rydberg Atoms. In C.C. Lin P.R. Berman and E. Arimondo, editors, *Advances in Atomic, Molecular and Optical Physics*, volume Volume 54, pages 131–202. Academic Press, 2006.

[204] T. Amthor, Reetz-Lamour, and M. Weidemüller. Frozen Rydberg Gases. In M. Weidemüller and C. Zimmermann, editors, *Cold Atoms and Molecules*, chapter Cold Rydberg Gases. Wiley-VCH, 2009.

[205] Robert Löw, Hendrik Weimer, Johannes Nipper, Jonathan B Balewski, Björn Butscher, Hans Peter Büchler, and Tilman Pfau. An experimental and theoretical guide to strongly interacting Rydberg gases. *J. Phys. B: At., Mol. Opt. Phys.*, 45(11):113001, 2012.

[206] Peter Schauß. *High-resolution imaging of ordering in Rydberg many-body systems*. PhD thesis, Ludwig-Maximilians-Universität München, 2014.

[207] CL Vaillant, MPA Jones, and RM Potvliege. Long-range Rydberg–Rydberg interactions in calcium, strontium and ytterbium. *J. Phys. B: At., Mol. Opt. Phys.*, 45(13):135004, 2012.

[208] II Beterov, II Ryabtsev, DB Tretyakov, and VM Entin. Quasiclassical calculations of blackbody-radiation-induced depopulation rates and effective lifetimes of Rydberg nS, nP, and nD alkali-metal atoms with $n \leqslant 80$. *Phys. Rev. A*, 79(5):052504, 2009.

[209] I. I. Beterov, D. B. Tretyakov, I. I. Ryabtsev, A. Ekers, and N. N. Bezuglov. Ionization of sodium and rubidium nS, nP, and nD Rydberg atoms by blackbody radiation. *Phys. Rev. A*, 75:052720, 2007.

[210] I. I. Beterov, D. B. Tretyakov, I. I. Ryabtsev, V. M. Entin, A. Ekers, and N. N. Bezuglov. Ionization of Rydberg atoms by blackbody radiation. *New J. Phys.*, 11:013052, 2009.

[211] Brian Harold Bransden, Charles Jean Joachain, and Theodor J Plivier. *Physics of atoms and molecules*. Pearson Education India, 2003.

[212] Markus Mack, Florian Karlewski, Helge Hattermann, Simone Höckh, Florian Jessen, Daniel Cano, and József Fortágh. Measurement of absolute transition frequencies of ^{87}Rb to nS and nD Rydberg states by means of electromagnetically induced transparency. *Phys. Rev. A*, 83(5):052515, 2011.

[213] K. Singer, J. Stanojevic, M. Weidemüller, and R. Côté. Long-range interactions between alkali Rydberg atom pairs correlated to the ns-ns, np-np and nd-nd asymptotes. *J. Phys. B*,

38:S295, 2005.

[214] F. Robicheaux, J. V. Hernández, T. Topçu, and L. D. Noordam. Simulation of coherent interactions between Rydberg atoms. *Phys. Rev. A*, 70:042703, Oct 2004.

[215] T Förster. Zwischenmolekulare Energiewanderung und Fluoreszenz. *Ann. Phys.*, 437(1-2):55–75, 1948.

[216] T.G. Walker and M. Saffman. Zeros of Rydberg-Rydberg Föster interactions. *J. Phys. B*, 38:S309, 2005.

[217] A. Reinhard, T. Cubel Liebisch, B. Knuffman, and G. Raithel. Level shifts of rubidium Rydberg states due to binary interactions. *Phys. Rev. A*, 75:032712, 2007.

[218] Thomas J. Carroll, Katharine Claringbould, Anne Goodsell, M. J. Lim, and Michael W. Noel. Angular Dependence of the Dipole-Dipole Interaction in a Nearly One-Dimensional Sample of Rydberg Atoms. *Phys. Rev. Lett.*, 93:153001, 2004.

[219] Christophe Boisseau, Ionel Simbotin, and Robin Côté. Macrodimers: Ultralong Range Rydberg Molecules. *Phys. Rev. Lett.*, 88:133004, 2002.

[220] Arne Schwettmann, Jeff Crawford, K. Richard Overstreet, and James P. Shaffer. Cold Cs Rydberg-gas interactions. *Phys. Rev. A*, 74:020701(R), 2006.

[221] Nolan Samboy and Robin Côté. Rubidium Rydberg macrodimers. *J. Phys. B: At., Mol. Opt. Phys.*, 44(18):184006, 2011.

[222] Nolan Samboy, Jovica Stanojevic, and Robin Côté. Formation and properties of Rydberg macrodimers. *Phys. Rev. A*, 83:050501, 2011.

[223] Vladan Vuletic. When superatoms talk photons. *Nat. Phys. News & Views*, 2:801, 2006.

[224] M. Saffman and T. G. Walker. Creating single-atom and single-photon sources from entangled atomic ensembles. *Phys. Rev. A*, 66:065403, 2002.

[225] C. Ates, I. Lesanovsky, C. S. Adams, and K. J. Weatherill. Fast and Quasideterministic Single Ion Source from a Dipole-Blockaded Atomic Ensemble. *Phys. Rev. Lett.*, 110:213003, May 2013.

[226] DP Sadler, EM Bridge, D Boddy, AD Bounds, NC Keegan, G Lochead, MPA Jones, and Beatriz Olmos. Radiation trapping in a dense cold Rydberg gas. *Phys. Rev. A*, 95(1):013839, 2017.

[227] A. D. Bounds, N. C. Jackson, R. K. Hanley, R. Faoro, E. M. Bridge, P. Huillery, and M. P. A. Jones. Rydberg-Dressed Magneto-optical Trap. *Phys. Rev. Lett.*, 120:183401, May 2018.

[228] BJ DeSalvo, JA Aman, FB Dunning, TC Killian, HR Sadeghpour, S Yoshida, and J Burgdörfer. Ultra-long-range Rydberg molecules in a divalent atomic system. *Phys. Rev. A*, 92(3):031403, 2015.

[229] F Camargo, JD Whalen, R Ding, HR Sadeghpour, S Yoshida, J Burgdörfer, FB Dunning,

and TC Killian. Lifetimes of ultra-long-range strontium Rydberg molecules. *Phys. Rev. A*, 93(2):022702, 2016.

[230] JA Aman, BJ DeSalvo, FB Dunning, TC Killian, S Yoshida, and J Burgdörfer. Trap losses induced by near-resonant Rydberg dressing of cold atomic gases. *Phys. Rev. A*, 93(4):043425, 2016.

[231] J. D. Whalen, F. Camargo, R. Ding, T. C. Killian, F. B. Dunning, J. Pérez-Ríos, S. Yoshida, and J. Burgdörfer. Lifetimes of ultralong-range strontium Rydberg molecules in a dense Bose-Einstein condensate. *Phys. Rev. A*, 96:042702, Oct 2017.

[232] F. Camargo, R. Schmidt, J. D. Whalen, R. Ding, G. Woehl, S. Yoshida, J. Burgdörfer, F. B. Dunning, H. R. Sadeghpour, E. Demler, and T. C. Killian. Creation of Rydberg Polarons in a Bose Gas. *Phys. Rev. Lett.*, 120:083401, Feb 2018.

[233] S. Mauger, J. Millen, and M. P. A. Jones. Spectroscopy of strontium Rydberg states using electromagnetically induced transparency. *J. Phys. B*, 40:F319, 2007.

[234] S. Ye, X. Zhang, T. C. Killian, F. B. Dunning, M. Hiller, S. Yoshida, S. Nagele, and J. Burgdörfer. Production of very-high-n strontium Rydberg atoms. *Phys. Rev. A*, 88:043430, Oct 2013.

[235] M. Hiller, S. Yoshida, J. Burgdörfer, S. Ye, X. Zhang, and F. B. Dunning. Characterizing high-n quasi-one-dimensional strontium Rydberg atoms. *Phys. Rev. A*, 89:023426, Feb 2014.

[236] S. Ye, X. Zhang, F. B. Dunning, S. Yoshida, M. Hiller, and J. Burgdörfer. Efficient three-photon excitation of quasi-one-dimensional strontium Rydberg atoms with $n \sim 300$. *Phys. Rev. A*, 90:013401, Jul 2014.

[237] X. Zhang, F. B. Dunning, S. Yoshida, and J. Burgdörfer. Rydberg blockade effects at $n \sim 300$ in strontium. *Phys. Rev. A*, 92:051402, Nov 2015.

[238] Ryan K Hanley, Alistair D Bounds, Paul Huillery, Niamh C Keegan, Riccardo Faoro, Elizabeth M Bridge, Kevin J Weatherill, and Matthew P A Jones. Probing interactions of thermal Sr Rydberg atoms using simultaneous optical and ion detection. *J. Phys. B: At., Mol. Opt. Phys.*, 50(11):115002, 2017.

[239] G. Fields, X. Zhang, F. B. Dunning, S. Yoshida, and J. Burgdörfer. Autoionization of very-high-n strontium Rydberg states. *Phys. Rev. A*, 97:013429, Jan 2018.

[240] C-J Lorenzen and K Niemax. Quantum Defects of the $n^2P_{1/2,3/2}$ Levels in ^{39}K I and ^{85}Rb I. *Phys. Scr.*, 27(4):300, 1983.

[241] Wenhui Li, I Mourachko, MW Noel, and TF Gallagher. Millimeter-wave spectroscopy of cold Rb Rydberg atoms in a magneto-optical trap: Quantum defects of the ns, np, and nd series. *Phys. Rev. A*, 67(5):052502, 2003.

[242] JE Sansonetti. Wavelengths, transition probabilities, and energy levels for the spectra of

strontium ions (Sr II through Sr XXXVIII). *J. Phys. Chem. Ref. Data*, 41(1):013102–013102, 2012.

[243] C L Vaillant, M P A Jones, and R M Potvliege. Multichannel quantum defect theory of strontium bound Rydberg states. *J. Phys. B: At., Mol. Opt. Phys.*, 47(15):155001, 2014.

[244] Christophe L. Vaillant. *Long-Range Interactions in One- and Two-Electron Rydberg Atoms*. PhD thesis, Durham University, 2014.

[245] Turker Topcu and Andrei Derevianko. Rydberg blockade with multivalent atoms: effect of Rydberg series perturbation on van der Waals interactions. *arXiv preprint arXiv:1505.07152*, 2015.

[246] CL Vaillant, RM Potvliege, and MPA Jones. Intercombination effects in resonant energy transfer. *Phys. Rev. A*, 92(4):042705, 2015.

[247] Christopher J. Foot. *Atomic Physics*, volume 7. Oxford University Press, 2005.

[248] S Kunze, R Hohmann, H-J Kluge, J Lantzsch, L Monz, J Stenner, K Stratmann, K Wendt, and K Zimmer. Lifetime measurements of highly excited Rydberg states of strontium I. *Z. Phys. D*, 27(2):111–114, 1993.

[249] R Beigang, K Lücke, D Schmidt, A Timmermann, and PJ West. One-photon laser spectroscopy of Rydberg series from metastable levels in calcium and strontium. *Phys. Scr.*, 26(3):183, 1982.

[250] Tetsuya Ido, Thomas H. Loftus, Martin M. Boyd, Andrew D. Ludlow, Kevin W. Holman, and Jun Ye. Precision Spectroscopy and Density-Dependent Frequency Shifts in Ultracold Sr. *Phys. Rev. Lett.*, 94:153001, Apr 2005.

[251] C. Gaul, B. J. DeSalvo, J. A. Aman, F. B. Dunning, T. C. Killian, and T. Pohl. Resonant Rydberg Dressing of Alkaline-Earth Atoms via Electromagnetically Induced Transparency. *Phys. Rev. Lett.*, 116:243001, Jun 2016.

[252] S Helmrich, A Arias, N Pehoviak, and S Whitlock. Two-body interactions and decay of three-level Rydberg-dressed atoms. *J. Phys. B: At., Mol. Opt. Phys.*, 49(3):03LT02, 2016.

[253] Feng Gao, Hui Liu, Peng Xu, X Tian, Y Wang, J Ren, Haibin Wu, and Hong Chang. Precision measurement of transverse velocity distribution of a strontium atomic beam. *AIP Adv.*, 4(2):027118, 2014.

Acknowledgements

First of all I would like to thank my supervisor Prof. Matthias Weidemüller for giving me the opportunity to do research in a very interesting and challenging field of physics, with the lab being located in the no less interesting and vibrant city of Shanghai, which is nicknamed as the "magic city" (魔都) in Chinese. Without you I would certainly not have started to pursue a PhD degree at all. I am glad that during the last few PhD years I had the chance to come in contact with top researchers in our field at conferences and at visits in our institute.

In the last 3.5 years I saw our institute – the USTC Shanghai Institute for Advanced Studies – growing, with more and more research groups in different fields of quantum physics being established. It was inspiring to live and work at the place where the experiments on the "quantum satellite" Micius are being planned, which was launched in 2016 and now achieved impressive results.

In these few years I spent a lot of time with my labmates, who are Luc Couturier, Qiao Chang (乔畅), Hu Fachao (胡发超), Tan Canzhu (檀灿竹) and our local group leader Chen Peng (陈鹏). I would like to thank all of you for any help which you gave me during this time period to accomplish results in the lab, to understand physics aspects, to deal with nasty technological problems or to write my thesis. I hope that our lab will be spared from any more technological failures in the future, and that it will yield many beautiful, inspiring and useful results.

I would like to express my special gratitude to my labmates, and also to Valentin Ivannikov, Rui Jun (芮俊) and Henning Labuhn for giving me useful comments on my thesis during the last few weeks of writing, and for your friendship!

I would like to thank Jan Blume who worked together with us during the early days in 2014/2015, when in the lab was nothing more than three empty optical tables, as well as our (former) secretaries Cheng Huan (程欢), Jin Chengcheng (金成成) and Maggie Sun (孙美琪). Furthermore, I would like to thank Prof. Jiang Yuhai (江玉海) from the Shanghai Advanced Research Institute, and André Salzinger, Gerhard Zürn and Dominic Litsch from Heidelberg who helped us to get the lab slowly running in 2015/2016.

Then I would like to thank Prof. Florian Schreck and Benjamin Pasquiou for the lab tour in Amsterdam in March 2014, and Prof. Matt Jones and Elizabeth Bridge for the lab tour in Durham in March 2015.

It was very nice to be part of the Quantum Dynamics group in Heidelberg in 2014, and I would like to thank some people from the cold atomic physics labs there for creating such

a nice working atmosphere, in particular Prof. Shannon Whitlock, Stephan Helmrich, Alda Arias, Bastian Höltkemeier, Henry Lopez, Pascal Weckesser, Juris Ulmanis, Stephan Häfner, Vladislav Gavryusev, Miguel Ferreira-Cao, Vincent Klinkhamer and Florian Ritterbusch.

It was also very nice to be part of the growing community of researchers in Shanghai. Here I would like to acknowledge (some of you already left) Rui Jun (芮俊) and Lu Jiawen (陆佳雯), Liu Yaxiong (刘亚雄), Prof. Yao Xingcan (姚星灿), Wu Yuping (吴裕平), Chen Haoze (陈昊泽), Zhu Minjie (朱敏杰), Shen Qi (沈奇), Sun Qichao (孙启超), Prof. Chen Shuai (陈帅), Prof. Zhao Bo (赵博), Dai Hanning (戴汉宁) and Zhang Wenzhuo (张文卓).

Special thanks also to Prof. Yuan Zhensheng (苑震生), my co-supervisor during my master thesis, for originally letting me being part of his research group in Hefei from 2012/09 to 2013/11. Thanks also to my former labmates in Hefei Xiao Bo (肖波), Li Mengda (李梦达), Xie Qian (谢虔), Zheng Yongguang (郑永光) and Sun Hui (孙辉), for letting me become familiar with cold atom lab techniques and for helping me to orientate myself in China.

I would like to thank Jeff Zhao from Fermion Instruments (Shanghai), as well as Dario Nicolosi and Andrea Cadoppi from SAES Getters for help regarding problems with the vacuum system.

Li Jun (李骏), our trip to Jixi in mid-2015 was very nice! I would also like to thank Yin Yayun (印亚云), Yang Kuixing (杨奎星), Yuan Tao (苑涛) and Nan Jue (南珏) for a few hotly contested table football matches. As well as my football comrades Dai Baiyang (代白杨) and Li Haijiang (李海疆), and Zhao Yicheng (赵翌程), Zhang Wei (张伟) and the others from the USTC MBA course.

I would like to thank Prof. Barry Sanders and Ish Dhand for a few nice dinners in the “rice restaurant” (醉爱餐馆), where I often enjoyed the fantastic “thousand leaves tofu” (千叶豆腐). Also thanks for a few nice meals to Mudassar Maraj and Mohammed Abdul. And thanks to the security guards of our institute who invited Luc and me for meals during Chinese New Years, when nearly everybody else had left for their homes.

Then I would like to thank my parents Dietmar and Regine for bringing me up as you did, as well as Lisa, and of course Frido for repeated Tritte in den Hintern. Thanks to all my relatives – it was always nice to see you during the past Christmases, even though it was always quite short recently. Thank you Moritz and Katia, for being good friends in Shanghai. Thanks to the cats from the USTC zoo for lifting my spirits every single day, and thanks to my dear flatmates from North Xiangyang Road. Thank you Ding Ling (丁玲), Liang Gang (梁钢) and Liang Sihao (梁思好) for your warm hospitality. And last but not least, thank you Sisi (思思), thanks for being my girlfriend, for dragging me out from the lab sometimes, for putting me on horsebacks at exotic places, and generally thank you for being there.

Publications

Published papers

1. Ingo Nosske, Luc Couturier, Fachao Hu, Canzhu Tan, Chang Qiao, Jan Blume, Y. H. Jiang, Peng Chen, and Matthias Weidemüller. Two-dimensional magneto-optical trap as a source for cold strontium atoms. *Phys. Rev. A* 96, 053415 (2017).

2. Luc Couturier, Ingo Nosske, Fachao Hu, Canzhu Tan, Chang Qiao, Y. H. Jiang, Peng Chen, and Matthias Weidemüller. Laser frequency stabilization using a commercial wavelength meter. *Rev. Sci. Instrum.* 89, 043103 (2018).